

Copyright © 1999, by the author(s).
All rights reserved.

Permission to make digital or hard copies of all or part of this work for personal or classroom use is granted without fee provided that copies are not made or distributed for profit or commercial advantage and that copies bear this notice and the full citation on the first page. To copy otherwise, to republish, to post on servers or to redistribute to lists, requires prior specific permission.

**THE MECHANISM OF RADIATION
INDUCED DENSIFICATION IN FUSED SILICA**

by

Fan Piao

Memorandum No. UCB/ERL M99/71

28 December 1999

**THE MECHANISM OF RADIATION
INDUCED DENSIFICATION IN FUSED SILICA**

by

Fan Piao

Memorandum No. UCB/ERL M99/71

28 December 1999

ELECTRONICS RESEARCH LABORATORY

College of Engineering
University of California, Berkeley
94720

The Mechanism of Radiation Induced Densification
in Fused Silica

by

Fan Piao

B.S. (Nankai University, Tianjin, China) 1988
M.S. (Nankai Institute of Mathematics, Tianjin, China) 1991

A dissertation submitted in partial satisfaction of the
requirements for the degree of

Doctor of Philosophy
in

Engineering - Materials Science and Mineral Engineering

in the

GRADUATE DIVISION

of the

UNIVERSITY OF CALIFORNIA, BERKELEY

Committee in charge:

Professor William G. Oldham, Co-chair
Professor Eugene E. Haller, Co-chair
Professor Tim Sands
Professor Jeffery Bokor

Fall 1999

The dissertation of Fan Piao is approved:

W W Oldham 12/12/1999
Cochair Date

[Signature] Dec 12, 1999
Cochair Date

[Signature] 12/10/99
Date

July V. Lutz 12/14/99
Date

University of California, Berkeley

Fall 1999

**The Mechanism of Radiation Induced Densification
in Fused Silica**

Copyright © 1999

By

Fan Piao

Abstract

Radiation Induced-Densification in Fused Silica

by

Fan Piao

Doctor of Philosophy in Engineering – Materials Science and Engineering

University of California at Berkeley

Professor William G. Oldham, Cochair

Professor Eugene E. Haller, Cochair

In this thesis, deep-UV (193nm) induced densification in fused silica is reviewed and some new compaction data are presented. UV-induced compaction in fused silica obeys a universal relation where, using the total energy absorbed from two-photon absorption as the dose parameter, density changes are equal to a material dependent constant times the dose parameter to a power of about 0.66 (2/3). With the exception of the two-photon damage excitation, this behavior is consistent with the compaction studies using electron beam and gamma radiation, suggesting like densification mechanisms.

We have developed a two-phase model to describe the structure of vitreous silica. Low temperature phase *A* and high temperature phase *B* are connected by a solid state phase transition and the phase transition temperature should be higher than the glass transition temperature. This model is based on the observed volume change induced by hydrostatic pressure, fast neutron, ion, electron and photon irradiation etc. Using this structural model, we can understand the compaction-fluence behaviors for two distinct compaction phenomena; knock-on (atomic displacement) radiation-induced-compaction and ionization-induced-compaction. Generally, knock-on radiation triggers a $A \rightarrow B$

phase transition in vitreous silica. For ionization-induced compaction, we propose a simple bridging-bond relaxation mechanism to explain the observed stretched power (2/3) dependence of compaction on deposited energy for ionization induced compaction in silica.

We have used thermal annealing techniques to study the deep ultraviolet-induced compaction in fused silica, and found a strong correlation between the UV-compaction rates and thermal histories among various samples. Experimental observations agree with the predictions based on our compaction model.

We have constructed a 193nm interferometer and measured the optical-path-length difference (OPD) changes from compaction at the actinic wavelength. For the first time, we were able to directly observe the spatial variation of OPD, clearly showing the reduction in OPD outside the damaged region (because of the surface indentation) in contrast to the density-driven OPD increase inside the damaged area. The compaction-induced OPD decreased in thermal annealing and the reduction agreed with our stress-induced birefringence results.

WG Oldham 12/12/99

Prof. William G. Oldham (Committee Co-Chairman)

E. Haller, 12/12/99

Prof. Eugene E. Haller (Committee Co-Chairman)

Table of Contents

Chapter 1 Background	1
1.1 Introduction.....	1
1.2 Structure of fused silica	2
1.3 Types of fused silica	7
1.4 Interaction between radiation and fused silica.....	9
1.5 Color centers in vitreous silica: our current understanding	10
1.6 Compaction.....	13
1.7 References.....	17
 Chapter 2 Compaction Measurements Using Stress-Induced Birefringence and At-Wavelength (193nm) Interferometry	 25
2.1 Introduction.....	25
2.2 Stress-induced birefringence method.....	26
2.2.1 Experimental method	26
2.2.2 Three-region model for long cylindrical, large radius samples	30
2.2.3 Using the compaction model to analyze birefringence distributions.....	33
2.2.4 Example experimental result.....	35
2.3 Phase-shifting point diffraction interferometer at 193nm wavelength	39
2.3.1 Description.....	39
2.3.2 Direct OPD measurement of UV-damaged fused silica samples	41
2.4 Conclusions.....	47
2.5 References.....	48
 Chapter 3 Compaction Data for Various Fused Silica Samples.....	 49
3.1 Introduction.....	49
3.2 Two-photon absorption mechanism.....	49
3.3 Experimental set-up and preliminary results	52
3.4 Comparison of compaction rates	55
3.5 Comparison to older compaction studies.....	60
3.6 Conclusions.....	63
3.7 References.....	64
 Chapter 4 Temperature Effects on the UV Compaction Rate and Thermal Annealing Experiments	 66
4.1 Introduction.....	66
4.2 Ambient temperature effects on compaction rates.....	67
4.3 Isochronal annealing of compaction	71
4.4 Isothermal annealing of compaction.....	74
4.5 Compaction recovery or plastic flow	77
4.6 Pre-annealing of virgin samples.....	85
4.7 Summary.....	88
4.8 References.....	89

Chapter 5 Mechanisms in Radiation-Induced Compaction of Fused Silica.....	90
5.1 Introduction.....	90
5.2 Structural change induced by radiation and hydrostatic pressure.....	91
5.3 Two-phase model for vitreous silica.....	96
5.4 Compaction induced by knock-on radiation.....	102
5.5 Conclusions.....	103
5.6 References.....	104
 Chapter 6 Theory of Ionization-Induced Compaction in Fused Silica	 108
6.1 Introduction.....	108
6.2 Ionization-induced compaction in fused silica	108
6.3 Boltzmann distribution function of bridging bond angles	110
6.4 The relaxation of bridging bond angles	114
6.5 Compaction model for ionization radiation	116
6.6 Discussion	119
6.7 Conclusions.....	122
6.8 References.....	123
 Chapter7 Conclusions.....	 126
 Appendix.....	 129
A-I. Gamma ray induced compaction in fused silica.....	129
A-II. X-ray diffraction study of compacted fused silica	133
A-III. References.....	136

List of Figures

Chapter 1

Figure 1-1. X-ray diffraction of amorphous SiO_2	3
Figure 1-2. SiO_4 tetrahedron structure in vitreous silica.....	5
Figure 1-3. Continuous Random Network (CRN) structure of vitreous silica	7
Figure 1-4. X-ray diffraction intensity curves of neutron irradiated and unirradiated vitreous silica.....	15

Chapter 2

Figure 2-1. Schematic drawing of the geometry of damaged spot on the samples	27
Figure 2-2. Schematic drawing of the experimental setup for 193nm UV test	28
Figure 2-3. 193nm material damage testing instrumentation	29
Figure 2-4. Vector definition for birefringence analysis	33
Figure 2-5. Measured birefringence for damaged sample	36
Figure 2-6. Simulated birefringence for damaged sample.....	37
Figure 2-7. At-wavelength (193nm) PS/PDI set-up	40
Figure 2-8. Calibration interferogram obtained with no test sample installed	42
Figure 2-9. Measured wavefront from tested sample	44
Figure 2-10. Wavefront-center cross-section.....	45

Chapter 3

Figure 3-1(a). Temporal profile of the 193nm beam at 22kV, 20Hz.....	51
Figure 3-1(b). Temporal profile of the 193nm beam at 22kV, 333Hz	51
Figure 3-2. Effective pulse duration at different operating frequency.....	52
Figure 3-3. Unconstrained densification in Corning 7940.....	54
Figure 3-4. Unconstrained densification in Corning 7940 (log-log scale)	54
Figure 3-5. Unconstrained densification in Suprasil 311.....	55
Figure 3-6. Unconstrained densification in fused silica A-F	57
Figure 3-7(a). Unconstrained densification in fused silica A and B (log-log scale)..	57
Figure 3-7(b). Unconstrained densification in fused silica C and D (log-log scale)	58
Figure 3-7(c). Unconstrained densification in fused silica E and F (log-log scale)	58
Figure 3-8. Compaction data for various types of ionizing radiation	62

Chapter 4

Figure 4-1. Temperature dependence of damage rate of sample E.....	69
Figure 4-2. Temperature dependence of damage rate of sample C	69
Figure 4-3. Relative recovery vs annealing temperature for sample D and E	72
Figure 4-4. The activation energy of thermal recovery (sample D and E)	72
Figure 4-5(a). Isothermal annealing data for sample A at three temperatures.....	75
Figure 4-5(b). Isothermal annealing data for sample B at three temperatures.....	75
Figure 4-6. Isothermal annealing data for pressure compacted fused silica	76
Figure 4-7. Isothermal annealing data for sample A, B, D, and F at 500°C	76
Figure 4-8. Schematic drawing of experimental flow for verification of	

thermal recovery of UV-induced densification in fused silica	79
Figure 4-9(a). UV compaction behavior for uniformly compacted sample B	80
Figure 4-9(b). UV compaction behavior for uniformly compacted sample D	80
Figure 4-9(c). UV compaction behavior for uniformly compacted sample F	81
Figure 4-10. The measured wavefront for sample I and II (before annealing).....	83
Figure 4-11. The measured wavefront for sample I and II (after annealing).....	83
Figure 4-12. Cross sections of the wavefront, before and after thermal annealing (sample I and II)	84
Figure 4-13(a). UV compaction behavior for virgin and 950°C pre-annealed B and D....	87
Figure 4-13(b). UV compaction behavior for virgin and 950°C pre-annealed A and F	87

Chapter 5

Figure 5-1. Change in density with neutron irradiation of crystalline quartz and vitreous silica	93
Figure 5-2. The Gibbs free energy for vitreous silica.....	97
Figure 5-3. Most probable Si-O-Si angle as a function of fictive temperature.....	100

Chapter 6

Figure 6-1. Bridging bond angle distribution as a function of fictive temperature	110
Figure 6-2. Using Boltzmann distribution to fit the X-ray diffraction data for Si-O-Si bridging bond angle distribution in vitreous silica	113

Chapter 7

Appendix

Figure A-1(a). UV-induced compaction curve for sample D before and after gamma irradiation.....	131
Figure A-1(b). UV-induced compaction curve for sample E before and after gamma irradiation.....	132
Figure A-1(c). UV-induced compaction curve for sample F before and after gamma irradiation.....	132
Figure A-2. Transmission decay at 193nm after gamma radiation for 1-cm thick samples	133
Figure A-3. The geometry of the tested sample-----Suprasil 2.....	134
Figure A-4. X-ray diffraction spectra of Suprasil 2	134
Figure A-5. Spatial atomic distribution in UV damaged and undamaged Suprasil 2.....	135

List of Tables

Chapter 1

Chapter 2

Chapter 3

Table 3-1. Curve fitting parameters for fused silica A—F59

Table 3-2. Dose exponent for compaction formation from
previous compaction studies61

Chapter 4

Table 4-1. Temperature dependence of damage rate for sample A and D70

Chapter 5

Chapter 6

Chapter 7

Appendix

Table A-I. Gamma radiation-induced compaction in fused silica (Type F)130

ACKNOWLEDGEMENTS

I would like to take this opportunity to express my deepest appreciation and gratitude to my research advisors, Professor William G. Oldham and Professor Eugene E. Haller for their insightful guidance and support throughout the duration of this study. I also thank Professor Tim Sands and Professor Jeffery Bokor for serving on my dissertation committee. Finally, I am grateful to Professor Ronald Gronsky for serving on my qualifying examination committee.

The friendly research atmosphere at Berkeley has helped to promote my learning of materials science and optical lithography. I would especially like to thank Dr. Richard Schenker for his help and friendship, he patiently served as my mentor when I first joined this group and collaborated with me for two and half years. The presence of several fellow students has also been a key ingredient in my enjoyment of graduate studies at Berkeley. It is not possible to list all of their names here, but among them are Yashesh Shroff, Ebo Croffie, Mosung Chen, Haolin Zhang, Sanghun Lee, Bo Wu, Yijian Chen, Konstantinos Adam, Dr. Edita Tejnil, Pingan Huang, Dr. Weidong Yi and Ning Zhang. Xiangmin Kwauk and Dr. Kexin Jing have also been constant sources of assistance and encouragement.

Finally, I am eternally grateful to my family. Without their motivation, wisdom, sacrifice, and love, this dissertation could not have been accomplished.

This research has been jointly sponsored by the Semiconductor Research Corporation (SRC), Intel, and SEMATECH.

To my mother

Chapter 1

Background

1.1 Introduction

Lithography is recognized as the key technology pacing the evolution of microelectronics. Projection optical lithography has provided many generations of improvements in feature size, overlay accuracy, throughput, and will continue to do so for several more generations of integrated circuits. Currently, 248nm lithography (KrF excimer laser source) is being used in advanced production to manufacture device features of 0.25 μm . At the end of 1999, 193nm (ArF excimer laser source) lithography will be introduced to make device features of 0.18 μm or smaller. Lithography using deep ultraviolet (UV) wavelengths is subject to a variety of limitations. One fundamental problem is that only fused silica (SiO_2) and calcium fluoride (CaF_2) are suitable optical materials for wavelengths below 350nm. Even though CaF_2 offers excellent transparency at UV wavelengths and can be resistant to optical damage, it normally has high intrinsic birefringence and has limited availability. Fused silica, on the other hand, offers sufficient transmission in the 180-300nm wavelength range, good enough surface quality and homogeneity to be used in a diffraction-limited system. But fused silica undergoes compaction and forms color centers when exposed in UV radiation. While compaction introduces phase aberrations in imaging systems, color centers cause lens heating. Characterizing the deep ultraviolet induced damage in fused silica and understanding the damage mechanism are critical for lithographic applications. So far, very comprehensive experimental data of deep UV damage in fused silica have been gathered, but we still

know very little about the physical mechanism of radiation damage in silica. In this thesis, I will propose a physical model to explain the radiation-induced densification in fused silica.

In order to be able to describe the effects of radiation on fused silica, we have to understand the structure of fused silica. Unlike quartz, fused silica is an amorphous solid, and its structure is complex. In this chapter, I will summarize the current available structural models and characterize the basic defect centers in fused silica. This information is relevant in developing the compaction model.

1.2 Structure of fused silica

As in the structural study of crystalline solids, X-ray [1] and neutron [2] diffraction measurements serve as tools for gaining insight into the amorphous structure of fused silica. The diffraction of X-rays and neutrons gives information about the structure of rings (Fig. 1-1) [3] whose radial variation of intensity provides a 1-dimensional representation of the 3-dimensional glass structure. Clearly some information about the structure is "averaged out" in the experiment. Such measurements give much less information about the structure of fused silica, compared to that of a crystalline solid. The interpretation of the diffraction data does not provide a unique structure. In practice, one proposes a likely structure, predicts experimental results and compares these with the observations. If the comparison is poor, the specific model is rejected; however, a good comparison merely qualifies the model as an acceptable candidate, but leaves open the possibility that some other model would do as well, or even better.

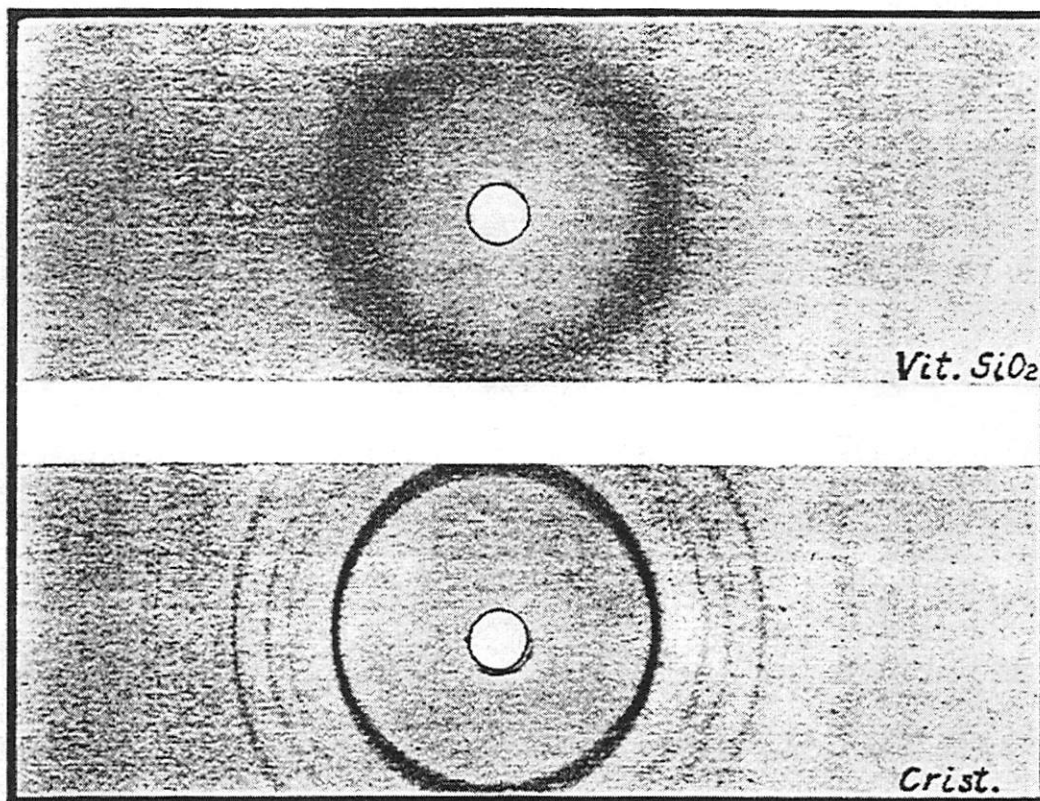


Figure 1-1. X-ray diffraction of amorphous SiO_2 (above), and cristobalite (below).
Copied from reference [3].

The uniqueness issue motivates the need for many different experimental probes of structure. Diffraction, NMR, vibrational spectroscopy and other techniques [4] emphasize different aspects of structure, such as inter-atomic distances, or angles, or local symmetry, or range of order, and the like. Each technique provides an alternative view of the structure and generally averages the structure differently, thus revealing aspects that may be de-emphasized or obscured by another technique. For example, neutrons penetrate much deeper into a material, thus neutron diffraction tends to provide more

information on bulk structure than do X-ray diffraction experiments. Raman spectroscopy generally gives information on the strength of molecular vibrational modes [5] in the material that in turn provides structural information. Although each probe gives limited information, the combined results of several different probes can dramatically reduce the number of possible models, leading us to closer to the "true" model.

Historically, there were five famous models for amorphous SiO_2 in terms of short-range order, intermediate range order, long range order [6]. These are:

- (I) the 1921 microcrystallite model of Lebedev [7];
- (II) the 1936 extension of the Lebedev model by Valenkov and Porai-Koshits [7];
- (III) the 1932 continuous random network model (CRN) of Zachariasen [8];
- (IV) the 1936 extension of this by Warren *et al.* [9];
- (V) the 1982 "paracrystallite" model of J.C. Phillips [10];

Strong arguments against all but the Zachariasen (III) and Warren (IV) models were presented in reference [6], many of these arguments have previously been given by others. The Zachariasen-Warren (ZW) model for the structure of vitreous silica is accepted broadly, and it is the model I will use to discuss the mechanism of radiation-induced compaction in fused silica.

It is clear that glasses contain sufficient disorder such that their structure must ultimately be defined statistically. In vitreous silica, the short range order is commonly specified by stating that each Si atom is surrounded almost tetrahedrally by four oxygen atoms at a bonding distance r of 1.61 \AA , while each O atom bridges between two Si atoms at the same distance. There is a small spread in the bond distance r , a small spread in the O-Si-O angles ϕ , and a much larger spread in the Si-O-Si angle β . (See Fig. 1-2)

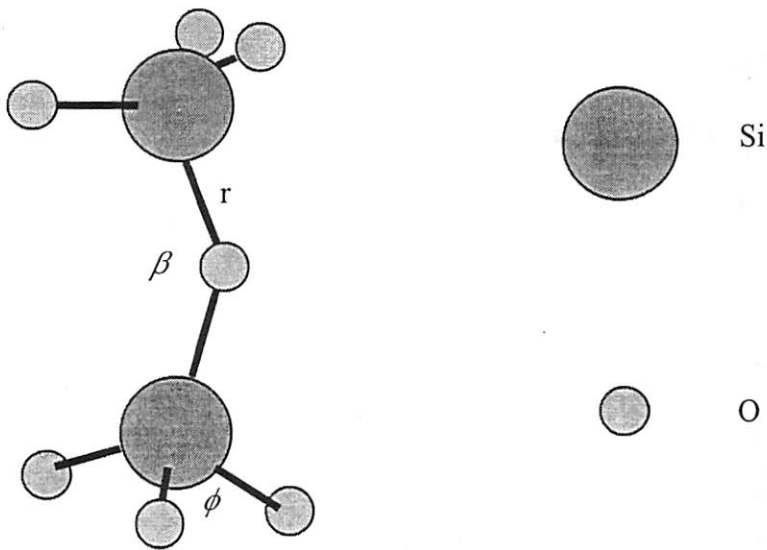


Figure 1-2. SiO_4 tetrahedron structure in vitreous silica.

The ZW model is properly defined in the papers of Zachariasen [8], Warren, Krutter and Mornigstar [9], Warren [11] and Mozzi and Warren [12]. Although its overall features have been described in numerous textbooks [13-16], we list here some of the characteristics of the ZW model of glass.

The short range order of the ZW model.

- * only Si and O atoms (no impurities).
- * only Si-O bonds (chemically ordered).
- * a narrow unimodal distribution of bond lengths r , peaked at 1.61\AA .
- * each Si bonded almost tetrahedrally to four O atoms (4-coordinated Si).
- * a narrow unimodal distribution of O-Si-O angle ϕ , peaked at 109.5° .
- * each O bridges between two Si atoms (2-coordinated O).
- * a broad unimodal distribution of Si-O-Si angles θ , peaked at 145° .
- * the r , θ , ϕ are uncorrelated, amongst themselves and with each other.

The intermediate range order of the ZW model.

- * the tetrahedrons share corners only (no 2-rings).

The long range order (LRO) of the ZW model.

- * there is no morphological LRO.
- * there is no crystalline LRO (not microcrystalline).

The global range order of the ZW model.

- * the material is chemically ordered everywhere.
- * the network is “continuous”, in that there are no broken bonds.
- * the network is topologically 4-connected everywhere.
- * the structural parameters are homogeneous statistically (all rings).
- * the network is microscopically isotropic.
- * the macroscopic density of the model is that of a real glass sample.

The ZW model is a specific model based upon the Continuous Random Network (CRN) (Fig. 1-3) as its conceptual parent. Numerous specific models have been developed that can be considered as approximations of the ZW model. They involve simplifications designed to facilitate construction or calculations of properties of the ZW model of a glass. Here we listed six examples.

The isolated molecule model [17].

The Bell and Dean large cluster models [18].

The large amorphous unit cell models [19,20].

The Sen and Thorpe model [21].

The Bethe lattice model [22].

The Oxygen steric hindrance model [23,24].

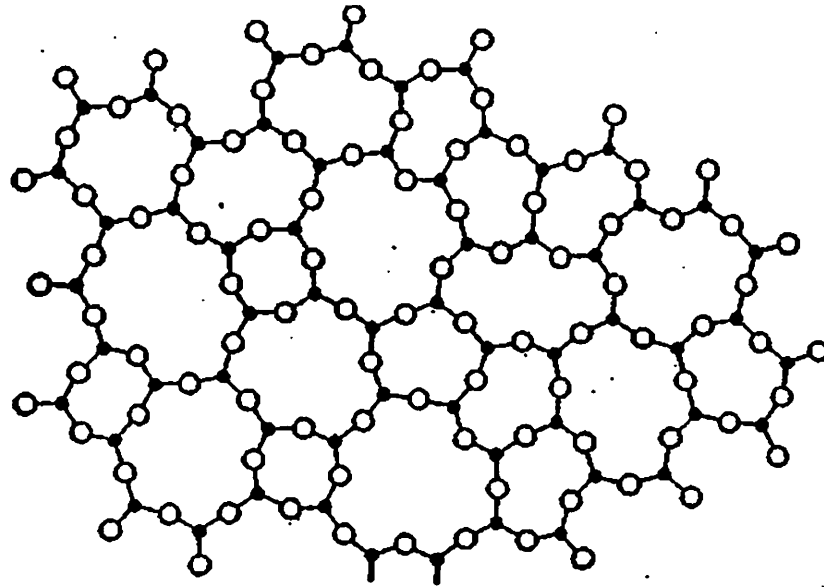


Figure 1-3. Continuous Random Network (CRN) structure of vitreous silica. Copied from reference [3].

1.3 Types of fused silica

The properties of silica, and in particular its response to radiation, are determined to a large extent by the type and concentration of impurities such as alkali atoms, aluminum, chlorine, and hydroxyl; in turn these are influenced by the technique used to fabricate the glass. Bruckner [25] classified silica into five types according to fabrication process:

Type I. Type-I silica glasses are produced from natural quartz by electrical fusion under vacuum or under an inert gas atmosphere. They contain nearly no OH-groups (about

5ppm or less) but relatively high metallic impurity concentrations of the order of 30-100ppm Al and 1-4ppm Na (all in weight fractions). This category includes Infrasil [26], IR-Vitreosil [27], and G. E. 105, 201, 204 [28].

Type-II. Type II-silica glasses are produced from quartz crystal powder by flame fusion (Verneuille-process). Because of the partial volatilization and the absence of any crucible material the metallic impurities are less than in type I silica glasses, but the atmosphere of the hydrogen-oxygen flame causes an OH-content of about 150-400ppm. Trade names are Herasil, Homosil [26], Optosil [26], O.G. Vitreosil [27], G.E. 104 [28]. A special thermal treatment in an oxygen atmosphere, resulting in a good optical transparency in the ultraviolet range, leads to Ultrasil [26] silica glass.

Type-III. Type III-silica glasses are synthetic vitreous silica prepared by hydrolysis of SiCl_4 in an oxygen-hydrogen (or oxygen-hydrocarbon) flame. This material is practically free from metallic impurities, but contains a high amount of OH, on the order of 1000ppm, and because of the starting material Cl in quantities of the order of 100ppm. Trade names: Suprasil [26], Spectrosil [27], and Corning 7940 [29]. Basically, all ultraviolet (UV)-grade fused silica are type III silica.

Type-IV. Type IV-silica glasses are also synthetic vitreous silica produced from SiCl_4 in a water vapor-free plasma flame. These silica are similar to type III but contain only about 0.4ppm OH and about 200ppm Cl. Trade names: Suprasil W [26], Spectrosil WF [27], and Corning 7943 [29]. Another type was produced but only in a single case and on

a laboratory scale. The starting material was silicon of semiconductor-quality that was oxidized in pure oxygen high-frequency plasma flame. The impurity content, especially the OH-content, was extremely low.

Type V. Type V-silica glasses are manufactured using new synthetic processes, such as sol-gel fabrication [30], modified chemical vapor deposition process [31] etc. Examples include Suprasil 200, 300, 311 and 312; Corning 7957 and 7980 [29].

1.4 Interaction between radiation and fused silica

There are two principal interactions of the radiation with fused silica---ionization of electrons and direct displacement of atoms via a collision (knock-on). When silica is subjected to ionizing radiation (X-rays, gamma rays, electrons, etc.), ionizing radiation initially excites electron-hole pairs via the Compton effect [32-35]. Electrons are ionized from the valence band if the energy of the radiation is greater than the band gap. The excess energy is converted to kinetic energy. As these energetic “hot” electrons travel through the material they ionize other electrons, losing the energy of ionization while forming a secondary electron-hole cascade. When the electrons no longer have sufficient energy to ionize additional electrons, they can be trapped at the sites of defects (such as non-bridging oxygens, oxygen vacancies, etc.) which are either pre-existing in the glass or created by the high-energy electrons themselves. Another effect of ionizing radiation is the creation of bound electron-hole pairs (excitons), whose non-radiative deexcitation can result in the displacement of atoms by the radiolytic process [34].

High-energy particle radiation (neutrons, protons, ions, etc.) manifests itself in knock-on displacements of atoms [33,34,36]. In the knock-on process, a fraction of the momentum and of the energy of the incident particle are directly transferred to an atom in the crystal lattice or glass network. If the transferred energy is sufficient to break the bond, the struck atom is displaced into an interstitial position. The minimum transferred energy required to accomplish such a knock-on event is of the order of the strength of the bond which must be broken, usually about 4-25 eV. This threshold for atomic displacement is perhaps considerably decreased by trapping of carriers injected by ionization at defect centers [37]. The structural changes induced by particle radiation are invariably accompanied by ionization effects.

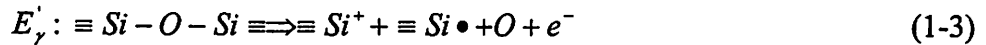
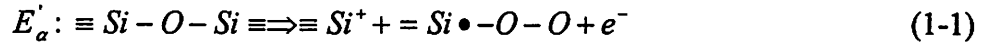
Ionizing radiation can also cause displacements. If an incident electron or the Compton electron excited by an X-ray or gamma photon has sufficient energy, it can then transfer the 4-25 eV required to displace an atom from its position in the network. The minimum energy required for the electron to remove a Si atom from its position in the glass matrix is 0.26 MeV, while that for an O atom is 0.16 MeV [33].

1.5 Color centers in vitreous silica: our current understanding

Radiation induces color centers in vitreous silica [38-68]. Color centers are structural defects that correspond to induced absorption bands in the optical spectrum of a material. In deep UV lithographic applications, the formation of color centers can reduce transmission through a lithographic system. Absorption induces temperature changes, leading to refractive index changes that can induce imaging aberrations in lithographic systems.

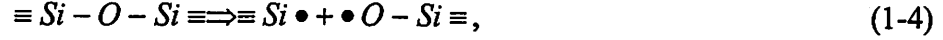
Most of the information we have about defect structures in silica comes from electron spin resonance (ESR) [69-72]. The most important paramagnetic centers in a-SiO₂ are the E' center, the non-bridging oxygen hole center (NBOHC) and the peroxy radical.

From studies of the hyperfine structure in the ESR spectrum arising from the ²⁹Si and ¹⁷O isotopes, we know the E' center contains an unpaired electron in a dangling, tetrahedral (sp^3) orbital of a single silicon atom which is bonded to just three oxygen atoms in the glass network [73,74]. However, in practice, one observes a diversity of defect production and annealing kinetics depending on both the character of the radiation and the water content and/or thermal histories of the vitreous silica samples [75-77]. These results suggest the possible existence of several E' center variants. So far, at least three different kinds of E' center [34] have been found and proved to be distinguishable on the basis of subtle difference in their ESR spectroscopic signatures [76]. The reactions producing these E' centers are as follows:



where the symbol (\equiv) represents bonding to three oxygen atoms, ($=$) represents bonding to two oxygen atoms, (\bullet) represents an unpaired electron, and ($\equiv Si \bullet$) represents the E' center. E' centers have a characteristic absorption band centered on 210 to 215nm with a full width at half maximum (FWHM) of about 50nm.

The non-bridging oxygen hole center (NBOHC) represented by ($\bullet O - Si \equiv$) is another important defect formed in irradiated silica. It can be produced in silica according to:

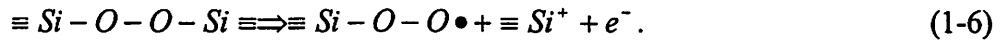


or in high-OH silica according to:



An absorption band centered on 260nm with a FWHM of about 40nm is often attributed to the NBOHC.

A second oxygen-associated hole center in a-SiO₂ is the peroxy radical [78,79]. Studies [79,80] have shown that this defect consists of a radical ion bonded to single silicon atom in the glass network ($\equiv Si - O - O \bullet$). The precursor structure in the glass network is the peroxy linkage ($\equiv Si - O - O - Si \equiv$). Radiation produces the peroxy radical defect according to:



The peroxy radical is generally associated with the absorption band around 163 -167nm.

In addition to the above discussed point defects, a-SiO₂ contains localized, defined structures which can be treated as structural defects in a continuous random network (CRN) model of the glass. The most prominent are the D1 and D2 'defects' associated with the Raman bands at 490 and 604 cm⁻¹, respectively [4]. They are relatively sharp features compared with the dominating broad bands in the spectrum at 430, 800 and 1060 cm⁻¹ and have not been explained by CRN models [21]. Both 'defects' bands have been interpreted as symmetric stretching modes of regular fourfold (D1) and planar threefold (D2) rings embedded in the irregular glass network. This interpretation is

based on (i) the nearly exact agreement with the dominant Raman frequencies of isolated cyclosiloxane ring molecules [81], (ii) on nearest-neighbor, central and non-central for calculations of the vibrational modes in α -SiO₂, (iii) on fundamental considerations of the decoupling of localized vibrations from the surrounding glass network [82], (iv) on isotope-enrichment experiments [83,84] and (v) recently on investigations using nuclear magnetic resonance (NMR) techniques [85,86].

1.6 Compaction

Fused silica (density 2.2g/cm³) compacts when exposed to X-rays [87,88], gamma rays [87-92], electron-beams [37,87,88, 93-96], neutrons [87,88, 97-102], ions [87,88], and UV-radiation [38, 40,42,103-106]. Compaction in fused silica has been the subject of considerable interest owing to the use of silica and silica-based ceramics in nuclear and fusion reactors and the concern for dimensionally stable optics for space application. Recently, compaction in fused silica has become a very important issue in micro-electronic applications, because compaction leads directly to refractive index changes in fused silica that produce imaging aberrations in a deep UV lithographic optics.

In general, the radiation dose dependence of compaction in fused silica obeys the so-called "stretched power dependence":

$$\frac{\Delta\rho}{\rho} = A' D_a^c \quad (1-7)$$

where ρ is the density of fused silica, D_a is the absorbed dose, and A' and c are constants. The dose exponent c seems to be dependent on the type of silica and the nature of the radiation source. Primak and Kampwirth [87] observed linear compaction ($c=1$) in silica irradiated with neutrons, He⁺, or D⁺, while values of $c=0.5$ to 0.7 were

measured for H⁺, electrons, or gamma rays. Our data (Chapter 3) show c to be in the vicinity of 0.66 (2/3) for 193nm UV radiation. Other workers found c to be in the range from 0.55 to 0.7 for UV radiation. [103-105]

The compaction kinetics appears to differ for the two distinct processes, one associated with atomic displacements and one associated with ionization.

The macroscopic effects of atomic displacement radiation in fused silica are now well established. [107-109] At doses in excess of $\sim 2 \times 10^{20}$ fast neutrons cm⁻², fused silica approaches a final amorphous state which has a density between 2 and 3% higher than that of normal vitreous silica. X-ray diffraction patterns before and after radiation give insight into the structural rearrangements coinciding with compaction. Fig. 1-4 shows typical results for a neutron irradiation experiment. Transforming the spectra in Fig. 1-4 yields electron distribution densities that suggest a reduction in average Si-Si spacing.

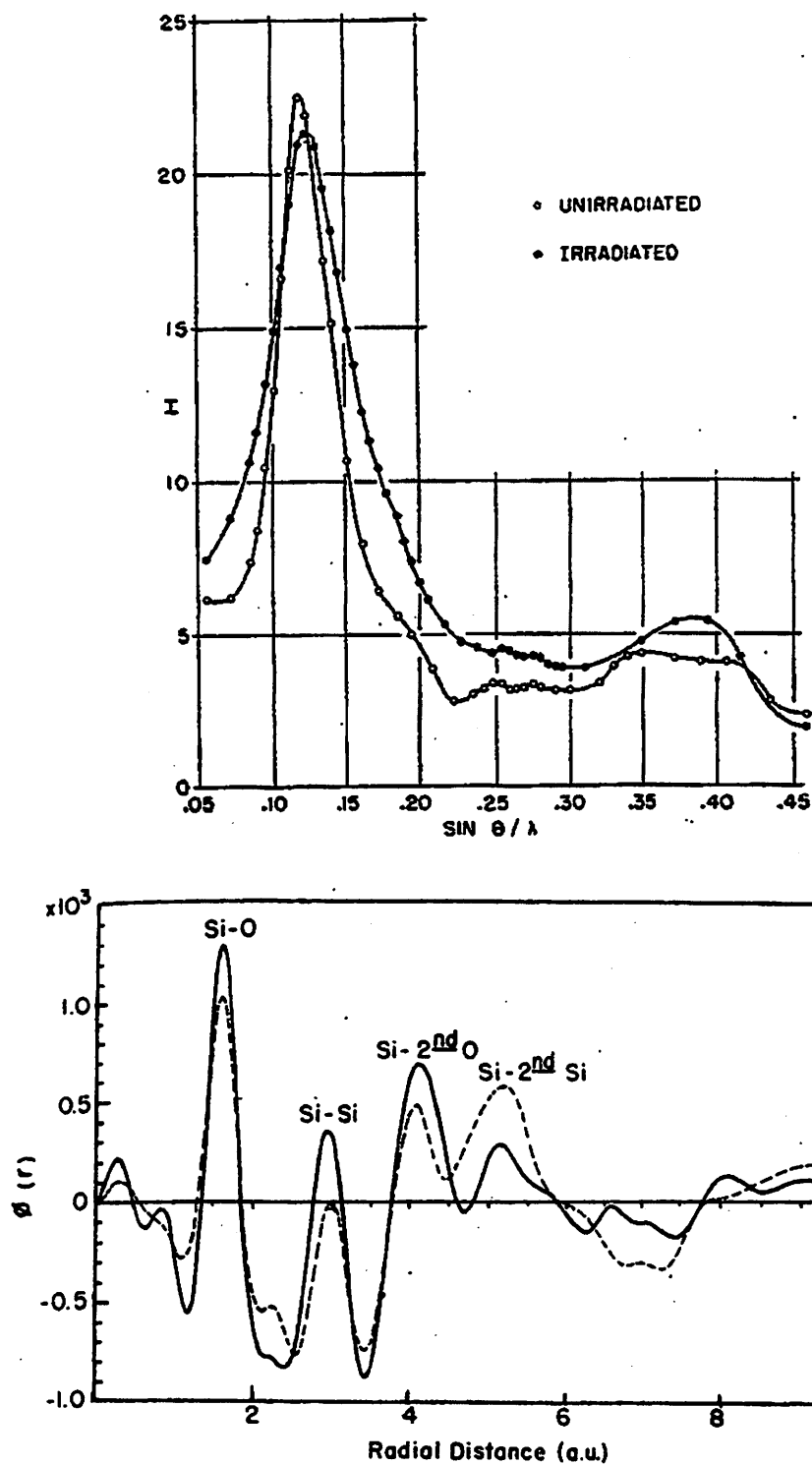


Figure 1-4. X-ray diffraction intensity curves of neutron irradiated and unirradiated vitreous silica (above) and their Fourier transformation (below), solid curve, irradiated silica; dashed curve, vitreous silica. Vertical scale is arbitrary. Copied from reference [110].

For ionizing radiation, because the compaction level is generally very small compared with that induced in atomic displacement radiation, we still lack information regarding the structural change inside the glass network. We attempted an X-ray diffraction measurement on a heavily UV-damaged fused silica sample (see Appendix), and found no obvious difference in the diffraction patterns from that of virgin samples. This result is not unexpected considering the relatively small compaction we could achieve in reasonable radiation time ($\sim 10\text{ppm}$).

In this thesis, I will first review the compaction measurement methods in Chapter 2 and then present the characterization of the UV-induced compaction among a variety of fused silica samples in Chapter 3. Studies of the effect of temperature on UV-induced compaction (at 193nm wavelength) in fused silica are given in Chapter 4. I then propose a theory for the radiation-induced compaction in fused silica, for both knock-on radiation (Chapter 5) and ionizing radiation (Chapter 6). In this theory, the direct atomic displacement damage and ionizing damage are treated as two distinct damage mechanisms. The theory addresses the different values of c in Eq. (1-7) for the two mechanisms. It is also found to be consistent with the observations of the thermal annealing experiments presented in Chapter 4.

1.7 References:

- [1] Kittel, "Introduction to Solid State Physics", 7th Edition, John Wiley & Sons, Inc. (1996)
- [2] A.C.Wright, B.Bachra, T.M.Brunier, R.N.Sinclair, L.F.Gladden, R.L.Portsmouth, "A neutron diffraction and MAS-NMR study of the structure of fast neutron irradiated vitreous silica". *Journal of Non-Crystalline Solids*, 69, 150 (1992)
- [3] B.E.Warren, "X-ray Diffraction" Addison-Wesley, Reading, (1969)
- [4] F.L.Galeener, "Planar rings in glasses". *Solid State Communications*, vol.44, 1037 (1982)
- [5] A. Yariv, "Quantum Electronics", third edition, John Wiley & Sons, Inc. 1989
- [6] F.L.Galeener, in "Proceedings of the Second International Conference on the Effects of Modes of Formation on the Structure of Glasses", edited by R.A.Weeks and D.L.Kinser *Trans. Techn. Publications, Aedermansdorf*, (1988)
- [7] E.A.Porai-Koshits, "Structure of glass: the struggle of ideas and prospects". *Journal of Non-Crystalline Solids*, vol.73 79 (1985)
- [8] W.H.Zacharisen, *J. Am. Chem. Soc.* 54:3841 (1932)
- [9] B.E.Warren, H.Krutter, O.Morningstar, *J. Am. Ceram. Soc.* 19:202 (1936)
- [10] J.C.Phillips, *Solid State Phys.* 37:93 (1982)
- [11] B.E.Warren, *J. Appl. Phys.* 8: 645 (1937)
- [12] R.L.Mozzi, B.E.Warren, "The structure of vitreous silica". *Journal of Applied Crystallography*, vol.2, 164 (1969)
- [13] R.H.Doremus, *Glass Science*, Wiley, New York (1973)
- [14] W.D.Kingery, H.K.Bowen, D.R.Uhlman, "Introduction to Ceramics, 2nd edition" Wiley, New York (1976)
- [15] R. Zallen, "The Physics of Amorphous Solids", Wiley, New York (1983)
- [16] S.R.Elliott, "Physics of Amorphous Materials", Longman, London (1984)
- [17] G.Lucovsky, R.M.Martin, "A molecular model for the vibrational modes in chalcogenide glasses". *Journal of Non-Crystalline Solids*, vol.8-10, 185 (1972)
- [18] R.J.Bell, P.Dean, "The structure of vitreous silica: validity of the random network theory". *Philosophical Magazine*, vol.25, (no.6), 1381 (1972)

- [19] F.Wooten, K.Winer, D.Weaire, "Computer generation of structural models of amorphous Si and Ge". Physical Review Letters, vol.54, 1392 (1985)
- [20] M.F.Thorpe, S.W. de Leeuw, "Coulomb effects in disordered solids". Physical Review B (Condensed Matter), vol.33, 8490 (1986)
- [21] P.N.Sen, M.F.Thorpe, "Phonons in $AX_{2/}$ glasses: from molecular to band-like modes". Physical Review B (Solid State), vol.15, 4030 (1977)
- [22] M.F.Thorpe, in "Excitations in Disordered Systems" ed. M.F.Thorpe, Plenum, New York (1981) P. 85
- [23] F.L.Galeener, "A model for the distribution of bond angles in vitreous SiO_2 ". Philosophical Magazine B (Physics of Condensed Matter, Electronic, Optical and Magnetic Properties), vol.51, L1 (1985)
- [24] Y.T.Thathachari, W.A.Tiller, "Steric origin of the silicon-oxygen-silicon angle distribution in silica". Journal of Applied Physics, vol.53, 8615 (1982)
- [25] R.Bruckner, "Properties and structure of vitreous silica. I". Journal of Non-Crystalline Solids, vol.5, 123 (1970)
- [26] Trademark of W.C.Heraeus-Schott Comp. Germany, and Amersil Quartz Division, Engelhard Industries, Inc.
- [27] Trademark of Thermal Syndicate Ltd., England
- [28] Trademark of General Electric Comp., U.S.A.
- [29] Trademark of Corning Comp, U.S.A.
- [30] S.P.Mukherjee, "Sol-gel processes in glass science and technology". Journal of Non-Crystalline Solids, vol.42, 477 (1980)
- [31] W.G.French, R.E.Jaeger, J.B.MacChesney, S.R.Nagel, K.Nassau, A.D.Pearson, Optical Fiber Telecommunication, eds. S.E.Miller, A.G.Chynoweth, (Academic Press, New York, 1975)
- [32] E. Lell, N.J.Kreidl, J.R.Hensler, Prog. Ceram. Sci., Vol. 4, ed. J.E.Burke (Pergamon Press, Oxford. New York, 1966) p. 1
- [33] E.J.Friebele, D.L.Griscom, Treatise Mater. Sci. Techn., Vol. 17, Glass II, eds. M.Tomozawa, R.H.Doremus, (Academic Press, New York, 1979) p. 257
- [34] D.L.Griscom, "Nature of defects and defect generation in optical glasses". Proceedings of the SPIE - The International Society for Optical Engineering, vol.541, 38(1985)

- [35] W.Primak, E.Edwards, D.Keiffer, H.Szymanski, Phys. Rev. 133 (1964)A 531
- [36] P.W.Levy, J. Am. Ceram. Soc. 43 (1960) 389
- [37] C.B.Norris, E.R.EerNisse, "Ionization dilation effects in fused silica from 2 to 18-keV electron irradiation". Journal of Applied Physics, vol.45, 3876(1974)
- [38] P. Schermerhorn, "Excimer laser damage testing of optical materials". Proceedings of the SPIE – The International Society for Optical Engineering, vol.1835, 70 (1993)
- [39] D.J.Krajnovich, I.K.Pour, A.C.Tam, W.P.Leung, M.V.Kulkarni, "248 nm lens materials: performance and durability issues in an industrial environment" Proc. SPIE 1848, 544-560 (1993)
- [40] D.J.Krajnovich, I.K.Pour, A.C.Tam, W.P.Leung, M.V.Kulkarni, "Sudden onset of strong absorption followed by forced recovery in KrF laser-irradiated fused silica", Optics Letters, 15 Vol. 18 453-455 (1993)
- [41] D.J.Krajnovich, I.K.Pour, "Long-term effects of pulses KrF laser radiation on crystalline and amorphous SiO₂", SPIE Vol. 2114 (1994)
- [42] R. Schenker, P. Schermerhorn, W. G. Oldham, "Deep-ultraviolet damage to fused silica". Journal of Vacuum Science & Technology B (Microelectronics and Nanometer Structures), vol.12, 3275 (1994)
- [43] R.Schenker, L.Eichner, H.Vaidya, S.Vaidya, P.Schermerhorn, D.Fladd, W.G.Oldham, "Ultraviolet damage properties of various fused silica materials", Laser-Induced Damage in Optical Material: 1994, 26th Annual Boulder Damage Symposium Proceedings, 458-468, SPIE proceedings 2428.
- [44] R.Schenker, L.Eichner, H.Vaidya, S.Vaidya, W.G.Oldham, "Degradation of fused silica at 193 nm and 213 nm", SPIE Vol. 2440 (1995)
- [45] M.Rothschild, D.J.Ehrlich, D.C.Shaver, "Effects of excimer laser irradiation on the transmission, index of refraction, and density of ultraviolet grade fused silica", Appl. Phys. Lett. 55 (13), 1276 (1989)
- [46] J.H.C.Sedlacek, M.Rothschild, "Optical materials for use with excimer lasers", SPIE Vol. 1835 (1992)
- [47] D.L.Griscom, "Growth and Decay Kinetics of Defect Centers in High-Purity Fused Silicas Irradiated at 77K with X-Rays or 6.4-eV Laser Light", Nucl. Inst. And Method. In Phys. Res. B46, 12-17 (1990)
- [48] T.E.Tsai, D.L.Griscom, E.J.Friebele, "Si E' Centers and UV-Induced Compaction in High Purity Silica" Nucl. Inst. And Method. In Phys. Res. B46, 265-268 (1990)
- [49] G.C.Escher, "KrF Laser Induced Color Centers in Commercial Fused Silica", SPIE Vol. 998 (1988)

- [50] R.A.Weeks, R.H.Magruder, III, P.Wang, "Some effects of 5 eV photons on defects in SiO₂", J. Non-Cryst. Solids, 149, 122-136 (1992)
- [51] R.H.Magruder, III, P.Wang, R.A. Weeks, D.L.Kinser, "KrF laser light interaction with intrinsic defects in silica", SPIE Vol. 1327, 50-59 (1990)
- [52] E.A.Nevis, "Alteration of the transmission characteristics of fused silica optical fibers by pulsed ultraviolet radiation", SPIE Vol. 540, 421-424 (1985)
- [53] H.Hitzler, Ch. Pfeleiderer, N.Leclerc, J.Wolfrum, K.O.Greulich, H.Fabian, "KrF laser irradiation induced defects in all silica optical fibers", J. Non-Cryst. Solids, 149, 107 (1992)
- [54] N.Leclerc, Ch.Pfeleiderer, H.Hitzler, J.Wolfrum, K.O.Greulich, S.Thomas, W.Englisch, "Luminescence and transient absorption bands in fused SiO₂ induced by KrF laser radiation at various temperatures", J. Non-Cryst. Solids, 149, 115 (1992)
- [55] N.Leclerc, Ch.Pfeleiderer, H.Hitzler, J.Wolfrum, K.O.Greulich, S.Thomas, W.Englisch, "Transit 210-nm absorption in fused silica induced by high-power UV laser irradiation", Optical Letters, Vol. 16, 940 (1991)
- [56] Ch.Pfeleiderer, N.Leclerc, K.O.Greulich, "The UV-induced 210-nm absorption band in fused silica with different thermal history and stoichiometry", J. Non-Cryst. Solids, 159, 145 (1993)
- [57] N.Leclerc, Ch.Pfeleiderer, H.Hitzler, J.Wolfrum, K.O.Greulich, S.Thomas, W.Englisch, "KrF excimer laser induced absorption and fluorescence bands in fused silica related to the manufacturing process", SPIE. Vol. 1327, 60 (1990)
- [58] K.Mann, H.Gerhardt, "Damage testing of optical components for high power excimer lasers", SPIE, Vol. 1503, 176 (1991)
- [59] E.Eva, K.Mann, "Calorimetric measurement of two-photon absorption and color-center formation in ultraviolet window materials", Appl. Phys. A 62, 143 (1996)
- [60] E.Eva, K.Mann, "Nonlinear absorption phenomena in optical materials for the UV-spectral range", Proceeding of Boulder Damage Symposium (1996)
- [61] A.Fujinoki, "Silica with High Resistance to Excimer Laser", SPIE, Vol. 2428, 170 (1996)
- [62] H.Nishikawa, R.Nakamura, R.Tohmon, Y.Ohki, Y.Hama, Y.Sakurai, K.Nagasawa, "Paramagnetic centers induced by ArF excimer laser irradiation in high-purity silica glasses", SPIE, Vol. 1327, 69 (1990)

- [63] K.Arai, H.Imai, H.Hosono, Y.Abe, H.Imagawa, "Two-photon processes in defect formation by excimer lasers in synthetic silica glass", Appl. Phys. Lett. 53, 1891 (1988)
- [64] N.Kuzuu, Y.Komatsu, M.Murahara, "ArF excimer laser induced emission and absorption bands in fused silica synthesized under oxidizing conditions", Phys. Rev. B Vol. 45, 2050 (1992)
- [65] N.Kuzuu, Y.Komatsu, M.Murahara, "ArF excimer laser induced emission and absorption bands in fused silica synthesized in reducing conditions", Phys. Rev. B Vol. 44, 9265 (1991)
- [66] V.P.Pashinin, N.Yu, Konstantinov, V.G.Artjushenko, V.I.Konov, A.S.Silenok, G.Muller, B.Schaldach, R.Ulrich, "Mechanism of UV laser-induced absorption in fused silica fibers", Fiber and Integrated Optics, Vol. 10, 365 (1991)
- [67] N.V.Morozov, "Laser induced damage in optical materials under UV excimer laser radiation", SPIE Vol. 2428, 153 (1996)
- [68] M.Rothschild, D.J.Ehrlich, D.C.Shaver, "Excimer Laser Induced Damage in Fused Silica", Microelectronic Engineering 11, 167 (1990)
- [69] D.L.Griscom, J. Non-Cryst. Solids, 13, 251 (1973)
- [70] D.L.Griscom, in : Defects and Their Structure in Non-metallic Solids, eds., B.Henderson, A.E.Hughes (Plenum, New York, 1976) p. 323
- [71] D.L.Griscom, "Defects in amorphous insulators". Journal of Non-Crystalline Solids, vol.31, 241 (1978)
- [72] D.L.Griscom, "Electron spin resonance in glasses". Journal of Non-Crystalline Solids, vol.40, 211 (1980)
- [73] D.L.Griscom, E.J.Friebele, G.H.Sigel Jr, Sol. St. Commun. 15, 479 (1974)
- [74] D.L.Griscom, "E' center in glassy SiO_2 : ^{17}O , ^1H , and 'very weak' ^{29}Si superhyperfine structure". Physical Review B (Condensed Matter), vol.22, 1823 (1980)
- [75] D.L.Griscom, M.Stapelbroek, E.J.Friebele, "ESR studies of damage processes in X-irradiated high purity $\alpha\text{-SiO}_2$:OH and characterization of the formyl radical defect". Journal of Chemical Physics, vol.78, 1638 (1983)

- [76] D.L.Griscom, "Characterization of three E'-center variants in X- and gamma -irradiated high purity a-SiO₂". Nuclear Instruments & Methods in Physics Research, Section B (Beam Interactions with Materials and Atoms), vol.229, 481 (1984)
- [77] D.L.Griscom, Thermal bleaching of X-ray-induced defect centers in high purity fused silica by diffusion of radiolytic molecular hydrogen. Journal of Non-Crystalline Solids, vol.68, 301 (1984)
- [78] M.Stapelbroek, D.L.Griscom, E.J.Friebele, G.H.Sigel Jr, "Oxygen-associated trapped-hole centers in high-purity fused silicas". Journal of Non-Crystalline Solids, vol.32, 313 (1979)
- [79] E.J.Friebele, D.L.Griscom, M.Stapelbroek, R.A.Weeks, "Fundamental defect centers in glass: the peroxy radical in irradiated, high-purity, fused silica". Physical Review Letters, vol.42, 1346 (1979)
- [80] D.L.Griscom, E.J.Friebele, "Fundamental defect centers in glass: ²⁹Si hyperfine structure of the nonbridging oxygen hole center and peroxy radical in a-SiO₂". Physical Review B (Condensed Matter), vol.24, 4896 (1981)
- [81] F.L.Galeener, in: The Structure of Non-Crystalline Materials, ed. P.H.Gaskell, J.M.Parker and E.A.Davis (Taylor and Francis, London, 1982) p. 337
- [82] F.L.Galeener, R.A.Barrio, E.Martinez, R.J.Elliott, Phys. Rev. Lett. 53, 2429 (1984)
- [83] F.L.Galeener, A.E.Geissberger, Phys. Rev. B27, 6199 (1983)
- [84] C.J.Brinker, D.R.Tallant, E.P.Roth, C.S.Ashley, J. Non-Cryst. Solids 82, 117 (1986)
- [85] C.J.Brinker, R.J.Kirkpatrick, D.R.Tallant, B.C.Bunker, B.Montez, "NMR confirmation of strained 'defects' in amorphous silica". Journal of Non-Crystalline Solids, vol.99, 418 (1988)
- [86] C.J.Brinker, R.K.Brow, D.R.Tallant, R.J.Kirkpatrick, "Surface structure and chemistry of high surface area silica gels". Journal of Non-Crystalline Solids, vol.120, 26 (1990)
- [87] W.Primak, R.Kampwirth, "Radiation Compaction of Vitreous Silica", J. Appl. Phys. 39, 5651 (1968)
- [88] W.Primak, R.Kampwirth, "Impurity Effect in the Ionization Dilation of Vitreous Silica", J. Appl. Phys., 39, 6010 (1968)
- [89] F. L. Galeener, "Nonlinear gamma -ray activation of defect spins in vitreous silica". Journal of Non-Crystalline Solids, vol.149, 27 (1992)
- [90] J. A. Ruller, E. J. Friebele, "The effect of gamma-irradiation on the density of various types of silica". Journal of Non-Crystalline Solids, vol.136, 163 (1991)

- [91] J. E. Shelby, "Effect of radiation on the physical properties of borosilicate glasses". *Journal of Applied Physics*, vol.51, 2561 (1980)
- [92] J. E. Shelby, "Effect of morphology on the properties of alkaline earth silicate glasses". *Journal of Applied Physics*, vol.50, 3702 (1979)
- [93] P. L. Higby, E. J. Friebele, C. M. Shaw, M. Rajaram, E. K. Graham, D. L. Kinser, E. G. Wolff, "Radiation effects on the physical properties of low-expansion-coefficient glasses and ceramics". *Journal of the American Ceramic Society*, vol.71, 796 (1988)
- [94] E. J. Friebele, P. L. Higby, in *Laser Induced Damage in Optical Materials*, 1987 NIST Spec. Pub. 756, edited by H. H. Bennett, A. H. Guenther, D. Milam, B. E. Newnam, M. J. Soileau (NIST, Boulder, CO. 1988), p. 89
- [95] M. Rajaram, T. Tsai, E. J. Friebele, "Radiation-induced surface deformation in low-thermal-expansion glasses and glass-ceramics". *Advanced Ceramic Materials*, vol.3, 598 (1988)
- [96] C. I. Merzbacher, E. J. Friebele, J. A. Ruller, P. Matic, "Long-wavelength infrared transmitting glasses: new ternary sulfide compositions". *Proceedings of the SPIE - The International Society for Optical Engineering*, vol.2018, 222 (1991)
- [97] J.B.Bates, R.W.Hendricks, L.B.Shaffer, "Neutron irradiation effects and structure of noncrystalline SiO₂", *J. Chem Phys.* 61, 4163 (1974)
- [98] W.Primak, R.Kampwirth, "ionization Expansion of Pile-Exposed Vitreous Silica", *J. Appl. Phys.* 40, 2565 (1969)
- [99] W.Primak, "Fast-Neutron-Induced Changes in Quartz and Vitreous Silica", *Phys. Rev.*, 110, 1240(1958)
- [100] W.Primak, "Radiation Behavior of Vitreous Silica", *Nucl. Sci. Eng.* 65, 141 (1978)
- [101] J.S.Lukesh, "Neutron Damage to the Structure of Vitreous Silica", *Phys. Rev.* 97, 345 (1955)
- [102] A.Hiramatsu, M.Arai, H.Shibazaki, M.Tsunekawa, T.Otomo, A.C.Hannon, S.M.Benington, N.Kitamura, A. Onodera, "Investigation on permanently densified vitreous silica by means of neutron scattering", *Physica, B*,219, 287(1966)

- [103] M. Rothschild, D. J. Ehrlich, D. C. Shaver, "Effects of excimer laser irradiation on the transmission, index of refraction, and density of ultraviolet grade fused silica". *Applied Physics Letters*, vol.55, 1278 (1989)
- [104] C. Smith, N. F. Borrelli, D. C. Allan, "Compaction of fused silica under low fluence/long term 193 nm irradiation". *Proceedings of the SPIE - The International Society for Optical Engineering*, vol.3051, 116 (1997)
- [105] D. C. Allan, C. Smith, N. F. Borrelli, T. P. Seward III, "193-nm excimer-laser-induced densification of fused silica". *Optics Letters*, vol.21, 1960 (1996)
- [106] R. E. Schenker, F. Piao, W. G. Oldham, "Material limitations to 193-nm lithographic system lifetimes". *Proceedings of the SPIE - The International Society for Optical Engineering*, vol.2726, 698 (1996)
- [107] W. Primak, M. Bohmann, *Prog. Ceram. Sci.* 2, 103 (1962)
- [108] W. Primak, *The Compacted States of Vitreous Silica* (Gordon and Breach, New York, 1975)
- [109] W. Primak, *Phys. Rev.* 110, 1240 (1960)
- [110] I. Simon, "Structure of Neutron-Irradiated Quartz and Vitreous Silica", *Journal of The American Ceramic Society*, Vol. 40, 5, 150 (1957)

Chapter 2

Compaction Measurements Using Stress-Induced Birefringence and At-Wavelength (193nm) Interferometry

2.1 Introduction

Both stress-induced birefringence and interferometry have been used to study UV damage in fused silica. Compared with the traditional interferometry working at 633nm wavelength, the stress-induced birefringence method offers the advantage of simplicity as well as greater sensitivity. Also, stress-induced birefringence measurements are insensitive to surface quality and bulk inhomogeneities. However, the densification introduces an overall geometrical change in fused silica due to both bulk contraction and stress-induced surface indentation. Differentiating the bulk and surface effects is important in interpreting the stress-induced birefringence data. Interferometry provides a direct measurement of the optical-path-length difference (OPD), and it can be used to measure the surface indentation directly. Hence interferometry is well suited to characterizing the compaction in fused silica. In this chapter, I will review the stress-induced birefringence technique and discuss the first use of at-wavelength (193nm) interferometry for compaction measurement.

2.2 Stress-induced birefringence method

2.2.1 Experimental method

The basic concept behind the stress-induced birefringence technique is that directional refractive indices change when a sample is under stress. This phenomenon is described for isotropic materials by:

$$(n_y - n_x) = \Re(\sigma_y - \sigma_x) \quad (2-1)$$

where n_y and n_x are the refractive indices seen by light polarized in the (y) and (x) direction respectively; σ_y and σ_x are the stresses in the (y) and (x) directions and \Re is the stress-optic constant which is both material and wavelength dependent. For fused silica, \Re equals to $-3.5(\text{nm/cm})/(\text{kg/cm}^2)$ at 633nm wavelength [1].

The experimental approach used here was developed by Richard Schenker at UC-Berkeley, and a detailed description of this approach can be found in reference [2]. Fig. 2-1 shows the standard geometry used to irradiate a fused silica sample. The center irradiated region is compacted (region I). Resistance to this compaction by the unirradiated portion of the sample leads to stress in the sample (region II and III). Compaction-induced stress causes directional refractive index variations in the sample, which leads to birefringence and polarization scattering of incoming light. Changes in polarization of an initially linearly polarized Helium-Neon beam (He-Ne, $\lambda=633\text{nm}$) through a fused silica sample are measured to detect compaction-induced birefringence caused by the irradiation. Fig. 2-2 shows the configuration used to detect these changes. A high gain photodiode measures the 633nm reflectance of a thin calcium fluoride plate oriented at Brewster's angle to detect small changes in polarization resulting from UV-induced stress within the fused silica sample. The He-Ne polarization is such that the

plate has zero reflectance in the absence of birefringence. Spatial distributions of stress-induced birefringence is recorded by scanning the damaged fused silica sample through the He-Ne probe beam and measuring polarization shifts in and around the irradiated region.

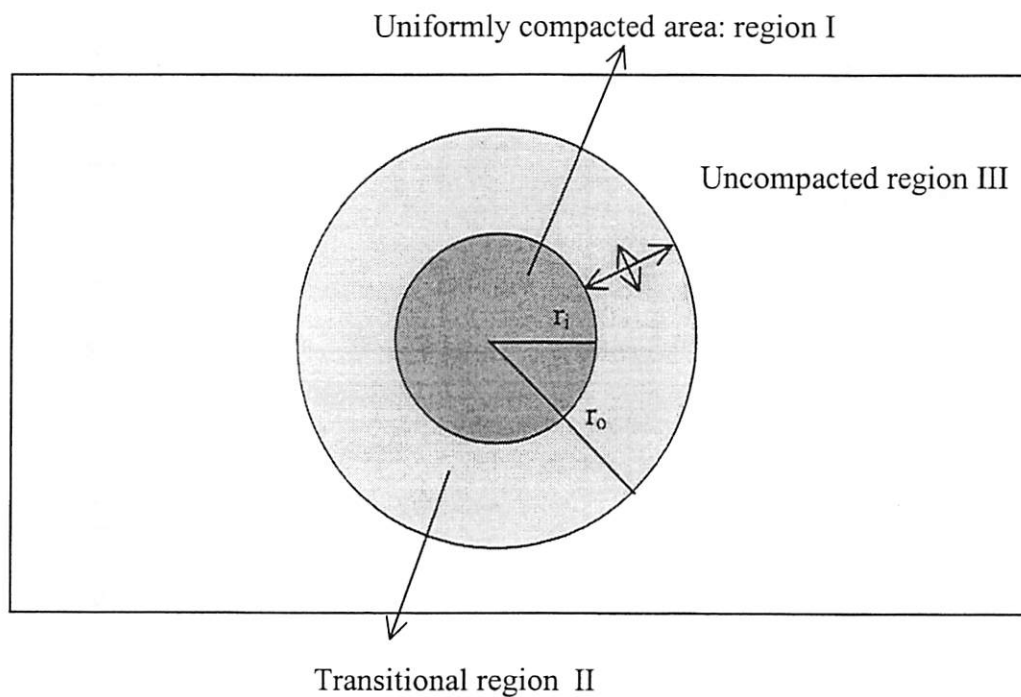


Figure 2-1. Schematic drawing of the geometry of damage spot on the samples.

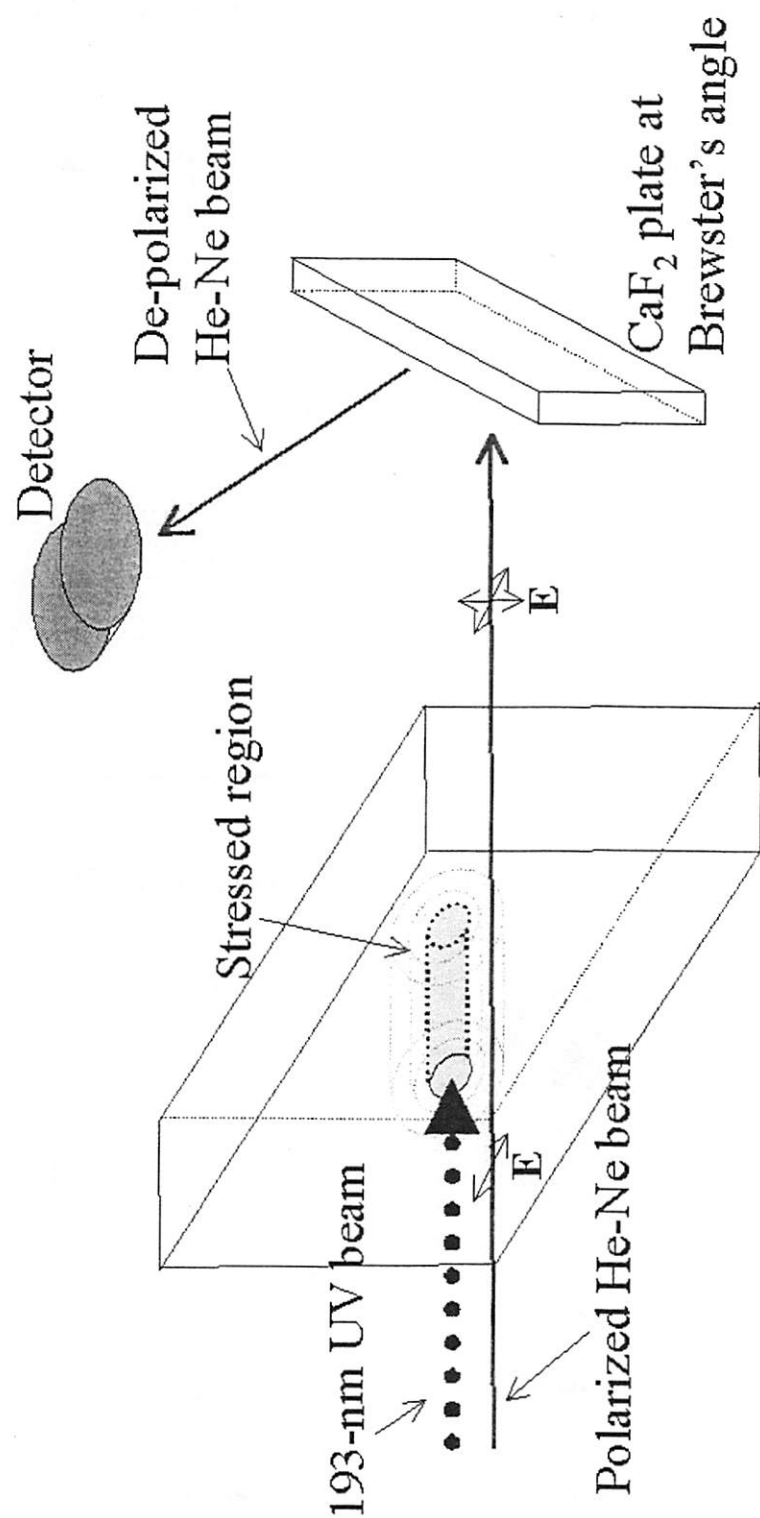


Figure 2-2. Schematic drawing of the experimental setup for 193nm UV-induced compaction tests.

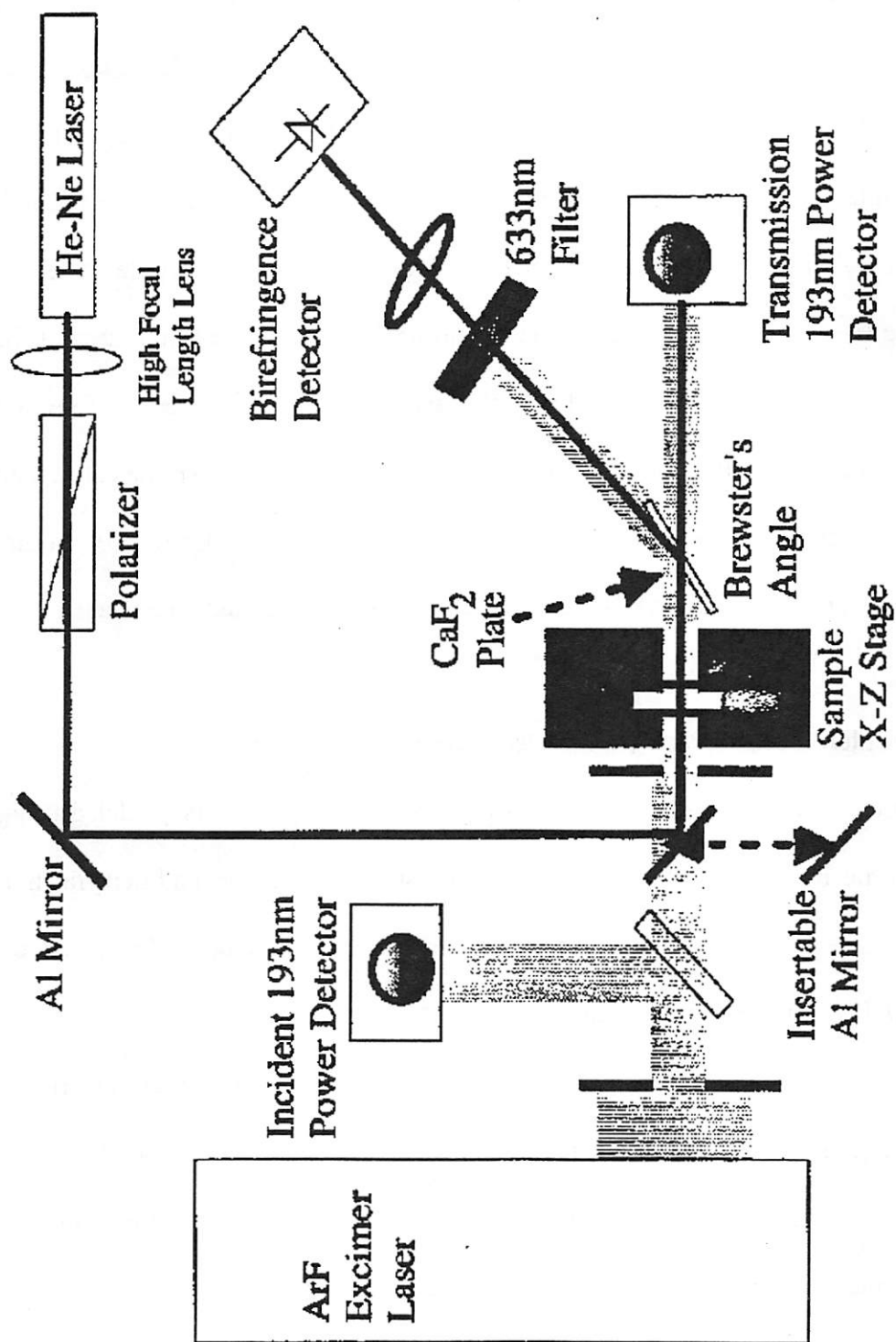


Figure 2-3. 193nm material damage testing instrumentation. A Z-stage inserts the He-Ne probe beam down the primary optical paths to scan for birefringence during exposure. Copied from reference [2].

The detailed experimental setup is illustrated in Fig. 2-3. The He-Ne probe beam is introduced into the primary beam line by reflection from a standard aluminum mirror that is inserted into the beam line via a mechanical stage. The birefringence is not monitored while the 193nm laser is firing, because the purity of the probe beam is improved by avoiding travel through any element before reaching the sample. A lens is used after the Brewster plate to focus the entire probe beam onto the active area of the photodiode. A second polarizer, crossed with the first, can be placed after the Brewster plate to further improve extinction of polarized light. Care is taken to keep the entire path of the He-Ne beam at the same height above the optical table in order to prevent any unwanted polarization shifts upon reflection off the mirrors used to guide the beam.

2.2.2 Three-region model for long cylindrical, large radius samples

The production of stress-induced birefringence by compaction is modeled using basic material mechanics. In order to extract the corresponding stresses and densification from birefringence distributions, a three-region stress model has been developed by Schenker *et al.* [2] assuming plane strain.

A three-region model is used with a uniformly compaction center region ($r < r_1$), an uncompacted region ($r > r_o$), and a transition region ($r_1 < r < r_o$) (Fig. 2-1). The notation used in this work will be that used in Shame and Cozzarelli [3] where ε is used for strains, u for displacements, and τ and σ are used interchangeably for stresses.

For the three region models, the following assumptions were made:

- 1) A circularly symmetric compacted region
- 2) Isotropic media

- 3) Large specimen so that surface boundary effects are small and all strain is in the plane perpendicular to the direction of the damaging beam (Plane Strain).
- 4) The compacted area is much smaller than the bulk so that stresses go to zero at the sample edge.
- 5) The body forces are zero (i.e.; gravitational effects are ignored)
- 6) Displacements are small, giving simple elastic behavior.

Shames *et al.* [3] derived the general solutions for stresses for an axially symmetric plane strain case using an Airy stress function. The use of the Airy stress function insures satisfying the compatibility equations so that the solutions for displacements are single-valued and continuous.

In polar coordinates, one obtains:

$$\tau_{rr} = K_1[\ln(r) - 0.5] + K_2 + K_3 / r^2 \quad (2-2)$$

$$\tau_{\theta\theta} = K_1[\ln(r) + 0.5] + K_2 - K_3 / r^2 \quad (2-3)$$

$$\varepsilon_{rr} = \frac{1-\nu^2}{Y} \left(\tau_{rr} - \frac{\nu \cdot \tau_{\theta\theta}}{(1-\nu)} \right) \quad (2-4)$$

$$\varepsilon_{\theta\theta} = \frac{1-\nu^2}{Y} \left(\tau_{\theta\theta} - \frac{\nu \cdot \tau_{rr}}{(1-\nu)} \right) \quad (2-5)$$

$$u_r = r \cdot \frac{1-\nu^2}{Y} \left(\tau_{\theta\theta} - \frac{\nu \cdot \tau_{rr}}{(1-\nu)} \right) \quad (2-6)$$

where K_1 , K_2 and K_3 are constants; ν is Poisson's ratio (0.17 for fused silica) and Y is Young's Modulus ($743 \times 10^3 \text{ kg/cm}^2$ for fused silica). The constants K_1 , K_2 and K_3 will be determined by the boundary conditions and are related to the total densification in the center region.

Application of boundary conditions for the three-region model is straightforward. To satisfy the physical requirement that stresses must be finite and by examining Eq. (2-2) and (2-3) for the center region, one obtains:

$$\text{Region I: } (r < r_i) \quad \tau_{rr} = \tau_{\theta\theta} = K_2 \quad (2-7)$$

In the outer region, stresses must go to zero as r approaches infinity so one obtains:

$$\text{Region III: } (r > r_o) \quad \tau_{rr} = K_3 / r^2 \quad (2-8)$$

$$\tau_{\theta\theta} = -K_3 / r^2 \quad (2-9)$$

In the transition region, the general solution for stresses are given by:

$$\text{Region II: } (r_i < r < r_o) \quad \tau_{rr} = D_1[\ln(r) - 1/2] + D_2 + D_3 / r^2 \quad (2-10)$$

$$\tau_{\theta\theta} = D_1[\ln(r) + 1/2] + D_2 - D_3 / r^2 \quad (2-11)$$

where K_2 , K_3 , D_1 , D_2 and D_3 are constants. When the boundary conditions are applied; the radial stress and the displacements are continuous at the two interfaces, the stress distribution become a function of a single unknown.

$$\tau_{rr}(r)_I = \tau_{\theta\theta}(r)_I = K_2 \quad (2-12)$$

$$\tau_{rr}(r)_{III} = [K_2(r_i^2 - r_o^2)]/[2r^2 \ln(r_i / r_o)] \quad (2-13)$$

$$\tau_{\theta\theta}(r)_{III} = [-K_2(r_i^2 - r_o^2)]/[2r^2 \ln(r_i / r_o)] \quad (2-14)$$

$$\tau_{rr}(r)_{II} = K_2[\ln(r / r_o) - 1/2 + r_i^2 / (2r^2)] / \ln(r_i / r_o) \quad (2-15)$$

$$\tau_{\theta\theta}(r)_{II} = K_2[\ln(r / r_o) + 1/2 - r_i^2 / (2r^2)] / \ln(r_i / r_o) \quad (2-16)$$

2.2.3 Using the compaction model to analyze birefringence distributions

The incident He-Ne beam is initially polarized in the E direction and propagates along Z direction (Fig. 2-4). It can be described as

$$\vec{E} = \vec{E}_0 \exp i(\vec{k} \cdot \vec{z} - \omega t) \quad (2-17)$$

This electric field can be decomposed into two orthogonal components. Here we decompose it along the radial and tangential directions in Fig. 2-4.

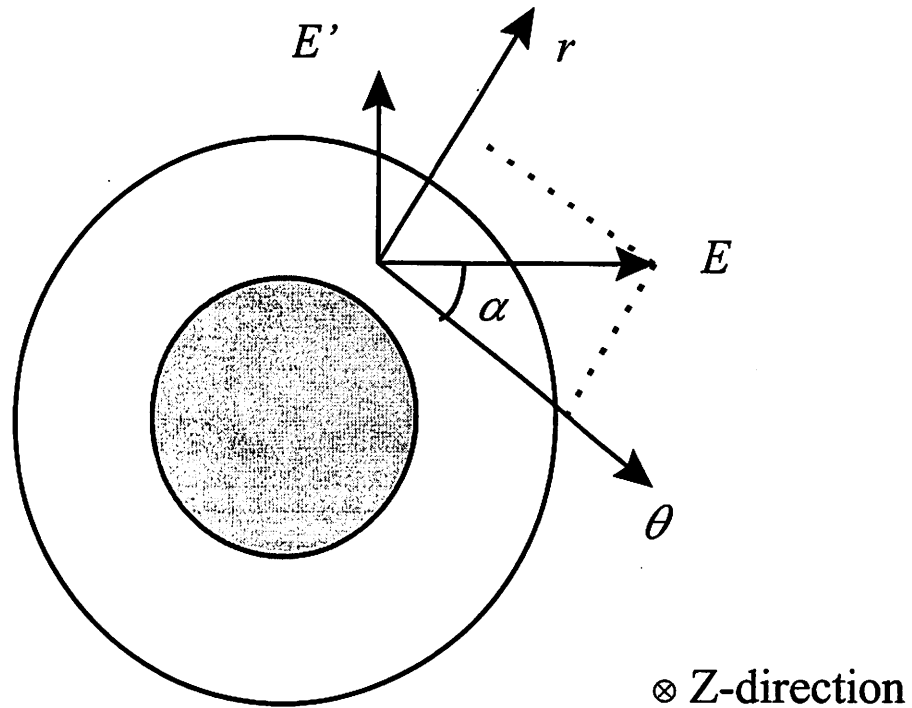


Figure 2-4. Vector definitions for birefringence analysis.

$$E_r = E \cos \alpha \quad (2-18)$$

$$E_\theta = E \sin \alpha. \quad (2-19)$$

After the beam has transited through the sample (path length L), there will be a phase difference for the above two components. This phase difference is from the stress induced refractive index change for r and θ directions, and can be calculated from

$$\chi = \frac{2\pi}{\lambda} [\Re L(\sigma_r - \sigma_\theta)]. \quad (2-20)$$

The outgoing beam can be described as:

$$E_r = E \cos \alpha \quad (2-21)$$

$$E_\theta = E \sin \alpha \exp(i\chi).$$

Since we put a CaF_2 plate at Brewster's angle relative to the E direction behind the sample, ideally, we can not detect any E component of the outgoing electric field. But we should be able to detect the E' component of the outgoing electric field. We find that after the incident He-Ne beam transmits through the compacted area, the E' component is no longer zero; it is given by

$$|\vec{E}'| = |E \cos \alpha \sin \alpha \exp(i\chi) - E \cos \alpha \sin \alpha| \quad (2-22)$$

Since we just detect the intensity of the beam, $I \propto |\vec{E}'|^2$, we find:

$$I \propto E_0^2 \sin^2(2\alpha) \sin^2\left(\frac{\chi}{2}\right) \quad (2-23)$$

When the compaction is very small (as in our case), we use $\sin(\frac{\chi}{2}) \approx \frac{\chi}{2}$, and the detected birefringence signal can be expressed as:

$$I = I_0 \sin^2(2\alpha) \frac{\chi^2}{4} \quad (2-24)$$

where I_0 is the intensity of the incident He-Ne beam.

Combining Eq. (2-20) with Eq. (2-24), we find

$$\frac{I}{I_0} = \sin^2(2\alpha) \left[\frac{\pi R L (\sigma_r - \sigma_\theta)}{\lambda} \right]^2, \quad (2-25)$$

the maximum depolarization occurs when the probe He-Ne beam is oriented at 45° with respect to the principal stress axes ($\alpha = 45^\circ$) and at the edge of the compacted region (boundary of region II and region III in Fig. 2-1). The value of

$$(\sigma_r - \sigma_\theta)|_{r=r_0} = K_2 \frac{r_i^2 - r_0^2}{r_0^2 \ln(\frac{r_i}{r_0})} = \eta K_2. \quad (2-26)$$

So the maximum fraction of depolarization is given by

$$\left(\frac{I}{I_0} \right)_{\max} = \left(\frac{\eta K_2 \pi R L}{\lambda} \right)^2 \quad (2-27)$$

2.2.4 Example experimental result

Fig. 2-5 shows a measured birefringence distribution for a sample irradiated by a 3mm diameter 193nm beam with 12 million 1.05mJ/cm^2 pulses applied. The four peaks correspond to locations where the probe beam polarization is at 45° with respect to the principal stress axes. The z-coordinate is directly proportional to the current produced by the photodiode detecting the reflectance of the Brewster plate used in the experimental setup.

A computer program (developed by Schenker) is used to fit the calculated birefringence distribution from the three-region stress model to the measured birefringence distributions by adjusting the level of stress in the center region to the optimum magnitude. The locations of the boundary (r_i and r_0 in Fig. 2-1) were selected as

the 90% and 10% intensity radii as measured by a CCD camera (typical values are 1.4mm and 1.56mm).

Fig. 2-6 shows the best fit of the three-region stress model to the data in Fig. 2-5. The center radial stress (K_2) corresponding to the birefringence distribution in Fig. 2-5 is 0.030 kg/cm².

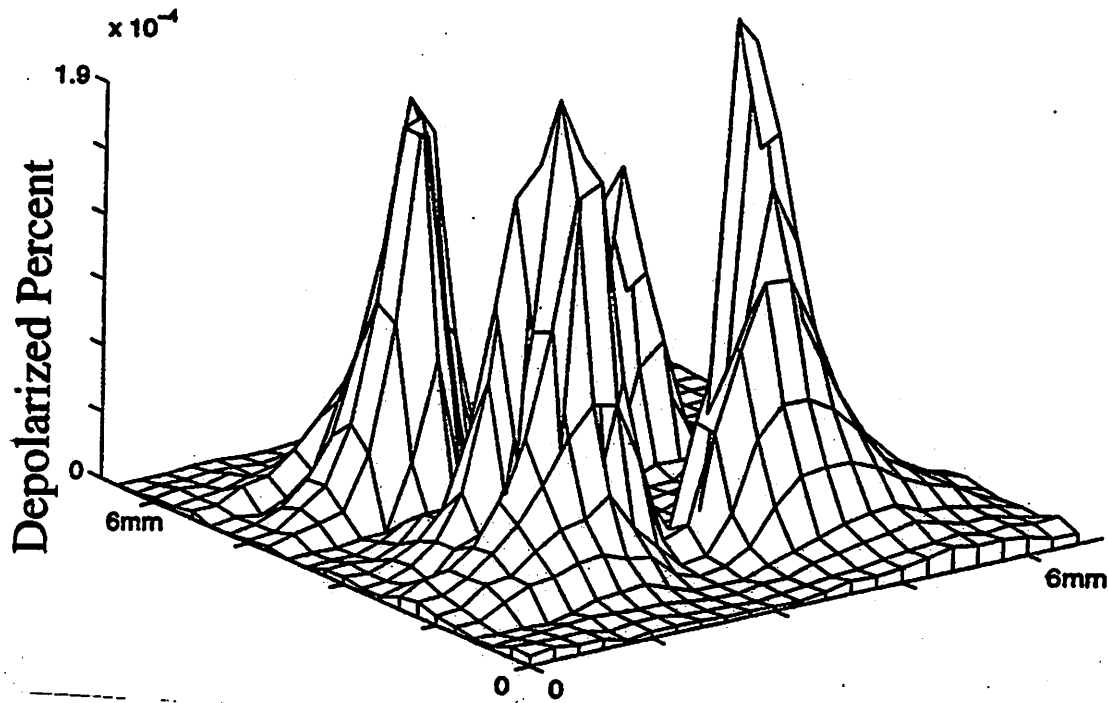


Figure 2-5. Measured birefringence for linearly polarized light (at 633nm) scanned across a 6.6 mm² sample region which has been exposed to 3mm diameter 193nm excimer laser beam (12 million pulses, 1.05mJ/cm²). Copied from reference [2].

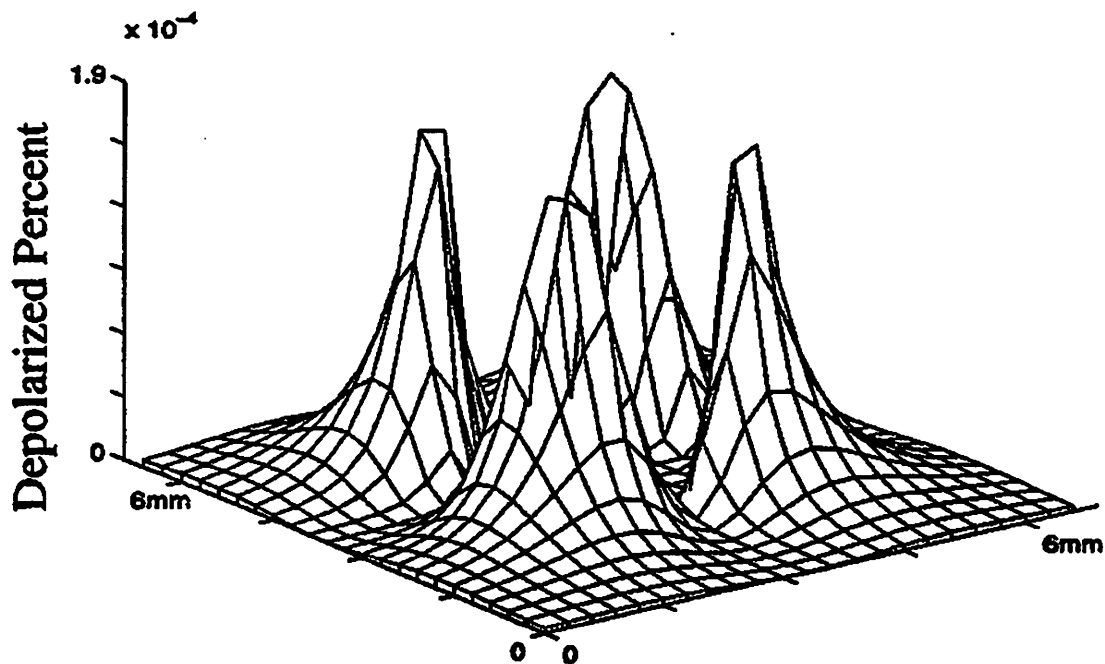


Figure 2-6. Simulated birefringence for the same sample assuming a 95ppB densification (using a plain strain compaction model) in a 3mm-diameter compaction zone. Copied from reference [2].

Before we proceed, we have to define a quantity; unconstrained compaction $(\frac{\Delta\rho}{\rho})_u$, the relative density change that would be produced in the sample if the samples were irradiated uniformly. Because only a small area of the sample is irradiated in our tests, the net density change is less than $(\frac{\Delta\rho}{\rho})_u$ owing to the resistance of the undamaged portion of the sample to displacements from the compacted region (Fig. 2-1). The

unconstrained compaction serves as the best standard description of the compaction for comparison with other testing techniques [4].

In order to calculate the compaction level of the damaged area from the stress solution, Schenker *et al.* [2] have used a simplified two-region model to develop the analytical relation between these two quantities. The two-region model includes an inner region that has been uniformly compacted and the outer region that has an unchanged density for infinitesimal kinematics. The shortcoming of this two-region model is that it gives an abrupt transition from compacted to uncompacted material. It requires a uniform laser beam profile with a sharp cutoff in intensity, but we know this is very difficult to achieve in reality.

According to the two-region model, the relation between unconstrained densification and the center stress (K_2) is:

$$\left(\frac{\Delta\rho}{\rho}\right)_u = \frac{6(1-\nu)}{Y} K_2 \quad (2-28)$$

and the net density change is given by:

$$\frac{\Delta\rho}{\rho} = \frac{2(1+\nu)}{Y} K_2 \quad (2-29)$$

Finite Element Analysis (FEA) simulations were performed by Schenker to confirm the validity of the above two-region stress model [2]. Numerical solutions were found to agree with the analytical solution with high accuracy. In this thesis, I will use Eq. (2-28) to calculate the density change in fused silica samples.

For the birefringence distribution in Fig. 2-5, the unconstrained and net densifications are 200ppB and 95ppB respectively. This level of compaction would only produce about 1/500 of a wavelength (633nm) OPD through the sample. This is very

difficult to measure with conventional interferometry (at 633nm wavelength) using a perfect sample and virtually impossible for a sample with imperfect surface polish or bulk inhomogeneties.

2.3 Phase-shifting point diffraction interferometer at 193nm wavelength

2.3.1 Description

Fig. 2-7 shows a schematic drawing of a phase-shifting point diffraction interferometer implemented at the wavelength of 193nm to test flat fused silica samples.

This work has been done in collaboration with S. H. Lee [5].

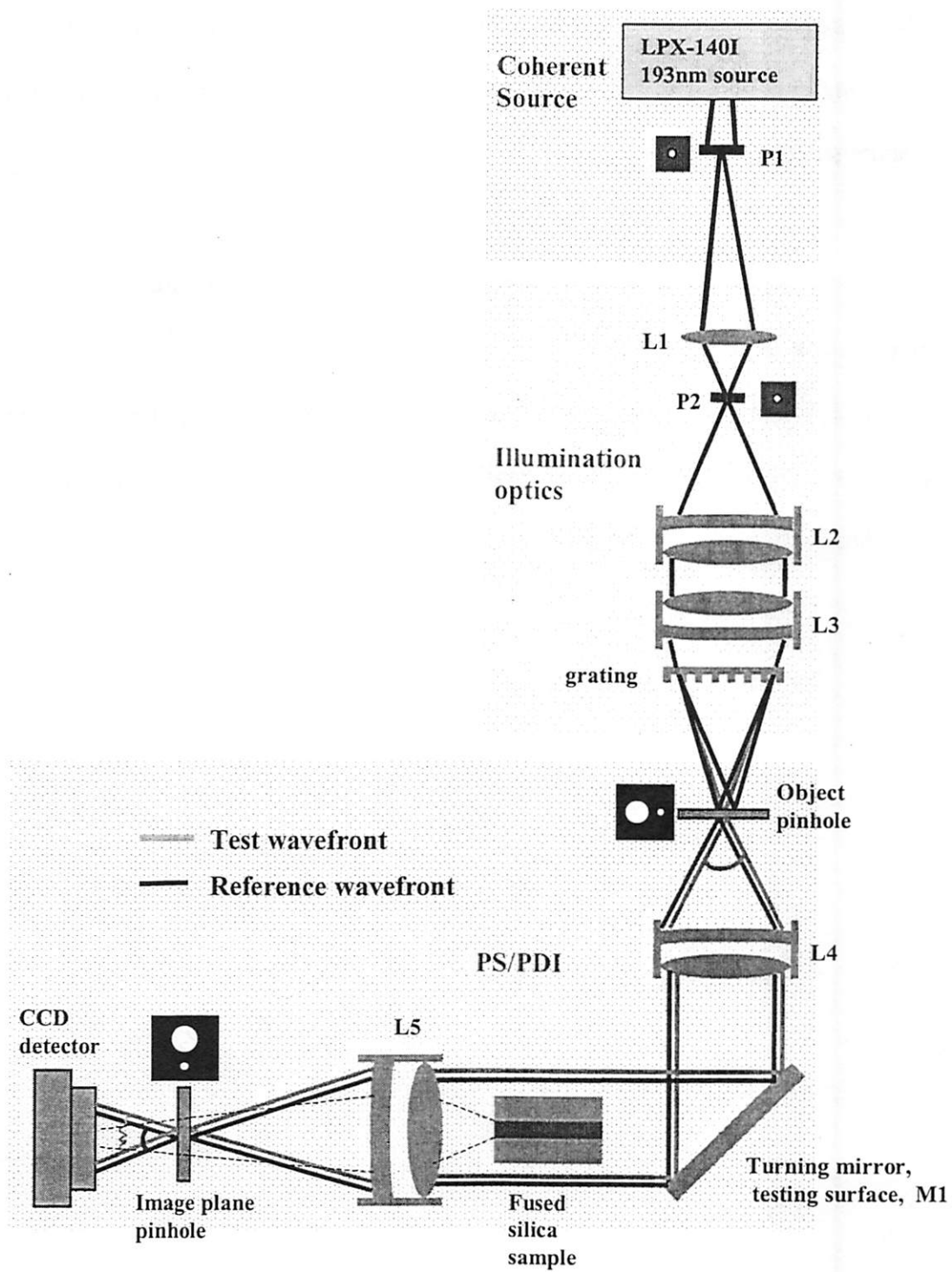


Figure 2-7. At-wavelength (193nm) PS/PDI set-up to test UV-induced damage of flat fused silica samples. Copied from reference [5].

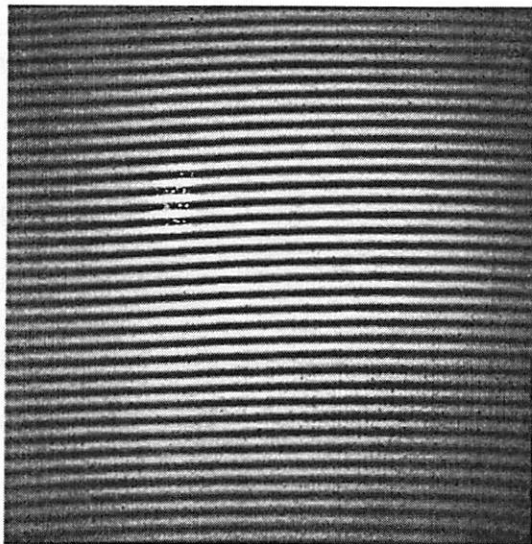
Our Lambda-Physik LPX-140I pulsed ArF excimer laser was used as the illumination source. Owing to the spatially incoherent nature of this laser source, spatial filtering was used to provide sufficiently coherent illumination of the interferometer. A dual-pinhole-filtering scheme was used to avoid laser damage. A $400\text{ }\mu\text{m}$ pitch chrome-on-glass diffraction grating is inserted into the illumination system to act as a beam splitter, producing a $120\text{ }\mu\text{m}$ beam separation in the object plane. An object-plane mask containing a $120\text{ }\mu\text{m}$ square window and a $2\text{ }\mu\text{m}$ spatial filtering pinhole is placed in the object plane to select two of the orders of the beam diffracted by the grating. The window to pinhole center-to-center separation is $120\text{-}\mu\text{m}$. The first-order diffracted beam passes through the window and will eventually serve as the reference beam, whereas the zeroth-order beam passes through the pinhole filter providing the nearly-perfect spherical illumination to be used as the testing beam.

The two beams propagate through the silica sample under test, acquiring aberrations imparted by the sample and are focused to the image plane. In the image plane, a second mask containing a window and small pinhole is placed. The reference beam passes through the pinhole filter removing aberrations imparted by all upstream components, thus generating an essentially spherical reference wave. The test and reference beams propagate to the detector plane where they overlap producing an interference pattern. The recorded interferogram yields information on the deviation of the test wavefront from the nominally spherical reference wavefront.

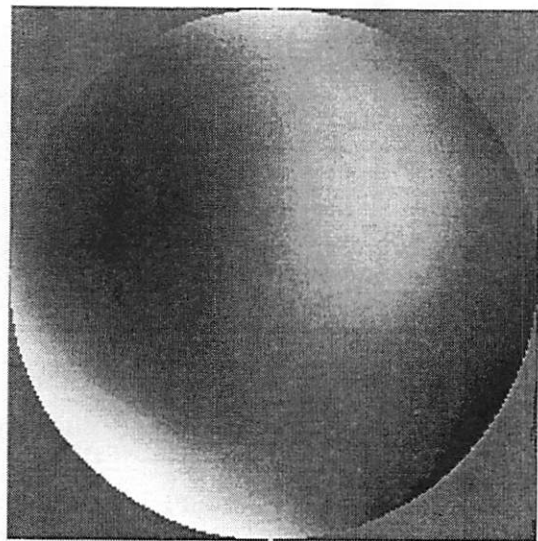
2.3.2 Direct OPD measurement of UV-damaged fused silica samples

To provide high-accuracy measurements it is important to calibrate the system. This has been achieved here by way of a null test. The null test involves simply

performing the measurement without the refractive sample installed. With no refractive sample, the interferometer measures the overall aberrations in the system. This serves as a calibration measurement for systematic errors in the interferometer. A representative calibration interferogram is shown in Fig. 2-8(a). The corresponding wavefront map [6,7] over a 0.04 numerical aperture, with piston, tilt, and defocus removed, is depicted in Fig. 2-8(b). The 0.04 numerical aperture corresponds to an 18mm diameter sample space. The peak-to-valley aberration is 0.3 waves (57.9nm) and the rms value is 0.05 waves (9.65 nm). Repeatability tests based on 50 measurements show the precision to be 0.004 waves (0.03nm) rms.



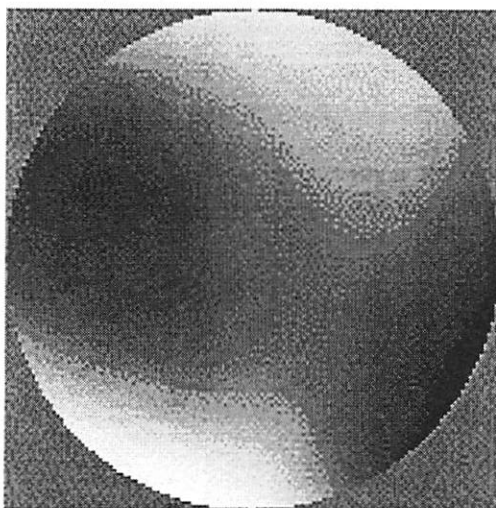
(a)



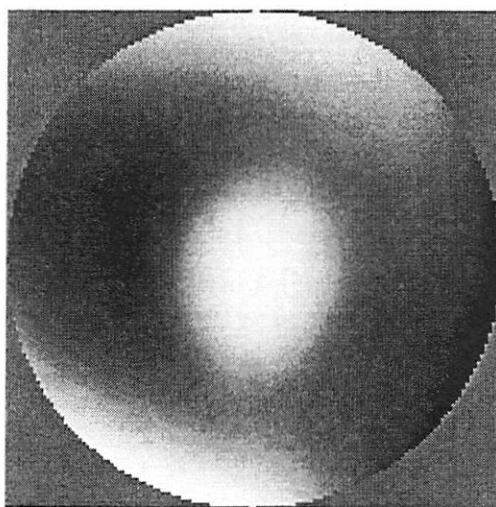
(b)

Figure 2-8. (a) Calibration interferogram obtained with no test sample installed. (b) The reconstructed calibration wavefront from the (a) interferogram. The peak to valley wavefront aberration is 0.3 waves and the rms aberration is 0.05 waves at 193 nm wavelength over a numerical aperture of 0.04 (representing a diameter of 18 mm in sample space). Copied from reference [5].

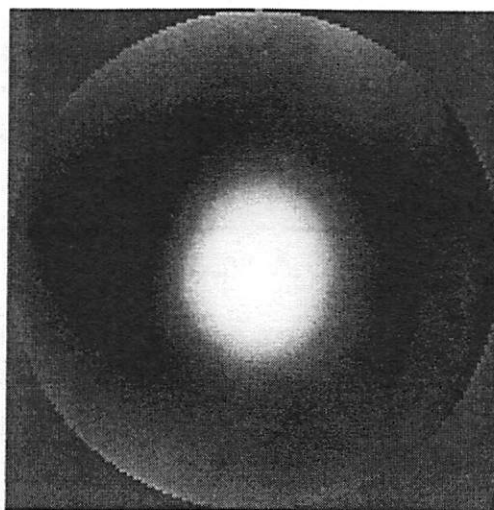
Fig. 2-9 shows a wavefront for a sample (1cm thick) irradiated by a 5mm diameter 193nm beam with 8.5 million $12\text{mJ}/\text{cm}^2$ pulses applied. To remove the systematic effects and isolate the effect of the UV damage, the difference wavefront between the before [Fig. 2-9(a)] and after [Fig. 2-9(b)] damage results is calculated and displayed in Figs. 2-9(c). Fig. 2-10 shows a line scan through the center of the difference wavefronts, given in Fig. 2-9(c).



(a)



(b)



(c)

Figure 2-9. Measured wavefront from tested sample. (a) Before UV radiation damage. (b) After UV radiation damage. (c) Difference between the before and after damage wavefronts.

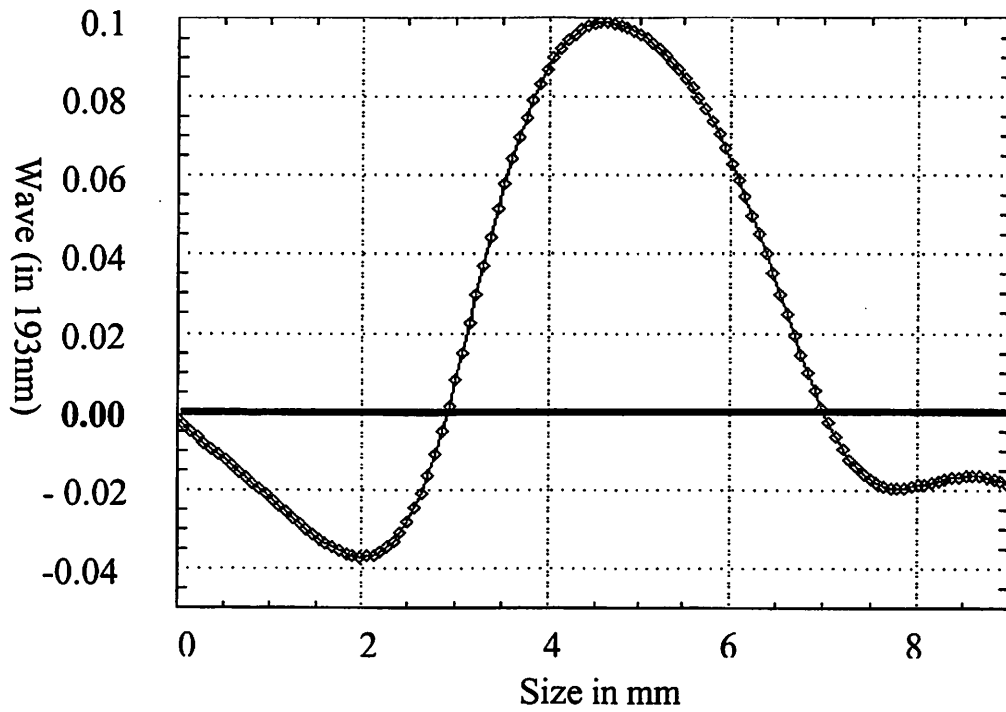


Figure 2-10. Wavefront-center cross-section for difference wavefronts shown in Fig. 2-9(c). The x-axis indicates the size of the damaged region in mm and y-axis indicates the OPD in waves at 193 nm.

The changes seen in Fig. 2-9 and 2-10 are owing to two effects: an index of refraction change and surface indentation due to volume contraction. These two effects, however, cause changes of opposite sign to the OPD. An increase in refractive index yields a positive OPD while volume compaction generates a negative OPD. In Fig. 2-10, we were able to directly observe the spatial variation of OPD, clearly showing the reduction in OPD outside the damaged region (because of the surface indentation) in contrast to the density-driven OPD increase inside the damaged area.

The overall OPD before and after the damage can be described by following equation;

$$\text{OPD} = \Delta L(n_{\text{air}} - n_{\text{fused silica}}) + \Delta n(L - \Delta L) \quad (2-30)$$

where ΔL , Δn , and L indicate the surface indentation, refractive index change, and the sample thickness respectively. The minimum magnitude points in Fig. 2-10 indicate the positions where the surface indentation effect and refractive index effect are balanced. By choosing this balanced point as the cut-off line, ΔL can be extracted, and it is calculated to be about 10 nm. With this approximation, the peak $\Delta n/n$ is found to be 1.6 ppm for this sample. This agrees with the earlier analysis by Schenker that the OPD change from surface depression is about 30% of the total OPD change (opposite sign) for 1-cm thick samples. For thicker samples (along the path length of DUV beam), the surface effect is relatively less important than the bulk effect [2]. Doug Allan of Corning showed by means of finite-element analysis that the relative role of surface and bulk effects is entirely predicable from the material properties [8,9], and his results are consistent with Schenker's analysis. The Corning group also directly measured

birefringence in their UV-damaged fused silica samples, and found that interferometric (at 633nm wavelength) data gave the same compaction levels [8,9].

2.4 Conclusions

Stress induced birefringence is used to detect very low levels of compaction in fused silica. It proved to be an efficient technique to monitor the compaction development in real time. In order to extract the compaction levels from the birefringence distributions, a three-region analytical model was constructed by Schenker *et al.* [2] based on the UV beam profile. Basic electromagnetic theory is applied to calculate the birefringence distribution from the model stress distributions. The calculated birefringence distribution using stress described by the three-region stress model agrees with measured birefringence distributions. By using the stress model to extract densification levels from birefringence measurements, one can measure compaction at level order of magnitude smaller than that resolvable with conventional interferometry.

The validity of using the stress-induced birefringence to measure the UV-induced compaction in fused silica is directly verified by the 193nm PS/PDI measurement of the OPD change in the damaged samples. The 193nm PS/PDI is a significant improvement over earlier point diffraction interferometers in that it has much greater optical throughput and provides higher resolution [10]. A particular advantage of the upstream grating configuration of the PS/PDI is that it provides beam equalization [7] allowing high-contrast interferograms to be recorded, and thereby improving the signal-to-noise ratio of the measurement.

2.5 References:

- [1] W.Primak, D.Post, "Photoelastic constants of vitreous silica and its elastic coefficient of refractive index", J. Appl. Phys. 30(5), 779 (1959)
- [2] R.Schenker, Ph.D. Dissertation, UC-Berkeley (1997)
- [3] I.H.Shames, F.A.Cozzarlli, "Elastic and inelastic stress analysis", Prentice Hall Inc. (1992)
- [4] As suggested by Douglas Allan of Corning Inc. at the Second International Symposium on 193nm Lithography in Colorado Springs, Colorado (1996)
- [5] S.Lee, F.Piao, P.Naulleau, K.A.Goldberg, W.G.Oldham, J.Bokor, "Direct measurement of deep ultraviolet radiation-induced fused silica damage with at-wavelength interferometry", to be published
- [6] E.Tejn timer, Ph. D. Thesis, UC-Berkeley (1998)
- [7] K.A.Goldberg, Ph. D. Thesis, UC-Berkeley (1998)
- [8] D.C.Allan, C.Smith, N.F.Borrelli, T.P.Seward,III, "193-nm excimer-laser-induced densification of fused silica". Optics Letters, vol.21, (no.24) (1996)
- [9] N.F.Borrelli, C.Smith, D.C.Allan, T.P.Seward,III, "Densification of fused silica under 193-nm excitation". Journal of the Optical Society of America B (Optical Physics), vol.14, (no.7), 1606 (1997).
- [10] H.Medecki, E.Tejn timer, K.A.Goldberg, J.Bokor, "A phase-shifting point diffraction interferometer", Optical Letters, 21(19), 1526 (1996)

Chapter 3

Compaction Data for Various Fused Silica Samples

3.1 Introduction

In this chapter, I will report the experimental compaction rate at 193nm wavelength for various fused silica samples. For all of the samples we tested, a universal empirical relation between compaction rate and absorbed UV dose exists. This relation is consistent with the earlier observations in fused silica for other types of ionizing radiation.

3.2 Two-photon absorption mechanism

At 193nm wavelength, two-photon absorption is the source of UV damage in fused silica. This point becomes more intuitive when we consider that the effective energy band gap of fused silica is about 8.3 eV [1], while the photon energy at 193nm is about 6.4 eV, i.e.; two UV-photons are required to exceed the band gap barrier. So, a two-photon ionization process is believed to be the catalyst for UV-induced compaction in fused silica [1]. Earlier experiments of a super-linear dependence of damage rates on laser intensity [1-6] and compaction rates scaling with the two-photon absorption coefficient at the radiation wavelength [3] support this model.

For a two-photon ionization process, the effective dose is given by [4]

$$D_a = \alpha \frac{NI^2}{\tau} \quad (3-1)$$

where α is the two-photon absorption coefficient at 193nm for fused silica which is measured to be 2.0×10^{-3} cm/MW [7], N is the pulse count, I is the pulse energy

intensity, τ is the effective pulse duration and is a constant which depends on the operation condition of the laser.

For our Lambda-Physik LPX-140I laser, the pulse profiles have been measured at different operating frequencies and operating voltages [Fig. 3-1(a), 3-1(b)]. The effective τ can be calculated using the integral average method suggested by R. Sandstrom [8].

$$\tau = \frac{\int_0^{\infty} E dt}{\int_0^{\infty} E^2 dt} . \quad (3-2)$$

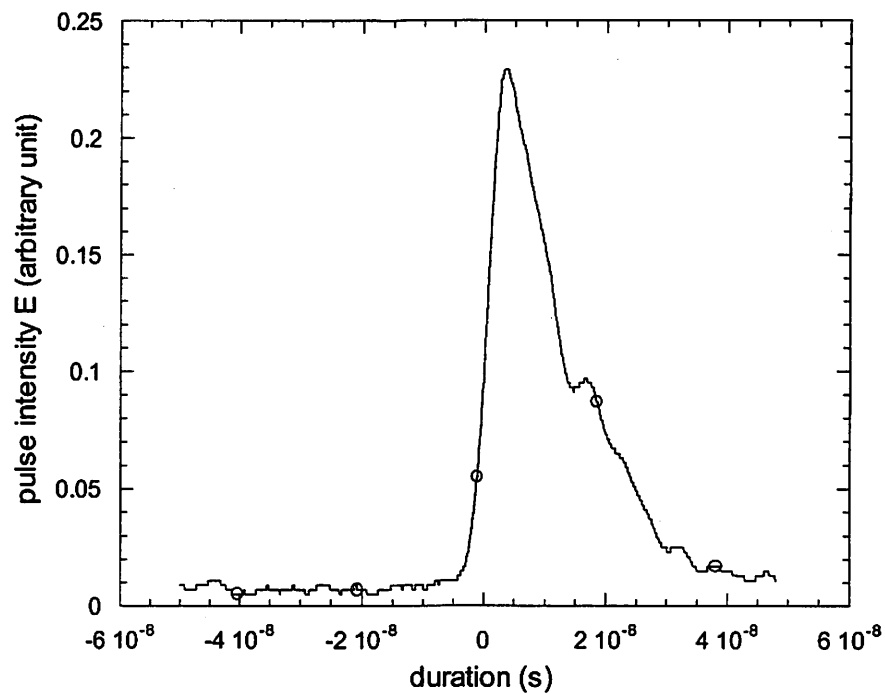


Figure 3-1(a). Temporal profile of the 193nm beam at 22kV, 20 Hz.

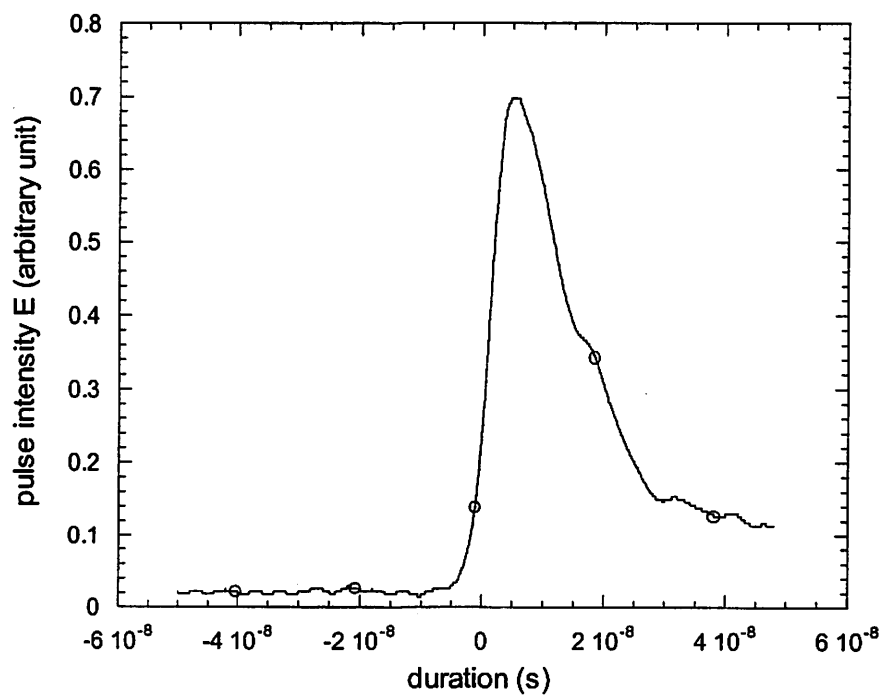


Figure 3-1(b). Temporal profile of 193nm excimer laser beam at 22kV, 333Hz.

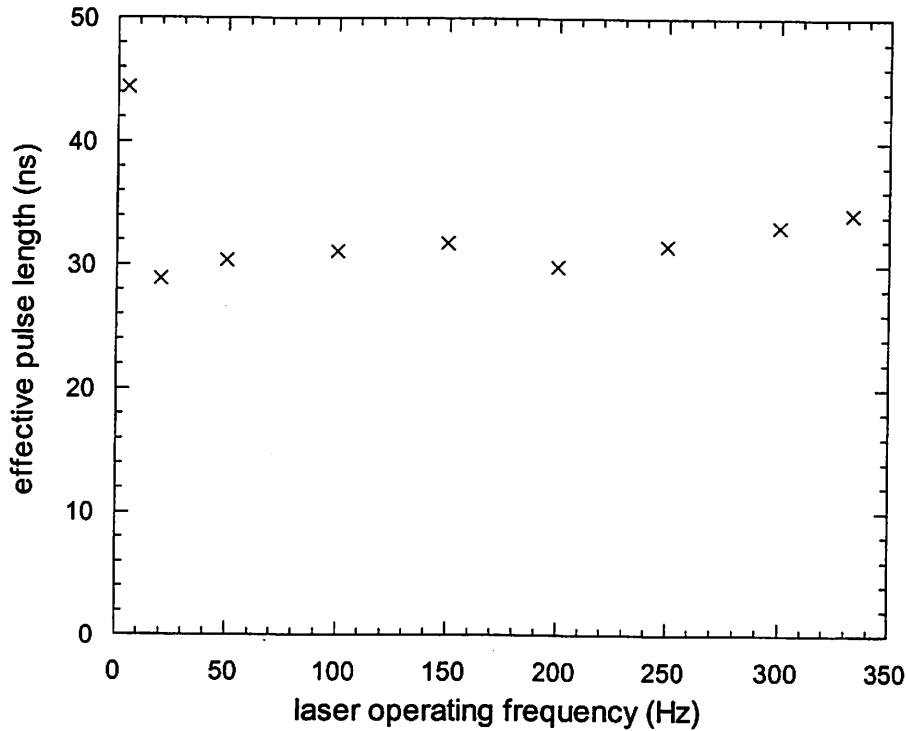


Figure 3-2. Effective pulse duration at different operating frequency.

In Fig. 3-2, we plot the effective pulse length as a function of laser operating frequency. At 330Hz and 22 kV (testing condition), τ is about 30ns.

3.3 Experimental set-up and preliminary results

In our experiments, 3-mm diameter cylindrical regions within fused silica samples were exposed to ArF excimer laser radiation at a repetition rate of 330Hz. We limited the UV beam size to about 3mm in diameter to ensure the beam intensity uniformity, and peak-to-valley intensity differences with the attenuated spatial profiles of the beam varied by no more than 10% as measured by a charge-coupled device (CCD) camera. A linearly polarized Helium-Neon (He-Ne) laser beam was used to measure

stress-induced birefringence in and around the irradiated region. The densification levels corresponding to the birefringence distribution were extracted by using a three-region stress model as discussed in Chapter 2.

The experimental data in Fig. 3-3, 3-4 and 3-5 have been reported by Schenker [9]. He used 11 ns (FWHM value of laser pulse) as the pulse duration τ . In this chapter, I plot the same data again by using the effective τ (30 ns) calculated from Eq. (3-2). Fig. 3-3 shows the compaction testing result for sample of Corning 7940 fused silica at five different pulse energy density levels. We used (NI^2/τ) as the effective dose coordinate. We can clearly see that for different pulse energy density levels, all the data lie on a single universal curve described by

$$\left(\frac{\Delta\rho}{\rho}\right)_u = A' \left(\frac{NI^2}{\tau}\right)^c. \quad (3-3)$$

In Fig. 3-4, we plot the compaction data in Fig. 3-3 on a log-log scale to extract the power parameter c and found it to be about 0.66 (2/3). To test the universality of the single relation seen in Fig. 3-3, a different sample was tested over a similar range of pulse densities. As seen in Fig. 3-5, similar damage behavior is also observed for Suprasil 311, in this case, c is also about 0.66.

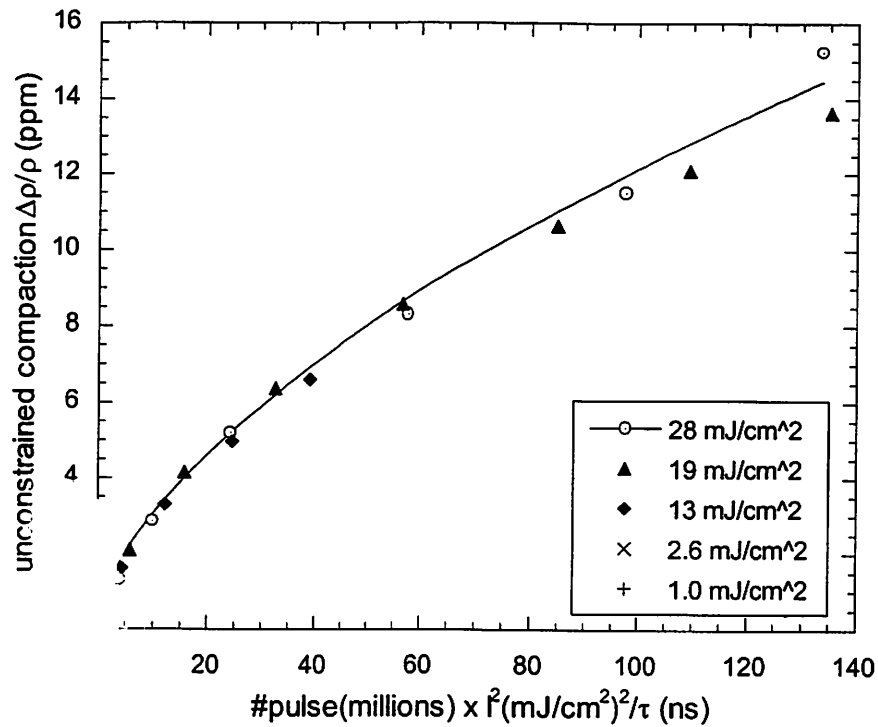


Figure 3-3. Unconstrained densification in Corning 7940 for five different pulse energy densities versus number of pulses times the pulse energy density squared divided by the pulse length.

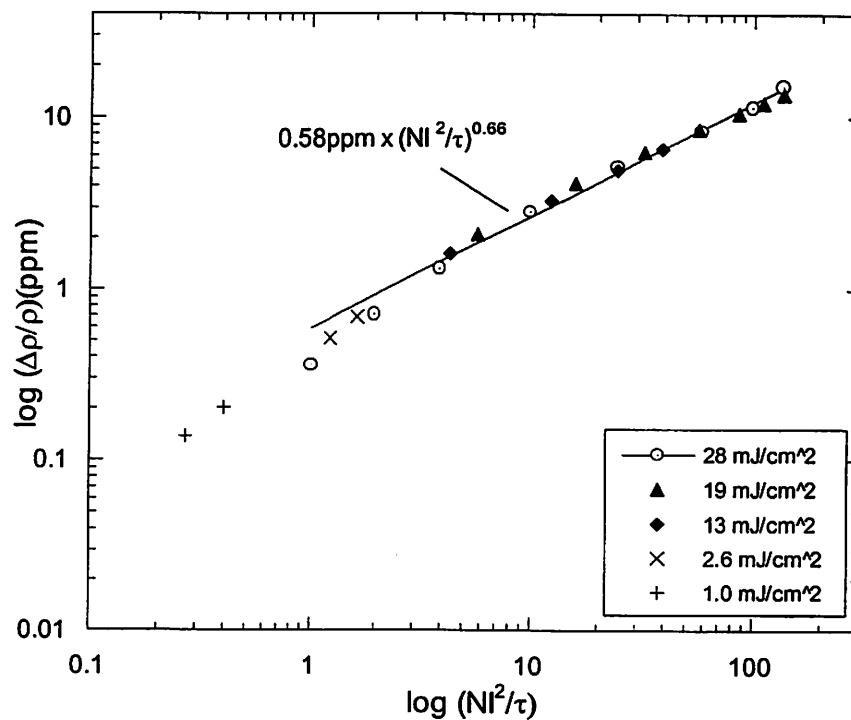


Figure 3-4. Unconstrained densification in Corning 7940 for five different pulse energy densities versus number of pulses times the pulse energy density squared divided by the pulse length. (log-log scale)

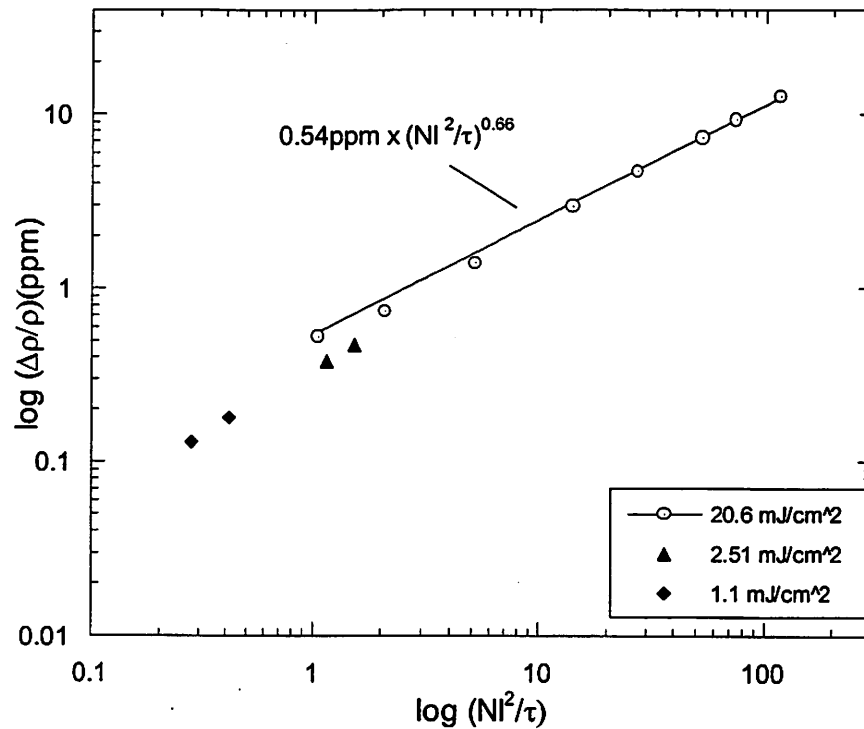


Figure 3-5. Unconstrained densification in Suprasil 311 for three different pulse energy densities versus number of pulses times the pulse energy density squared divided by the pulse length. (log-log scale)

These tests clearly show that the UV radiation induces compaction in silica through a two-photon absorption mechanism. For each type of sample, a universal sub-linear relation [Eq. (3-3)] can be found with a dose exponent c of 0.66. Schenker generally use a dose exponent of 0.7, which provides an equally good fit to the data [9].

3.4 Comparison of compaction rates

Within a SEMATACH program to improve the durability of fused silica for 193nm lithography, we tested more than 14 different types of fused silica samples. Here, I will list the testing results for six types of 1995-1996 experimental fused silica because they are the best quality samples regarding homogeneity and surface quality. The

birefringence data we got from these samples are more symmetric compared with other samples, and this makes the compaction level extraction more accurate (see Chapter 2). These samples are modified versions of Corning 7940, Corning 7980, Suprasil 311, Suprasil 1, Shin-Etsu X103, and Shin-Etsu X103A [10]. The materials are almost totally free of metallic impurities but contain about 1000ppm OH except Suprasil 311 with about 200 ppm OH content. The samples were randomly labeled A, B, C, D, E, and F in accordance with the wishes of the suppliers. They are all of 4x2x1cm in size, polished on all six sides. In these tests, the UV incident beam is along the 1cm direction.

I plot the compaction data for all the six type samples in Fig. 3-6. The data for sample C was taken from reference [9]. The compaction follows the sub-linear power relation as Eq. (3-3) and the total compaction at a given dose parameter varying by a factor of about two among all the fused silica samples tested. In order to extract the dose exponent c for these samples, we plot the data in Fig. 3-6 in log-log scale [Fig. 3-7(a), 3-7(b) and 3-7(c)]. We list the best curve fitting results in the Table 3-1.

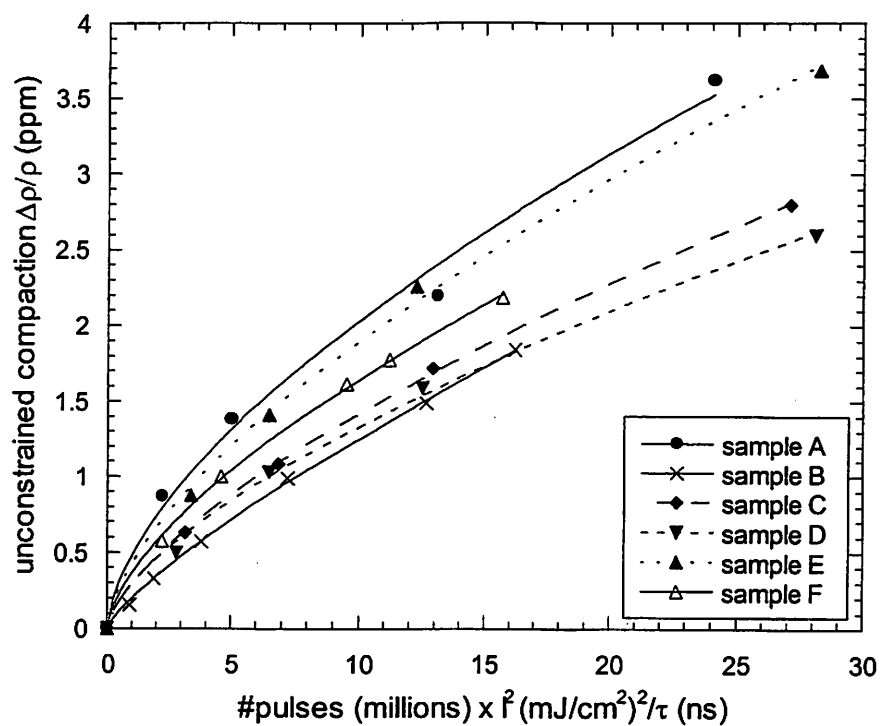


Figure 3-6. Unconstrained densification in experimental fused silica A-F versus number of pulse times the pulse energy density squared divided by the pulse length.

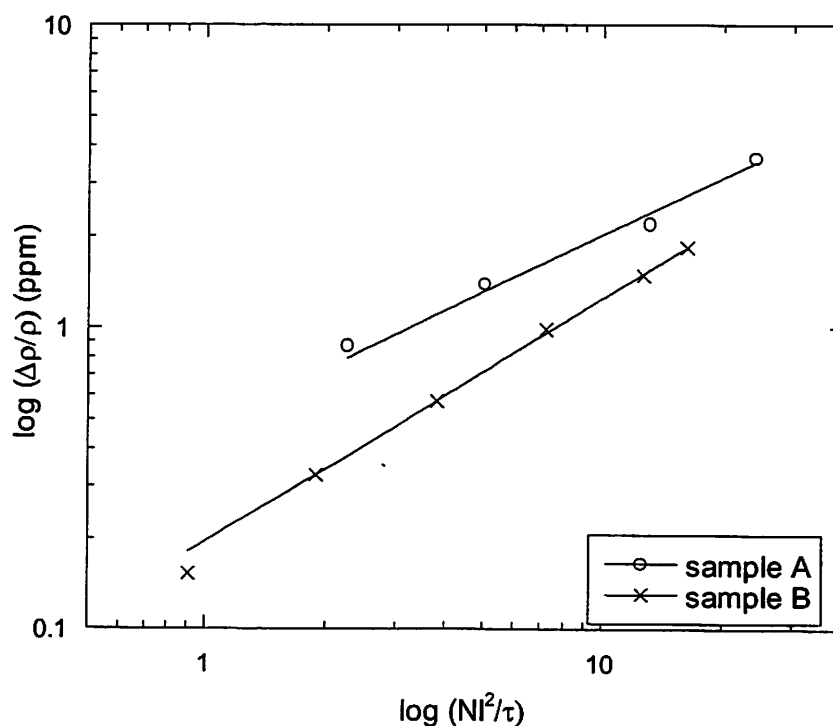


Figure 3-7(a). Unconstrained densification in sample A and B versus number of pulses times the pulse energy density squared divided by the pulse length. (log-log scale)

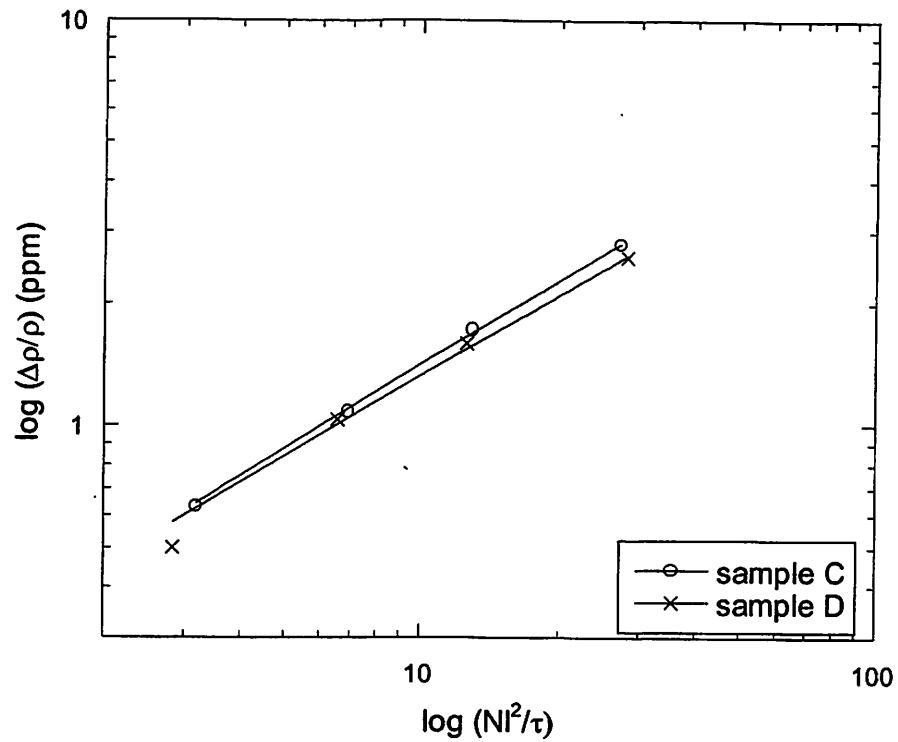


Figure 3-7(b). Unconstrained densification in sample C and D versus number of pulses times the pulse energy density squared divided by the pulse length. (log-log scale)

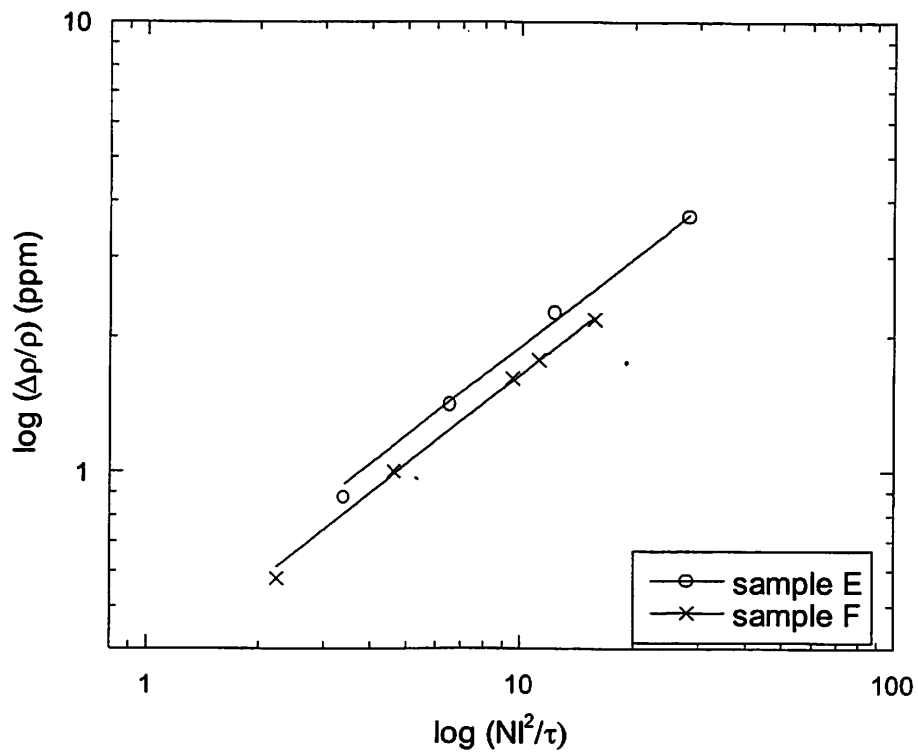


Figure 3-7(c). Unconstrained densification in sample E and F versus number of pulses times the pulse energy density squared divided by the pulse length. (log-log scale)

Table 3-1

Curve Fitting Parameters for Different Fused Silicas

$$\text{(Compaction Data fit to } (\frac{\Delta\rho}{\rho})_u = A'(\frac{NI^2}{\tau})^c \text{)}$$

Fused Silica	Parameter A' (ppm)	Parameter c
Type A	0.47	0.63
Type B	0.195	0.80
Type C	0.32	0.68
Type D	0.29	0.66
Type E	0.42	0.65
Type F	0.36	0.66

From Table 3-1, we see that even though different fused silica samples may have gone through very different manufacturing processes, their UV-induced compaction behaviors are very similar. The material dependent parameter A' varies over a relatively wide range but c is very close to 0.66 for all samples except sample B. For three pieces of type B we tested, c lies between 0.72 and 0.80. In Chapter 6, I will discuss the mechanism of UV-induced-compaction. There, we will understand that some special treatments can be done in order to increase the compaction resistance in fused silica, such as pre-compressing the material. These treatments may affect the internal structure and therefore affect the “structure dependent” parameter c . Since the sample B is the most UV-compaction resistant fused silica (Fig. 3-6), it is possible that this type of sample received some “special” treatments.

We tested more than 3 specimens from the same batch for each type of sample. For each type of fused silica, parameter A' is found to lie within $\pm 10\%$ of the values listed in Table 3-1, and c is found to lie within $\pm 5\%$ around 0.66 (sample B is not included).

3.5 Comparison to older compaction studies

Almost three decades ago, Primak and Kampwirth [11] reported comprehensive results of fused silica compaction for gamma ray, proton and electron sources. There, a 0.66 dose dependence was reported for all three types of radiation as seen in Fig. 3-8. Other authors have found similar results for electron beam radiation [12-14] and gamma ray radiation [15] using synthetic fused silica. The UV-induced compaction results reported here follow an almost identical dependence if one uses the total energy absorbed from two-photon absorption as the dose parameter instead of the total dose absorbed in the sample. For neutron and ion radiation, Primak [11] found a linear dependence of compaction on dose. Table 3-2 lists the extracted dose exponents c found when the previous compaction data was fit to a relation:

$$\frac{\Delta\rho}{\rho} = AD_{\alpha}^c \quad (3-4)$$

where D_{α} is the absorbed radiation dose.

TABLE 3-2 *

Dose Exponent for Compaction Formation from Previous Compaction Studies

Author	Radiation Source	Compaction Range $\frac{\Delta\rho}{\rho}$	Fused Silica	Dose Exponent c
Primak [11]	neutron, He ⁺ , D ⁺ gamma, e-beam H ⁺	10^{-6} - 10^{-3}	Suprasil 1	1
		10^{-6} - 10^{-3}	Suprasil 1	0.66
		10^{-6} - 10^{-3}	Suprasil 1	0.71
Higby [12]	e-beam	10^{-5} - 10^{-3}	Optosil	0.32, 0.37
			Suprasil 2	0.59
			Suprasil 300	0.56
			Suprasil W2	0.77
Friebele [16]	e-beam	10^{-5} - 10^{-3}	Suprasil 2	0.64
			Suprasil W2	0.67
			Optosil	0.3
Norris [17]	e-beam	10^{-4} - 10^{-3}	Infrasil	0.65
		10^{-4} - 10^{-3}	Corning 7940	0.65
		10^{-5} - 10^{-4}	Corning 7940	0.7
Rajaram [18]	e-beam	10^{-4} - 10^{-2}	Optosil	0.37
Merbacher [13]	e-beam	10^{-4} - 10^{-2}	Suprasil 2	0.5
Dellin [19]	e-beam	10^{-4} - 10^{-3}	T-08	0.5
Shelby [15]	gamma	10^{-5} - 10^{-3}	Suprasil W	0.81

* Copied from reference [9]

From Table 3-2, we see that in fused silica, the sublinear power dependence of compaction on dose holds over a wide range of compaction levels (10^{-6} - 10^{-2}) for gamma, e-beam and H⁺ radiation. In many cases, the dose exponent c lies very close to 0.66 and the data are generally centered around this value. (Optosil is exceptional; we do not understand the reason yet.) Only in the case of neutron and heavy ions does the dose parameter c equal 1.

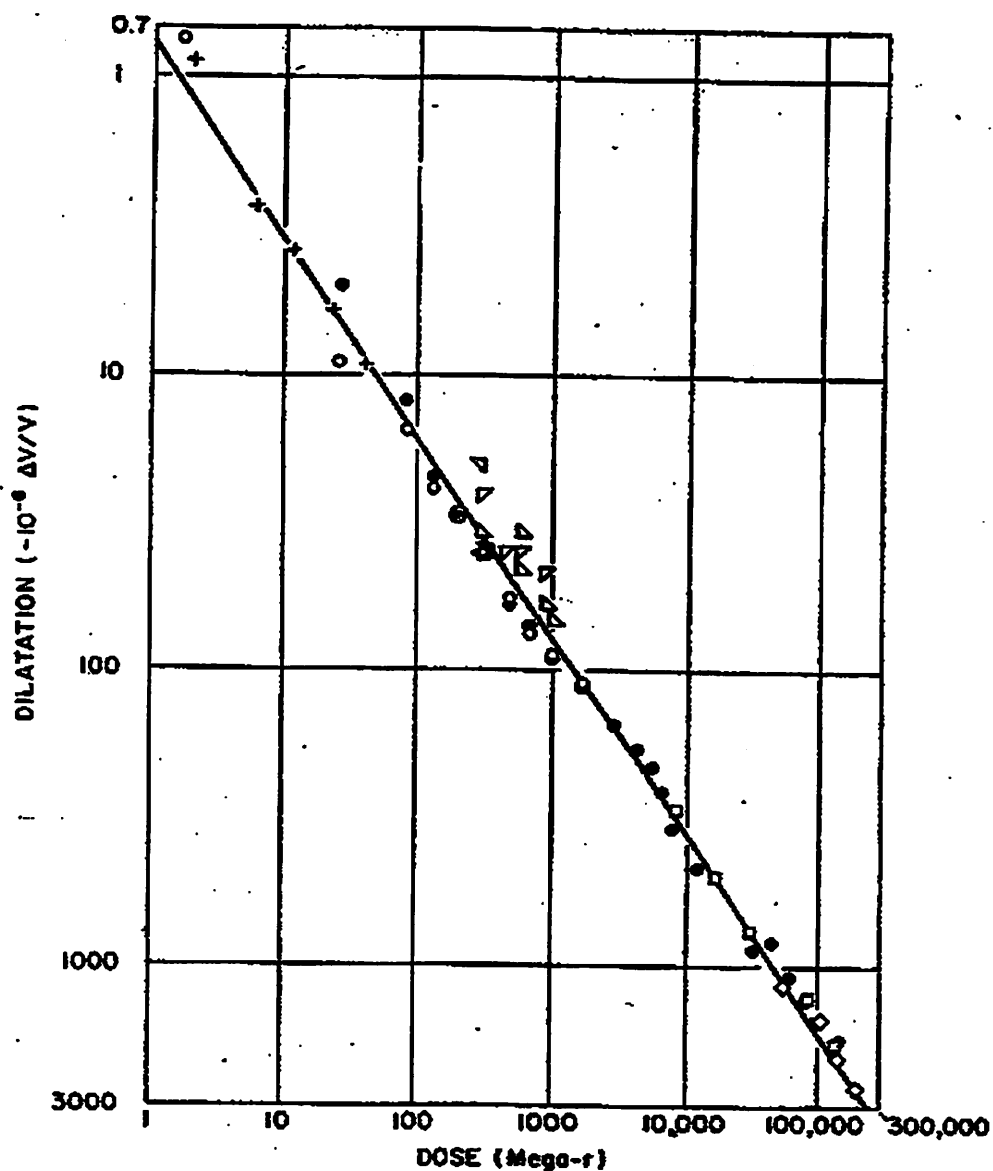


Figure 3-8. The dilation of Suprasil at the point of the maximum damage along the range of electrons plotted against the dose at this point; circle, actual measurements; round spot, calculated from the mean dilation; squares and diamonds, respective progressive 0.3 MeV irradiation of two specimens; crosses, respective single 0.6 MeV irradiations of five specimens. Triangles are comparative points for gamma irradiations of end-standards; the quadrants are for the respective temperature 7°, 25°, 50° and 95°C. The left half-diamonds is for 75°C. The line is drawn for a slope of 0.66 (2/3-power dependence). Copied from reference [11].

3.6 Conclusions:

Birefringence monitoring is capable of measuring the compaction induced birefringence distribution in very lightly compacted samples. The 193-nm compaction durability for different experimental fused silica samples was tested. A universal sublinear power relation between UV-induced compaction and absorbed UV dose was found, which is consistent with the previous compaction studies using electron-beam and gamma radiation. The dose exponent c in Eq. (3-4) depends on the type of radiation. For ionizing radiation such as UV, e-beam and gamma rays, c is close to 0.66, but for knock-on radiation, such as neutrons, c is 1.

3.7 References:

- [1] D.L.Griscom, "Nature of defects and defect generation in optical glasses", SPIE Vol. 541, 38 (1985)
- [2] P. Schermerhorn, "Excimer laser damage testing of optical materials". Proceedings of the SPIE – The International Society for Optical Engineering, vol.1835, 70 (1993)
- [3] R. Schenker, P. Schermerhorn, W. G. Oldham, "Deep-ultraviolet damage to fused silica". Journal of Vacuum Science & Technology B (Microelectronics and Nanometer Structures), vol.12, 3275 (1994)
- [4] R. E. Schenker, F. Piao, W. G. Oldham, "Material limitations to 193-nm lithographic system lifetimes". Proceedings of the SPIE - The International Society for Optical Engineering, vol.2726, 698 (1996)
- [5] K.Arai, H.Imai, H.Hosono, Y.Abe, H.Imagawa, "Two-photon processes in defect formation by excimer lasers in synthetic silica glass". Applied Physics Letters, vol.53, 1891 (1988)
- [6] T. E. Tsai, D. L. Griscom, E. J. Friebele, "Mechanism of intrinsic Si E'-center photogeneration of high-purity silica". Physical Review Letters, vol.61, 444 (1988)
- [7] R.K.Brimacombe, R.S.Taylor, K.E.Leopold, "Dependence of the nonlinear transmission properties of fused silica fibers on excimer wavelength", J. Appl. Phys. 66 (9), 4035 (1989)
- [8] Integral Square Method (ISQ), developed by R. Sandstrom at Cymer Inc.
- [9] Richard Schenker, Ph. D. Thesis, UC-Berkeley, 1997.
- [10] The fused silicas were manufactured by Corning Inc., Heraeus Inc., and Shin-Etsu Inc. and were provided by SEMATACH.
- [11] W.Primak, R.Kampwirth, "The radiation compaction of vitreous silica", J. Appl. Phys. Vol. 39, 5651 (1968)
- [12] P. L. Higby, E. J. Friebele, C. M. Shaw, M. Rajaram, E. K. Graham, D. L. Kinser, E. G. Wolff, "Radiation effects on the physical properties of low-expansion-coefficient glasses and ceramics". Journal of the American Ceramic Society, vol.71, 796 (1988)
- [13] C. I. Merzbacher, E. J. Friebele, J. A. Ruller, P. Matic, "Long-wavelength infrared transmitting glasses: new ternary sulfide compositions". Proceedings of the SPIE - The International Society for Optical Engineering, vol.2018, 222 (1991)
- [14] P.L.Higby, E.J.Friebele, Am. Ceram. Soc. Bull. 67, 615 (1988)

- [15] J.E.Shelby, "Radiation effects in hydrogen-impregnated vitreous silica", J. Appl. Phys., Vol. 50, 3702 (1979)
- [16] E.J.Friebele, P.L.Higby, "Radiation effects in amorphous SiO₂ for windows and mirror substrates", NIST Spec. Pub. 756 (1988)
- [17] C.B.Norris, E.P.EerNisse, "Ionization dilation effects in fused silica from 2 to 18-keV electron irradiation", J. Appl. Phys. Vol. 45, 3876 (1974)
- [18] M.Rajaram, T.Tsai, E.J.Friebele, "Radiation induced surface deformation in low-thermal-expansion glasses and glass ceramics", Adv. Ceram. Materials, Vol. 3, 598 (1988)
- [19] T.A.Dellin, D.A.Tichenor, E.H.Barsis, "Volume, index of refraction, and stress changes in electron irradiated vitreous silica", J. Appl. Phys. Vol. 48, 1131 (1977)

Chapter 4

Temperature Effects on the UV Compaction Rate and Thermal Annealing

Experiments

4.1 Introduction

The radiation-induced change in density has been interpreted in terms of the configuration changes of SiO_4 tetrahedrons in an open three-dimensional corner linked network [1]. Ionization is assumed to be the major source driving density change for electron, gamma and UV irradiation [1]. Primak *et al.* [1] found that the compaction rate of fused silica for electron, and gamma ray irradiation is independent of temperature from about 0°C to 100°C . Hence it is not a thermally activated process. But Rothschild *et al.* [2] found that the 193nm UV-induced compaction rate of fused silica increased dramatically with increasing temperature. Preliminary semi-quantitative studies in our laboratory confirmed the latter [3]. More recently, quantitative studies of the temperature dependence of compaction on a variety of samples (as measured using strain-induced birefringence) showed more normal behavior. The compaction decreased with increasing sample temperature. In this chapter, data for different 1995-1996 UV grade experimental fused silica samples (A, B, C, D, E, and F) are compared with respect to their resistance to UV-induced compaction at 193nm under elevated sample temperature conditions. We find that the compaction rate decreases with increasing sample temperature. Compaction recovery is observed at temperature as low as 120°C , suggesting that the recovery of UV-induced compaction in fused silica is a thermally excited process with low activation energy.

There are two most commonly employed types of annealing, isochronal and isothermal. We can use the experimental techniques to measure the fraction of radiation-induced density change remaining at several selected temperatures (isochronal) or to measure this change as a continuous function of time at a fixed temperature (isothermal). Here, both isothermal and isochronal annealing techniques are used to help us to investigate the mechanism of UV-induced compaction in fused silica.

4.2 Ambient temperature effects on compaction rates

In the temperature-dependent damage rate experiments, four sets of fused silica samples (A, C, D, and E) were tested at elevated temperatures. Fused silica samples were put in an electric oven which was thermally isolated from the outer environment. The temperature of the oven was controlled by means of a solid state relay (SSR) which turns off or on the heating circuit by the trigger signal of a temperature controller. The temperatures were measured by Chromel-Alumel thermocouples. Generally, the temperatures could be controlled within $\pm 3^\circ\text{C}$. Two holes on the opposite sides of the oven provide the beam paths for both the UV and testing He-Ne beams. For the latter we allowed the electric oven to cool down before measurement to reduce any error caused by the air convection. We irradiated sample E at room temperature (23°C) and 100°C , with the result shown in Fig. 4-1.

Fig. 4-1 shows that the compaction rate at 100°C is just about half of that at 23°C , inconsistent with the results in earlier literature. We also found that even at higher temperatures, the sub-linear dependence of the compaction on the dose was still obeyed.

The same test on sample C showed a similar result (Fig. 4-2). The compaction and the absorbed dose still followed the relation:

$$\frac{\Delta\rho}{\rho} = A' \left(\frac{NI^2}{\tau} \right)^c \quad (4-1)$$

where N is the number of pulses in millions, I is the pulse energy density in mJ/cm^2 , A' is a material dependent constant, and c is 0.66.

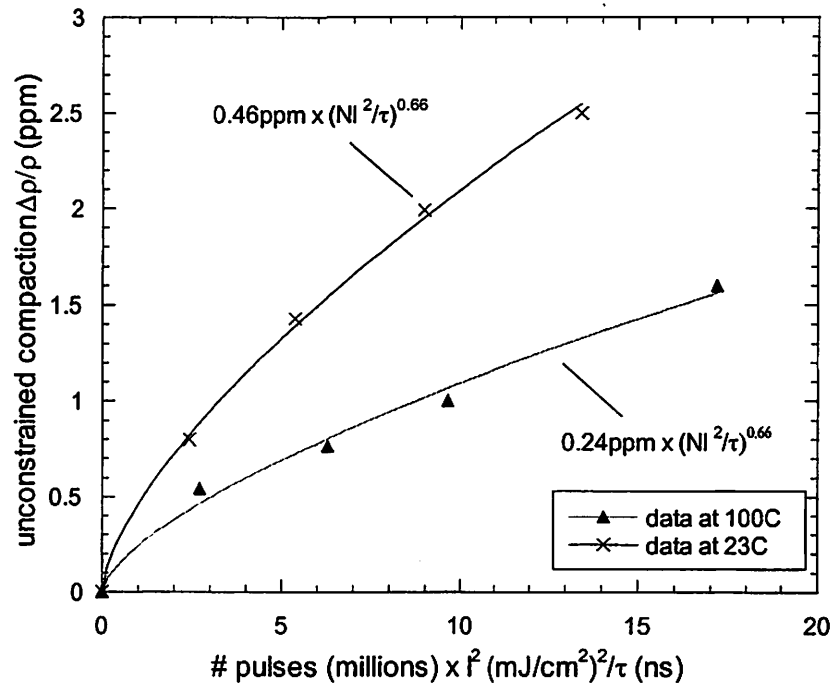


Figure 4-1. Temperature dependence of the damage rate for sample E

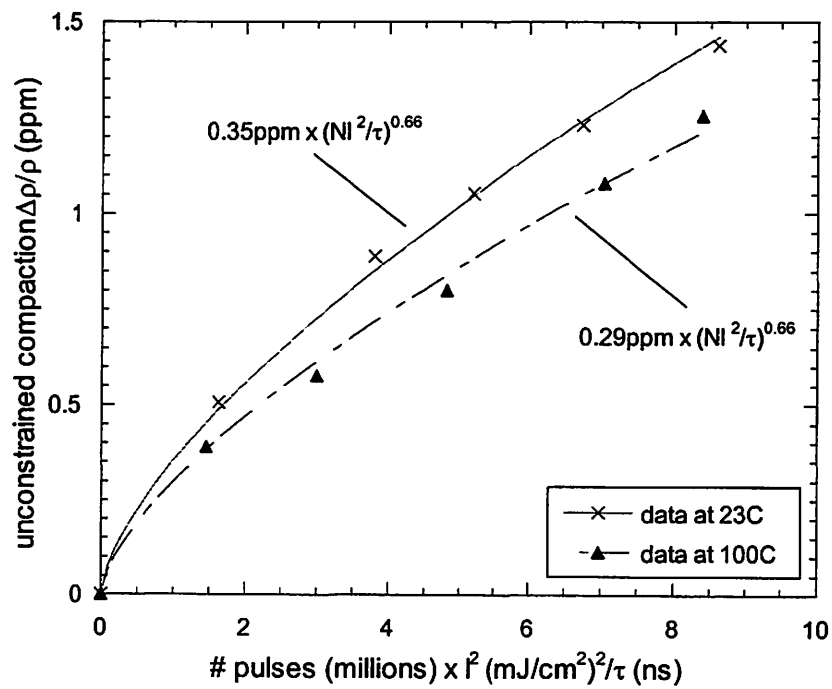


Figure 4-2. Temperature dependence of the damage rate for sample C

We also compared the UV-induced compaction levels at room temperature (23°C), 90°C and 120°C for sample A and D. The final measured compaction levels after being exposed in the 193nm UV beam for 2×10^6 rad* are listed in Table 4-1. For both samples A and D, tests performed at higher temperatures yield lower compaction levels. Thus all samples displayed decreasing damage rate with increasing temperature, although the temperature dependence for sample A is only very slight.

(* rad is the unit used to measure the absorbed radiation energy, $1 \text{ rad} = 0.01 \text{ J/kg}$. In our experiment, when $\frac{NI^2}{\tau} = 10.7$ (million pulses $\times (\text{mJ/cm}^2)^2/\text{ns}$), the absorbed UV dose is about 10^6 rad).

TABLE 4-1
Temperature Dependence of Damage Rate for Sample A and D

$\frac{\Delta\rho}{\rho}$ after 2×10^6 rad exposure	Sample A	Sample D
T = 23 °C	5.8 ± 0.2 (ppm)	2.4 ± 0.2 (ppm)
T = 90 °C	5.6 ± 0.2 (ppm)	1.87 ± 0.2 (ppm)
T = 120 °C	5.2 ± 0.2 (ppm)	1.80 ± 0.2 (ppm)

4.3 Isochronal annealing of compaction

In isochronal annealing experiments, five pieces of sample D from the same batch were radiated by 193nm UV at one spot on each sample to the same compaction level (such as 1ppm). After atmospheric annealing at different temperatures (from 100°C to 400°C) for 20 minutes, the specimens were withdrawn, air-quenched, and scanned in the He-Ne beam to check the remaining compaction. We also performed the isochronal annealing experiments on sample E, but because of the limited availability of specimens, we used only two physical samples from the same batch. UV exposure and annealing were performed on 5 different spots (two and three spots on each sample) sequentially. The annealing time was 15 minutes. During these tests, we monitored compaction and absorbed UV dose curve for all of these runs to make sure that there is no sample to sample variation.

The results of the annealing of the damaged fused silica samples are shown in Fig.

4-3. The relative relaxation of the compaction is defined as:

$$\text{Relative recovery} = \frac{\rho_i - \rho}{\rho_i - \rho_0} \quad (4-2)$$

where ρ_0 is the density of the as-received fused silica samples, ρ_i is the density of the UV-compacted sample, ρ is the density of the sample after thermal annealing. In Fig. 4-3, we plot the measured relative recovery for sample D and E after each annealing cycle. The recovery of the compaction even at very low temperature indicates that the activation energy associated with the recovery process is very low.

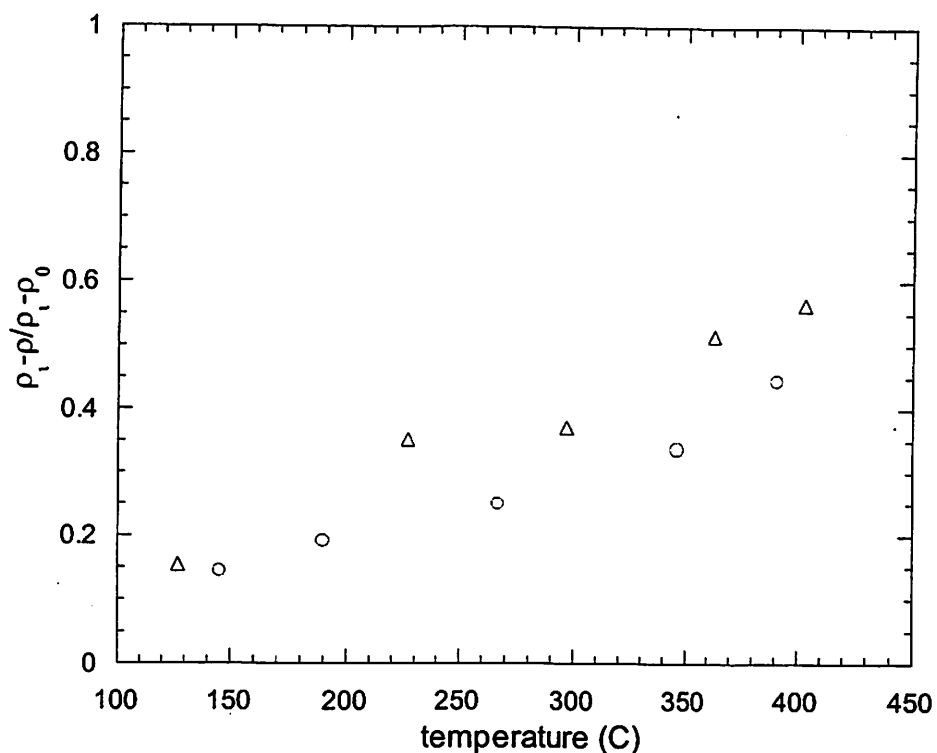


Figure 4-3. Relative recovery vs annealing temperature for sample D and E. (triangle points are for sample D and circle points are for sample E).

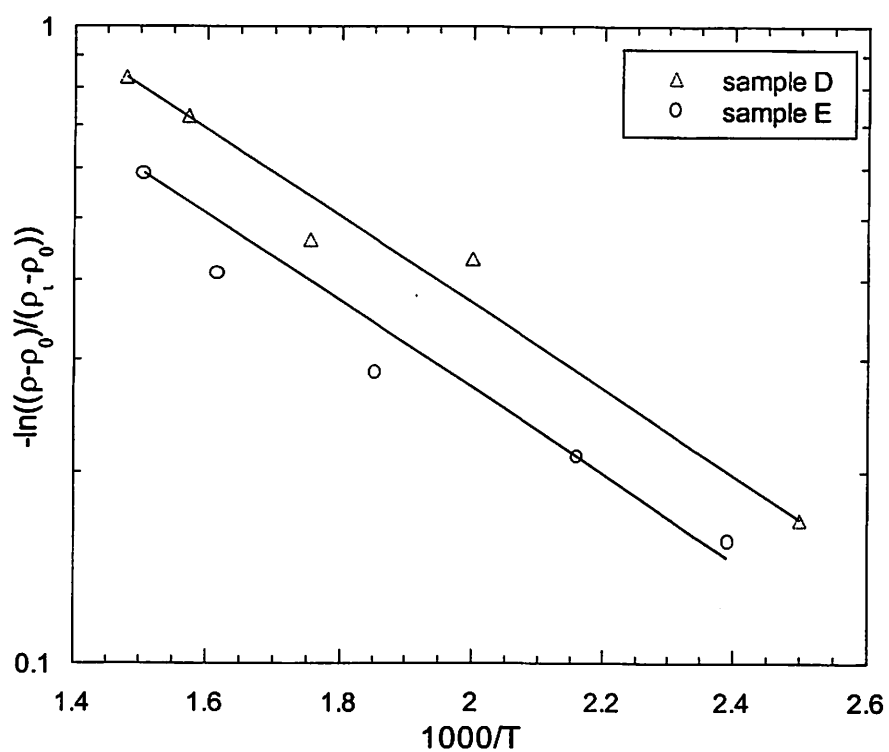


Figure 4-4. Isochronal annealing experiments for sample D and sample E, the activation energy for both samples is found to be 0.13eV (slope of the straight line in graph).

To analyze the data, we fit the data to the general rate equation

$$\frac{\rho(T, t) - \rho_0}{\rho_i - \rho_0} = \exp[-\nu(T)t] , \quad (4-3)$$

where t is annealing time [4]. For simplicity, a single dominant process is assumed with the rate constant $\nu(T)$ given by the Arrhenius expression

$$\nu(T) = \nu_0 \exp\left(-\frac{E}{\kappa_B T}\right), \quad (4-4)$$

where κ_B is Boltzmann constant, E is the activation energy and ν_0 is a constant. We can rewrite Eq. (4-3) and (4-4) as

$$-\ln \frac{\rho(T, t) - \rho_0}{\rho_i - \rho_0} = (\nu_0 t) \exp\left(-\frac{E}{\kappa_B T}\right). \quad (4-5)$$

The annealing time t is fixed in our experiments and we plot our data in the form of Eq. (4-5). The slope of the curve in Arrhenius plot is the apparent activation energy for the recovery process, as shown in Fig. 4-4. The apparent activation energy for both samples is around 0.13eV. We must be cautious in using the number because of the unverified assumptions in interpreting the data. In particular we do not believe there is any reason to believe that a single process is dominant.

In the above experiments, we used different experimental conditions (different annealing times) for samples D and E to ensure the reliability of the activation energy result. The difference in the compaction recovery levels in Fig. 4-3 is consistent with the different annealing times used for the two samples.

4.4 Isothermal annealing of compaction

In Fig. 4-5(a) and 4-5(b), we plot the isothermal annealing density data for two sets of samples A and B. For each type, we used three identical specimens. They were first densified by 193nm UV beams, then were isothermally annealed at different temperatures from 100°C to 600°C. After the thermal annealing process, the residual stress fields were measured and converted to compaction level. For simplicity of representation, we plot normalized residual compaction $\mathcal{R} = (\rho - \rho_0) / (\rho_i - \rho_0)$ versus annealing time. One observes immediately that the annealing is monotonic in all cases. For all of the annealing temperatures, most of the relaxation happens in the first 30-40 minutes and then the relaxation saturates. This behavior is very similar to the observation in pressure compressed fused silica samples (Fig. 4-6) [5]. In our experiments, a higher annealing temperature induces higher levels of compaction recovery (saturation), but the saturation level is sample-type dependent. For example, at 600°C, the residual compaction for sample A saturates at about 50%, but for sample B, even at 500°C, the residual compaction saturates at a lower level of about 30%.

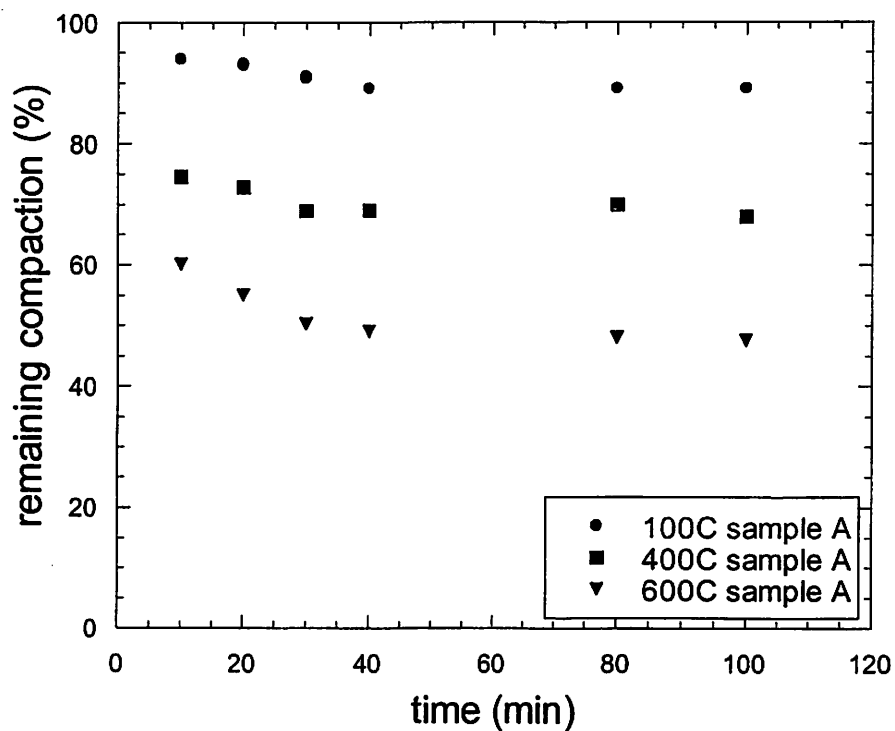


Figure 4-5(a). Isothermal annealing data for sample A at three different temperatures.

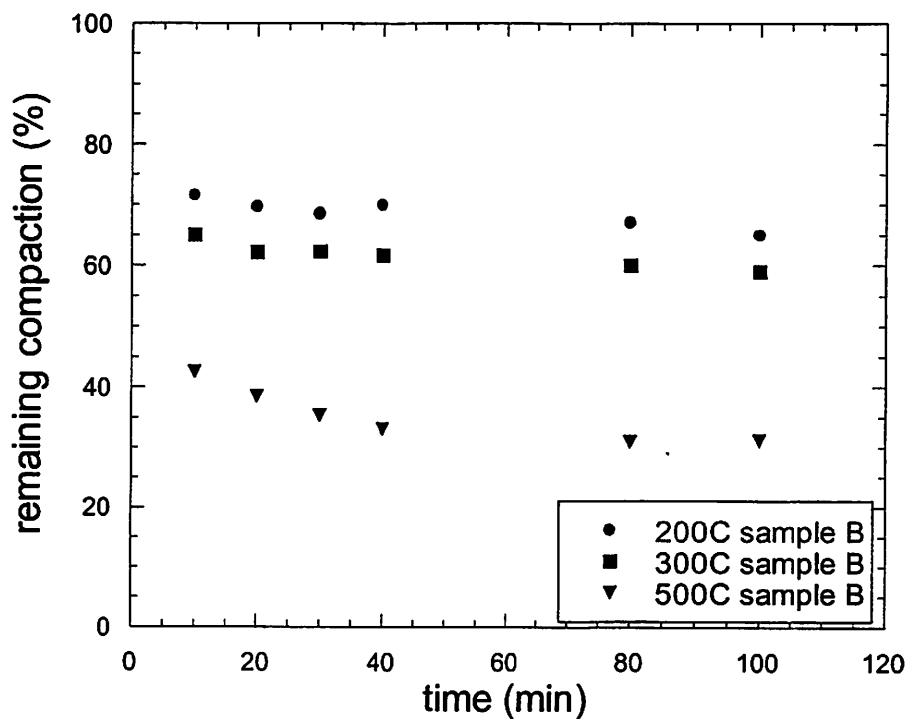


Figure 4-5(b). Isothermal annealing data for sample B at three different temperatures.

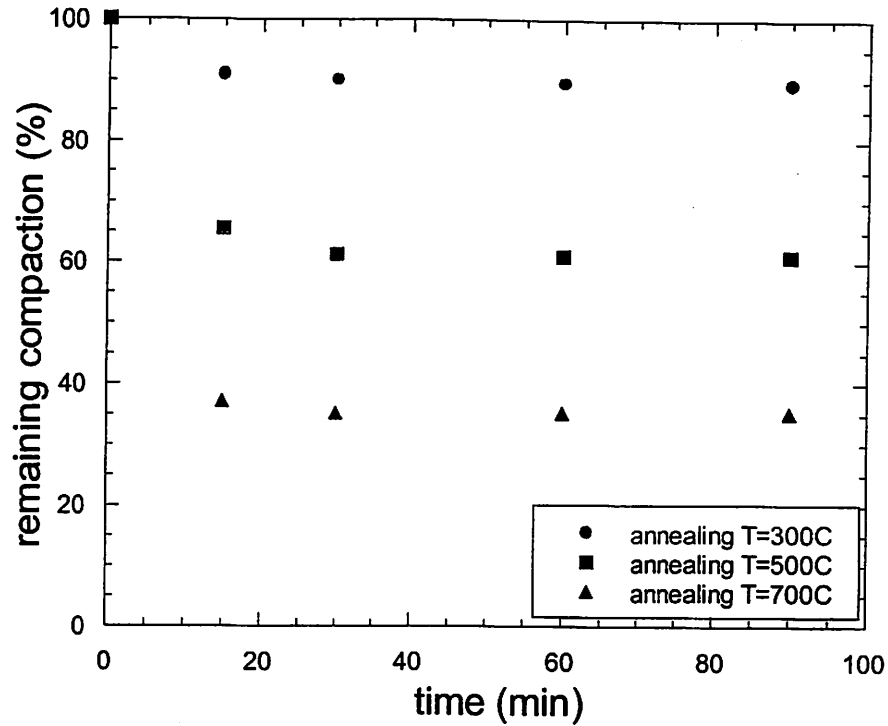


Figure 4-6. Isothermal annealing data for pressure compacted fused silica. (Taken from J.D.Mackenzie, J. Am. Ceram. Soc., 46, 470 (1963))

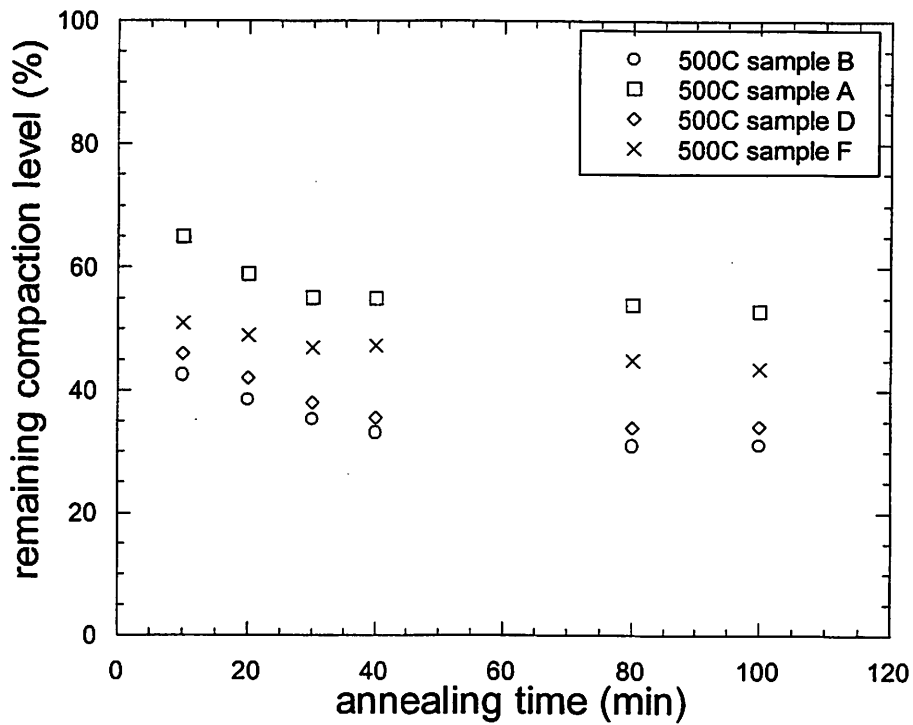


Figure 4-7. Isothermal annealing data for sample A, B, D, and F at 500°C.

We note that compaction rate for the type A sample is higher than that of the type B sample, suggesting a possible correlation between saturation of compaction recovery and compaction rates. To test this correlation, we performed isothermal-annealing experiments at 500°C for sample A, B, D and F. The samples were initially densified to 1.1, 1.5, 2.0, and 1.2 ppm respectively. The results from this isothermal annealing processes are plotted in Fig. 4-7. We noticed that, after the compaction recovery saturates, the saturated residual compaction \mathfrak{R}_s for these four samples are in the order of $\mathfrak{R}_s(B) < \mathfrak{R}_s(D) < \mathfrak{R}_s(F) < \mathfrak{R}_s(A)$. From Fig. 3-6, we see that the compaction rates for these four samples are in the order of $D(B) < D(D) < D(F) < D(A)$, thus the compaction rates correlate with the residual compaction after annealing.

4.5 Compaction recovery or plastic flow?

As already noted, in our experiments, the relative density change $((\rho_i - \rho_0)/\rho_0)$ was not measured directly, but inferred from stress induced birefringence. The experimental results for the thermal annealing assume that the decreased birefringence signals are owing to the recovery of compaction. But if we examine the geometry of the UV-damaged spot (Fig. 2-1), we note that plastic flow could also decrease the birefringence signals at high temperature: as T increases; materials in region I and III could flow towards region II under influence of the stress field in region II, much like birefringence annealing in conventional glass production. Of course, the temperature dependence of viscosity in normal fused silica is well-characterized [6], and significant flow at 600°C and below is actually unexpected.

To buttress the damage-recovery interpretation, we performed the following 5-step experiment (Fig. 4-8): (1) We tested the absorbed UV dose and compaction curve for virgin sample. (2) The same whole sample was uniformly irradiated in the 193-nm UV beam (uniformly compacted). (3) A new spot was irradiated to obtain the compaction and absorbed UV dose curve for the uniformly compacted sample. (4) This sample was then annealed at high temperatures. (5) The annealed sample was tested again for compaction. The results are plotted in Fig. 4-9(a), 4-9(b) and 4-9(c) for samples B, D and F.

For each of Fig. 4-9(a), (b), (c), we observe the following: (i) The compaction rate for all of the uniformly pre-compacted samples is lower than that of virgin samples by a predicted amount as expected from the “universal” sub-linear compaction rate curves. (ii) After thermal annealing of the uniformly compacted samples, the UV damage rates increased towards the virgin sample values. We also note that after the step (2), a He-Ne beam scan was used to check the uniformity of UV-induced compaction throughout the tested samples. The uniformity across the finished samples was found to be comparable with that of as-received samples. A uniform irradiation produces no stress fields. Therefore the damage rate recovery observed in Fig. 4-9(a)-(c) could not represent a simple plastic-flow relaxation process in response to damage-induced stress. This observation supports an interpretation of our thermal annealing experiments in which the decreasing stress field around the compacted regions at high temperature is from the density recovery of compacted area and not from the plastic flow driven by the stress.

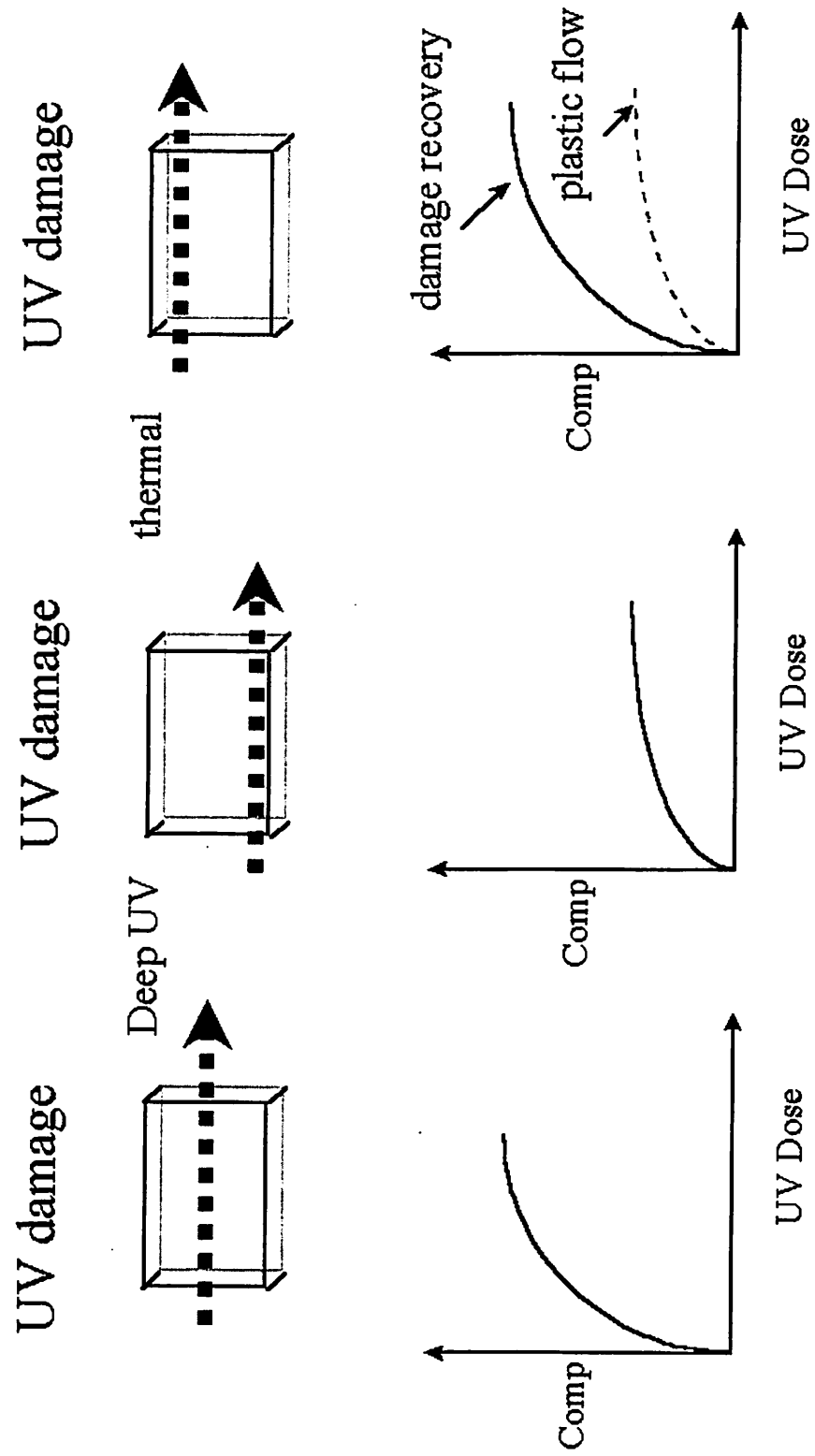


Figure 4-8. Schematic drawing of experimental flow for verification of thermal recovery of UV-induced densification in fused silica

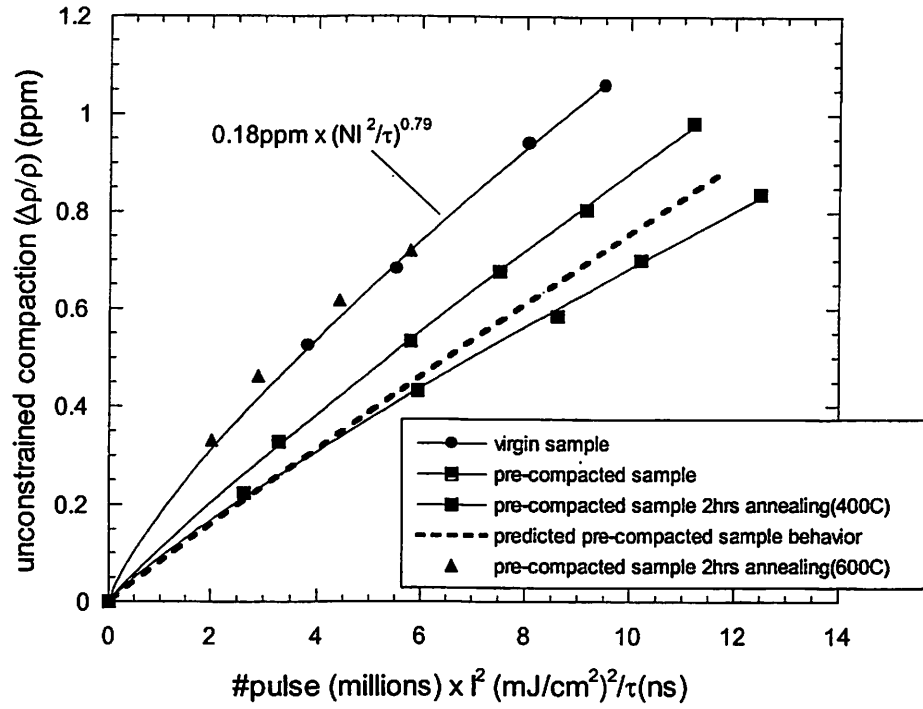


Figure 4-9(a). UV compaction behaviors for uniformly compacted sample B, before and after thermal annealing process

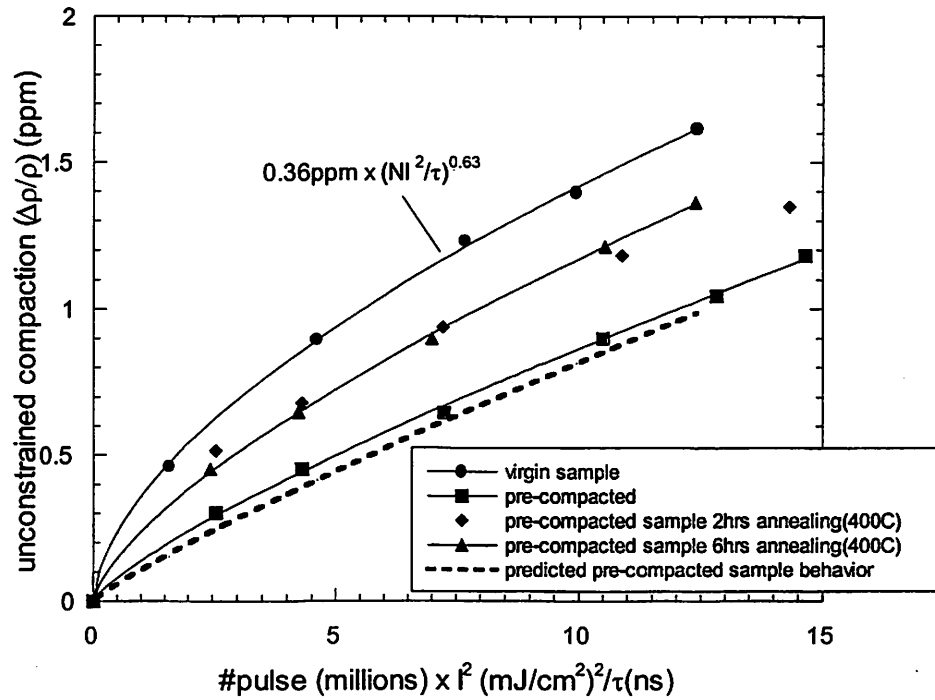


Figure 4-9(b). UV compaction behaviors for uniformly compacted sample D, before and after thermal annealing process

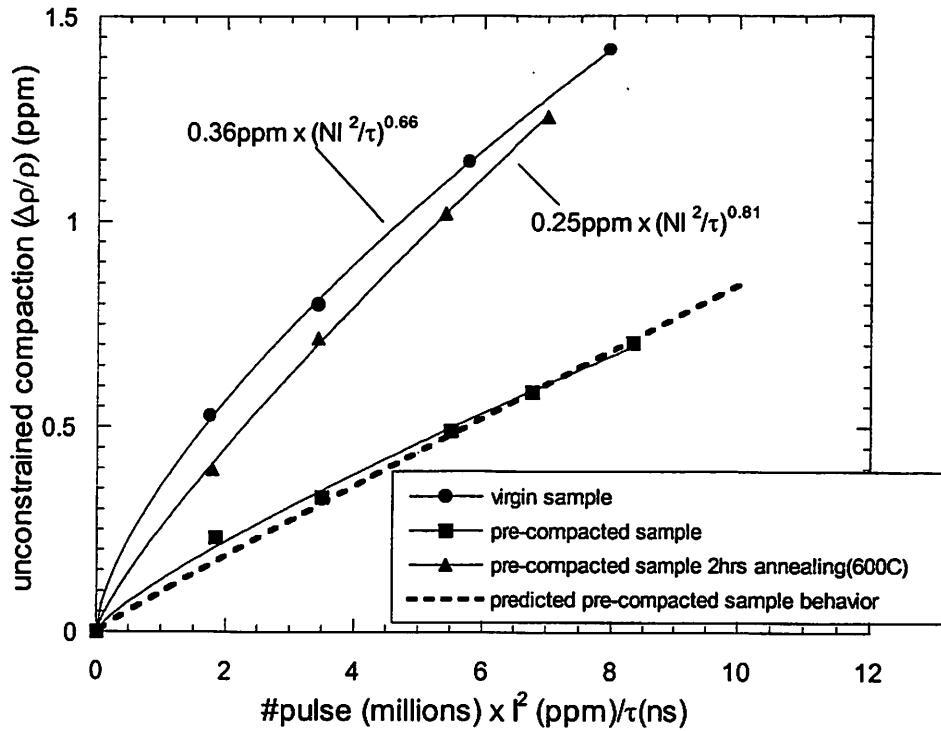
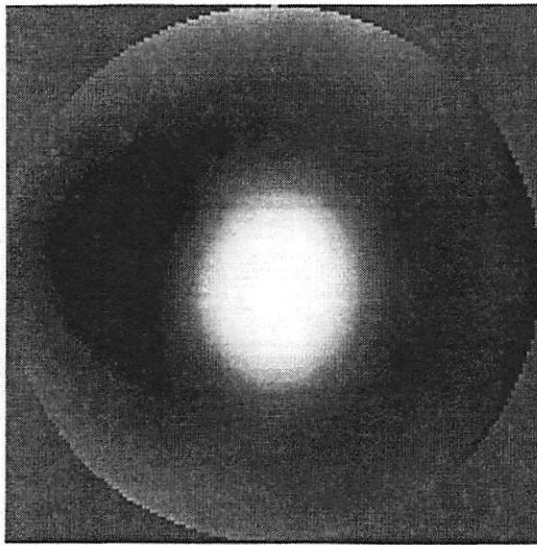


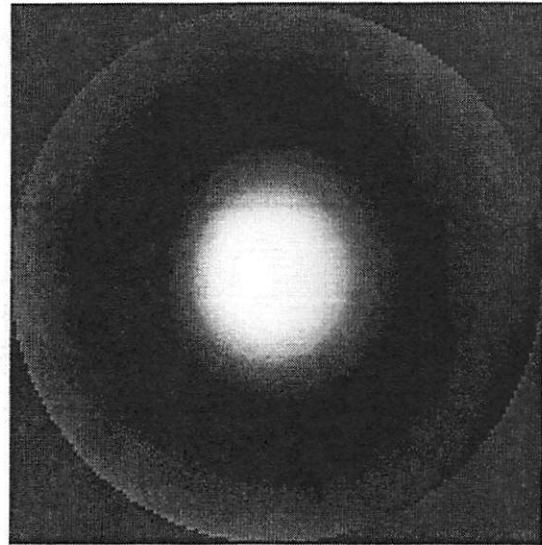
Figure 4-9(c). UV compaction behaviors for uniformly compacted sample F, before and after thermal annealing process

We have further confirmed this conclusion by interferometric measurement (PS/PDI at 193nm wavelength --- see Chapter 2) of the optical path difference (OPD) through damaged versus undamaged regions in fused silica samples before and after thermal annealing. The OPD which is directly related to the density, anneals in parallel with the birefringence. As an example, two pieces of the type B sample (I and II) were compacted to 1.4 and 1.2ppm respectively, the wavefronts were measured by 193nm phase-shifting point diffraction interferometry (PS/PDI) [7], and the results are displayed in Fig. 4-10(a) and 4-10(b). Then the sample (I) was annealed at 200°C for 35 minutes and sample (II) was annealed at 600 °C for one hour. After annealing, we re-measured the wavefront at the damaged spots for these two samples, as shown in Fig. 4-11(a) and 4-

11(b). To analyze the thermal recovery of the compaction, we plotted the cross sections of the wavefront for these two samples before and after thermal annealing in Fig. 4-12. There was approximately 28% compaction recovery observed for sample (I), and almost 100% compaction recovery observed for sample (II). These observations agreed with our birefringence measurement and our earlier thermal annealing results for type B samples [Fig. 4-5(b) and Fig. 4-9(a)].

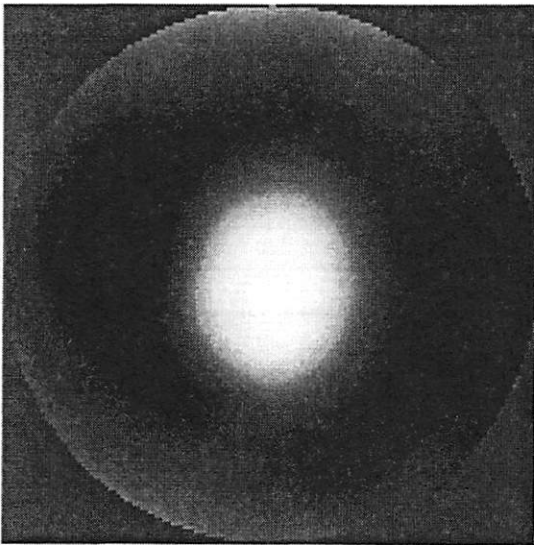


(a)

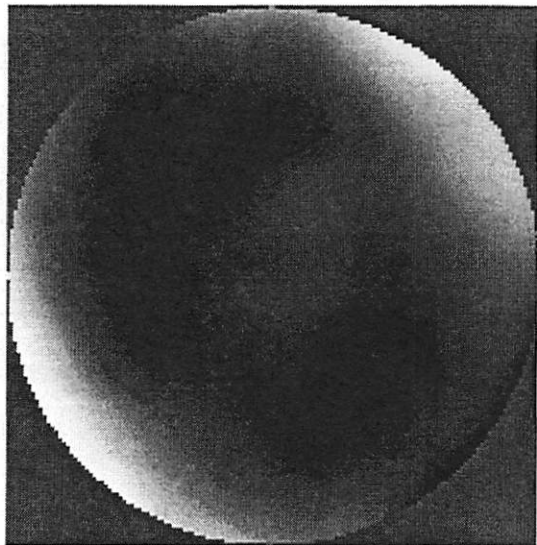


(b)

Figure 4-10. The measured wavefront at damaged spots from (a) sample I and (b) sample II (intrinsic OPD has been subtracted)

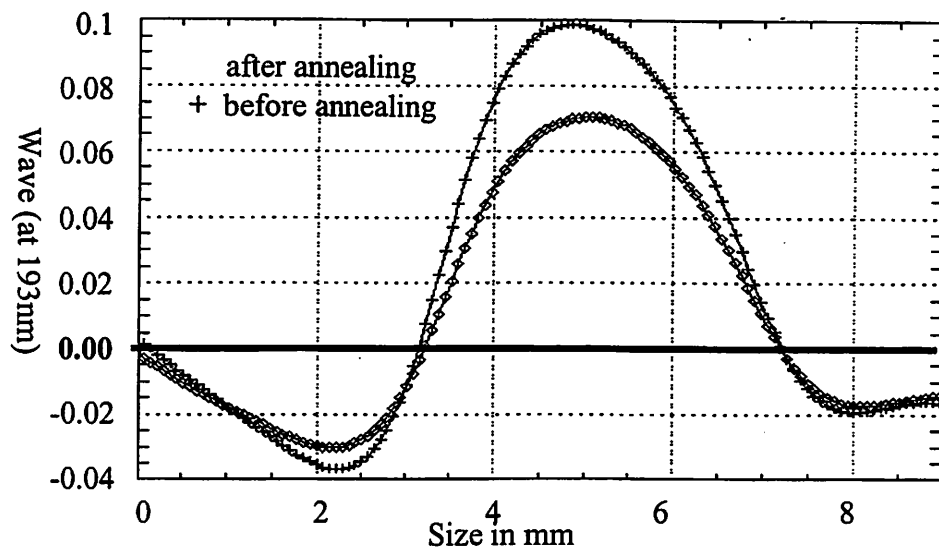


(a)

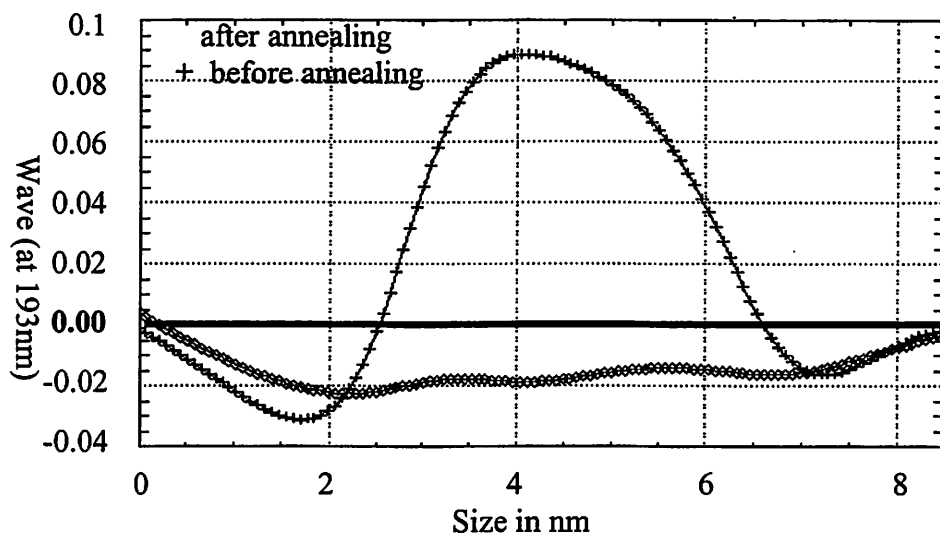


(b)

Figure 4-11. (a) The resulting difference wavefront, subtracting the wavefront of the virgin sample from the wavefront of the thermally annealed *sample A*, annealed at 200°C for 35 minutes at the atmospheric pressure. (b) The resulting difference wavefront, subtracting the wavefront of the virgin sample from the wavefront of the thermally annealed *sample B*, annealed at 600°C for 60 minutes at the atmospheric pressure



(a)



(b)

Figure 4-12. Cross sections of the difference wavefronts relative to the virgin wavefronts, before and after thermal annealing. (a) Sample I shows approximately 28% recovery in peak OPD, and (b) sample II shows almost full recovery

In Fig. 4-9(b), after 2 hours 400°C thermal annealing, the UV compaction rate for the pre-UV-compacted sample D recovered towards that for the virgin sample. The same sample showed no further increase in the compaction rate after additional 4 hours 400°C annealing. This behavior is consistent with the saturation of compaction recovery in isothermal annealing [Fig. 4-5(a), 4-5(b)]. For the pre-UV-compacted sample B, in Fig. 4-9(a), after 2 hours 400°C thermal annealing, its compaction rate increases. Then the same sample was heated at 600°C for 2 hours. After this process, the UV compaction rate of the sample increases further and almost recovers back to the damage rate for the virgin sample B. This observation is consistent with the results from our interferometric measurement for sample B we just mentioned. An annealing temperature of 600 °C is high enough to completely eliminate the UV-induced compaction in type B samples. This is also consistent with the results from the isothermal annealing experiment: a higher annealing temperature induces higher compaction recovery (saturation). But for pre-UV-compacted sample F [Fig. 4-9(c)], even though the compaction rate recovers after 2 hours 600°C annealing, it does not go back to the value for virgin sample F.

4.6 Pre-annealing of virgin samples

In another experiment, virgin samples of types A, B, D and F were annealed at 950°C for one hour prior to any radiation damage. The UV compaction behavior of these samples was then tested and plotted in Fig. 4-13(a) and 4-13(b). For sample B and D, the compaction rates after this 950°C pre-annealing process are higher than those in virgin samples. Moreover, for these two types of samples, even though their compaction rates are different, after the 950°C, one hour annealing cycle, the compaction rates for these

two types are very close to each other, and are still lower than those of virgin type A and F samples (see Fig. 3-6). In contrast to types B and D samples, one hour 950°C pre-annealing of types A and F samples does not change their UV compaction rates at all [Fig. 4-13(b)].

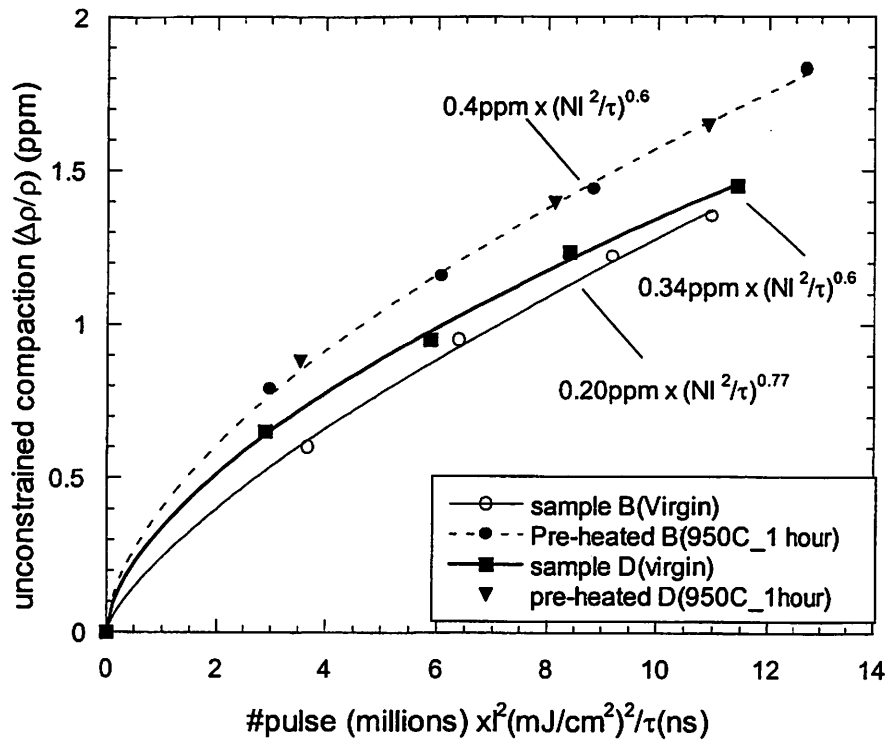


Figure 4-13(a). UV compaction behavior for virgin and 950°C pre-annealed sample B and D.

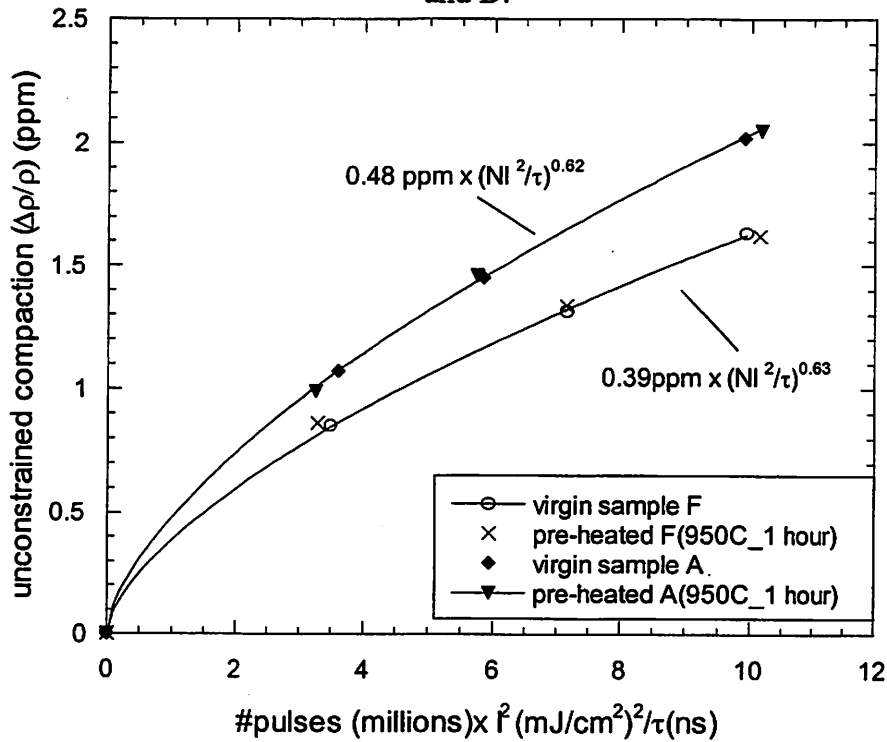


Figure 4-13(b). UV compaction behavior for virgin and 950°C pre-annealed sample A and F.

4.7 Summary

In this chapter, we described the thermal annealing behavior of UV-induced compaction in fused silica. We found that compaction recovery is observable at temperatures as low as 120°C. Isochronal annealing experiments determined that the apparent activation energy of this compaction recovery process is as low as 0.13eV. Thermal annealing of the uniformly compacted samples showed the recovery of the compaction rate proved that the thermal annealing of compaction is not driven by stress-induced plastic flow. We further confirmed this conclusion by interferometric measurement (at 193nm wavelength) of the optical-path-length difference (OPD) through damaged versus undamaged regions in fused silica samples before and after thermal annealing.

In isothermal annealing of UV-induced compaction, saturation of the compaction recovery was observed, consistent with the earlier observation of the saturation of the thermal recovery of pressure-compressed fused silica. A strong correlation between the compaction rate and thermal history among our tested fused silica samples was found. In Chapter 6, we describe a compaction model, which attempts to explain all of these phenomena.

4.8 References:

- [1] W.Primak, R.Kampwirth, "Radiation Compaction of Vitreous Silica", J. Appl. Phys. 39, 5651 (1968)
- [2] M.Rothschild, D.J. Ehrlich, and D.C. Shaver, "Effects of excimer laser irradiation on the transmission, index of refraction, and density of ultraviolet grade fused silica". Applied Physics Letters, vol.55, 1276-1278 (1989)
- [3] R.Schenker, Ph.D. Dissertation, UC-Berkeley (1997)
- [4] E.J.Friebele, D.L.Griscom, "Radiation Effects in Glass" in TREATISE ON MATERIALS SCIENCE AND TECHNOLOGY, Vol 17, 257-346 (1979)
- [5] J.D.Mackenzie, J. Am. Ceram. Soc. 46, P.470 (1963)
- [6] G.Hetherington, K.H.Jack, J.C.Kennedy, Phys. Chem. Glasses, 5 (5) 130 (1964)
- [7] S.H.Lee, F Piao, P.Naulleau, K.A.Goldberg, W.G.Oldham, J.Bokor, to be published

Chapter 5

Mechanisms in Radiation-Induced Compaction of Fused Silica

5.1 Introduction

The exposure of vitreous silica to radiation can cause changes in density [1-19]. The detailed origin of this density change has never been quite clear, but the compaction effect has been so universally observed in vitreous silica that it appears to be an inherent property of the material. In general, the dose dependence of compaction in vitreous silica obeys a power law

$$\frac{\Delta\rho}{\rho} = A' D_a^c. \quad (5-1)$$

The exponent c is found to be dependent on the nature of the radiation source and the effect of radiation on silica. For example, c equals to 1 for high-energy knock-on radiation [1] (neutron, He^+ , or D^+ etc.) and c is about 0.66 (2/3) for ionizing radiation (γ -ray [1-6], e-beam [1,2,7-12] and ultraviolet (UV) radiation [13-19]).

According to X-ray diffraction [20] and neutron-diffraction [21] investigations of vitreous silica structure after particle bombardment or hydrostatic pressure compression, the elementary SiO_4 tetrahedron unit maintains its shape. Only the angles of Si-O-Si bridging bond undergo essential changes. These angles define the tightness of the structural package on the whole and also are the randomizing factor in vitreous silica. The bridging bond angle in vitreous silica is the coordinate to indicate the structural change. Diffraction, infrared (IR) or Raman spectroscopy has been used to measure the bridging bond angle change in vitreous silica induced by particle bombardment or hydrostatic pressure [22,23].

In this chapter and the next chapter, the experimental results of radiation induced compaction are reviewed, and a two-phase structural model is proposed to explain the different c values in Eq. (5-1) for knock-on (atomic displacement) and ionizing radiation induced compaction in vitreous silica.

5.2 Structural change induced by radiation and hydrostatic pressure

The macroscopic effects of fast neutron irradiation in vitreous silica are well established [24-26]. At doses in excess of $\sim 2 \times 10^{20}$ fast neutrons cm^{-2} it approaches a final amorphous state which has a density between 2 and 3% higher than that of normal vitreous silica (Fig. 5-1).

Neutron diffraction and magnetic angle spinning (MAS)-NMR measurements have been performed on vitreous silica before and after irradiation to a dose of 2.8×10^{20} fast neutrons cm^{-2} (saturation range) [27]. There is a corresponding small increase in the Si-O bond length which is consistent with a reduction in the mean Si-O-Si bond angle of $\sim 9.5^\circ$ as indicated by the MAS-NMR data. Infrared (IR) and Raman spectroscopic measurements on ion and neutron radiated vitreous SiO_2 at saturation dose range also indicate that the mean bridging bond angle decreases by $\sim 10^\circ$ with respect to the unirradiated vitreous silica (about 145°) [22,28].

It is interesting to note that crystalline quartz, on the other hand, shows a decrease in density upon fast neutron irradiation. [24-26] At doses in excess of $\sim 2 \times 10^{20}$ fast neutrons cm^{-2} the structure approaches a final amorphous state which has the same final density as that of neutron irradiated vitreous silica and appears to be independent of the starting polymorph. The crystal loses its birefringence, [29,30] the refractive index decreases and the density decreases as much as 14.7 percent [30-32]. The optical

absorption edge at 8.5eV is shifted to 8.1eV, the value for silica [33]. The lattice expansion is clearly observed by X-ray diffraction methods [31], the diffraction lines become diffuse, resembling the diffraction pattern of glass. At the same time the Raman lines of quartz which are defined peaks in un-irradiated material widen, grow diffuse and become very similar to those in fused silica. [34]

The fact that, after heavy neutron irradiation or ion irradiation, all forms of SiO_2 are transformed to optically isotropic, glass-like material with virtually identical density, thermal expansion [35], elastic properties [36] leads to the conclusion that neutron or ion radiation produces a new phase of SiO_2 which is independent of the original phase before radiation. This new phase has the characteristic that the Si-O-Si bridging bond angle is about 10° smaller than that in normal vitreous silica and this state is normally called metamict phase [37].

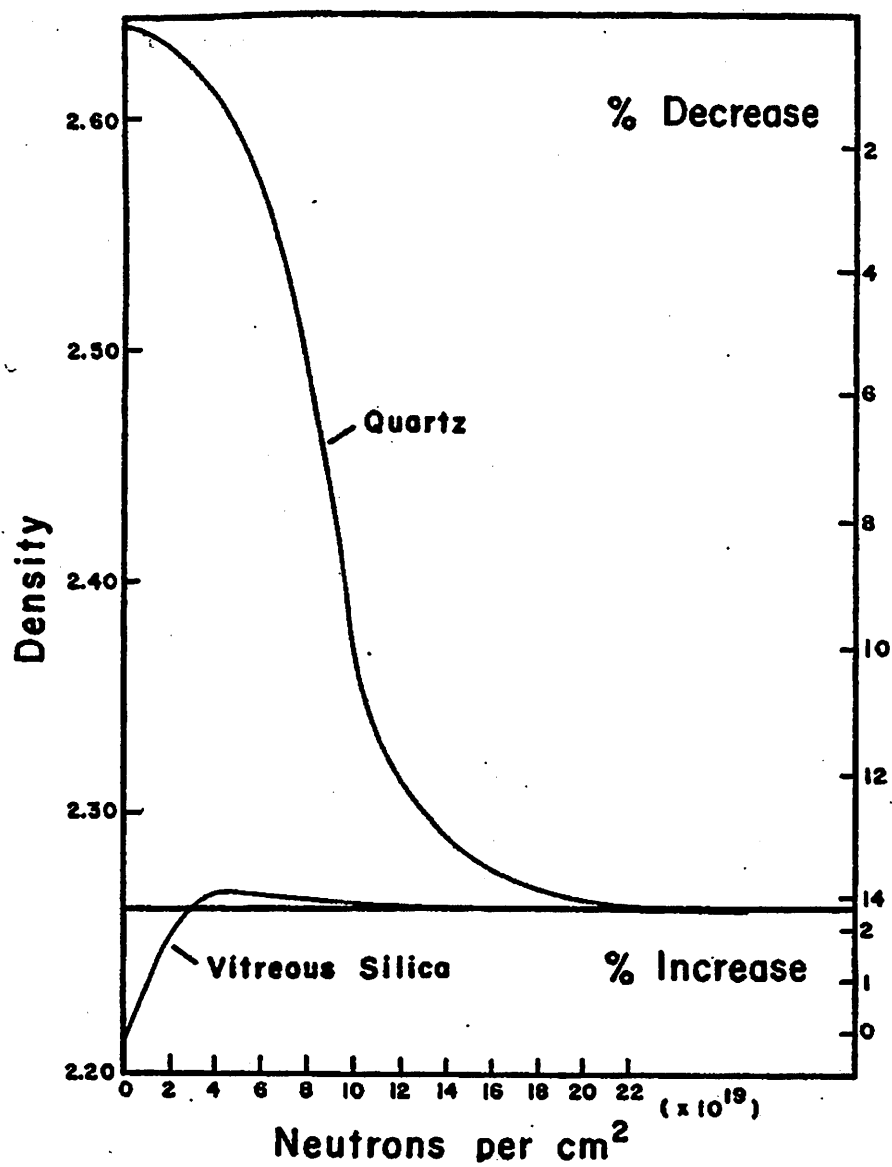


Figure 5-1. Change in density with neutron irradiation of crystalline quartz and vitreous silica. Copied from reference [37].

It is informative to compare the neutron or ion-induced compaction to hydrostatic pressure induced compaction in vitreous silica. Even though pressure can cause a much larger increase in density (>20%).

McMillan studied the Raman spectrum of hydrostatic-pressure-compressed vitreous silica [38]. When the hydrostatic pressure is about 9GPa at room temperature, 8% densification was observed, but the only change in the spectrum was a minor narrowing and slight upward frequency shift of the dominant 430cm^{-1} band on densification and there were no observable changes in D1 (495cm^{-1}) and D2 (606cm^{-1}) bands which were assigned by Galeener *et al.* [39] to the signatures of four-fold ring and three-fold ring structure in the silica network respectively, consistent with a slight decrease in the mean Si-O-Si angle. This can be explained by assuming densification at low temperature was achieved via cooperative rotations of adjacent SiO_4 tetrahedrons about Si-O-Si links with no change in the network connectivity [40]. There is no bond breaking and this densification process is called 'reversible' densification [41], which could be associated with the observed low activation energy (1-10kcal/mol) for the compaction recovery process [42-44].

Hemley *et al.* [40] also performed a similar experiment measuring the 430cm^{-1} band *in-situ* at high hydrostatic pressure up to 27.3GPa at room temperature. They found that up to 8GPa, there was a continuous narrowing and shift to higher frequency of the 430cm^{-1} band and these effects on the Raman spectrum were reversible up to 8GPa, consistent with what was reported on the quenched sample [38]. This suggested that no bond breaking happened. But when the pressure goes above 9GPa, the spectrum shift is no longer reversible. This effect was observed by McMillan *et al.* at a higher temperature

[38]. When they used 3.95GPa at 530 °C, the volume changed just 5.8%, but they found that the 430cm^{-1} band irreversibly shifted to 470cm^{-1} and the band became much narrower. The D2 (606cm^{-1}) band showed an increase in relative intensity indicating a decreasing average Si-O-Si bridging bond angle. The changes in 1060 and 1200cm^{-1} bands were also consistent with the Si-O-Si angles becoming smaller. The system apparently had different network connectivity.

In general, at room temperature and at pressure in excess of $\sim 9\text{GPa}$, irreversible densification takes place in fused silica accompanied by permanent changes in other physical properties [42]. Experimental evidence suggests that bond breaking occurs, which involves a decrease in the Si-O-Si bridging bond angle [23,40,45]. A “reconstructive” transformation resulting in a substantially different structure in permanently densified fused silica has been verified by Brillouin scattering measurements [46]. Direct measurement of infrared (IR) and Raman peaks in pressure-compacted vitreous silica indicated that the Si-O-Si bridging bond angle decreases about 10° when “irreversible” structural change occurs, and the Si-O bond length increases slightly [41].

Hydrostatic pressure can compact silica more than 20% while compaction induced by particle bombardment saturates at a density increase of just 2-3%. The microscopic effects are very similar in the two cases in that the average Si-O-Si bridging bond angle decreases by about 10° . This means that the structures of hydrostatic pressure compressed vitreous silica and neutron irradiated vitreous silica share similar short and intermediate range order. Because particle radiation produces smaller compaction, the irradiated vitreous silica should have more open space compared with hydrostatic

pressure compressed silica. The observation that the chemical etching rate in particle irradiated silica is enhanced by a factor of five supports this speculation [22].

5.3 Two-phase model for vitreous silica

We postulate the following structural model for vitreous silica; there are two phases existing for the amorphous SiO_2 tetrahedron network structure, a “low” temperature phase *A* with the most probable bridging bond angle at about 145° and a “high” temperature phase *B* with the most probable bridging bond angle at about 135° . The difference in the most probable bridging bond angle reflects the different structures for the two phases----especially the intermediate range order and its extension into longer range----long range order.

The equilibrium phase diagram for amorphous SiO_2 is governed by the thermodynamic potential known as the Gibbs free energy, as in Fig. 5-2(a) and 5-2(b),

$$G = E - TS + PV . \quad (5-2)$$

Where *S* is the entropy and *V* is the volume of the system.

We choose the most probable Si-O-Si bridging bond angle β_A (or β_B) as the coordinate to describe the system, *G* is a function of temperature *T* and pressure *P*. When the system is in a low temperature environment, the phase *A* has the lowest free energy, as shown in Fig. 5-2(a), the phase *A* is characterized by the most probable Si-O-Si angle at 145° in the network. When the temperature increases, the free energy curves for phase *A* and *B* are shifted. When the temperature passes the phase transformation temperature ($T_i \gg T_g$), the free energy for phase *B* is lower than that of phase *A*, as shown

in Fig. 5-2(b). In this case, the thermodynamically stable state is the phase *B* structure, which is characterized by the most probable Si-O-Si angle at 135° .

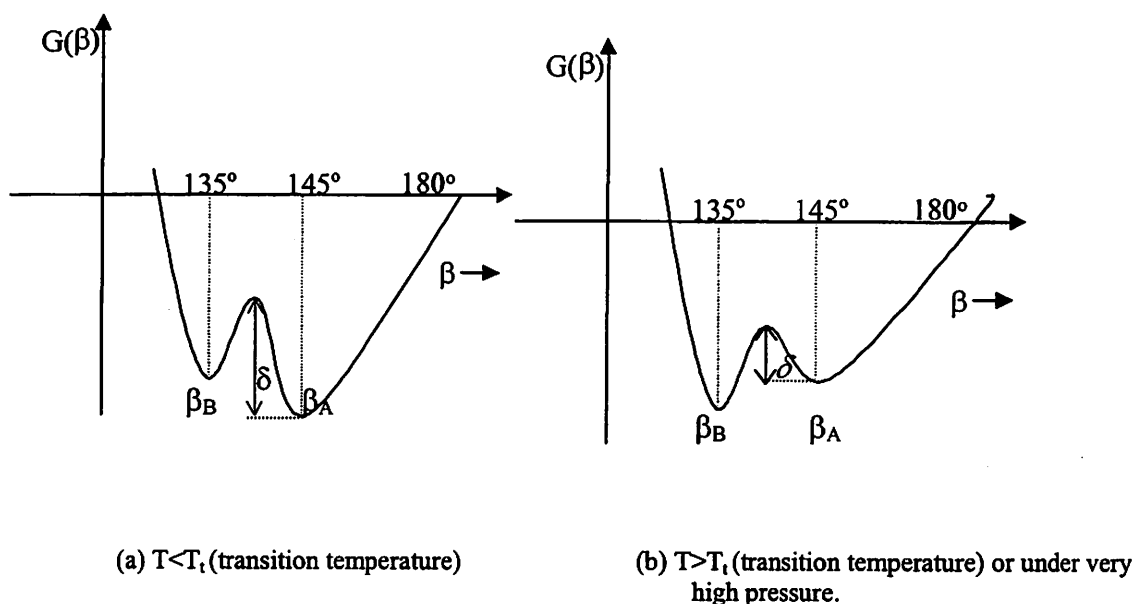


Figure 5-2. The Gibbs free energy with two minima, proposed here to explain the observed Si-O-Si angle change for heavily neutron, and ion irradiated vitreous silica.

By using the above model, we can understand the diffraction, Raman and IR data regarding the compaction of vitreous silica induced by ion, neutron bombardment and hydrostatic pressure.

When ions or neutrons bombard vitreous silica or crystal quartz, a fraction of the momentum and of the energy of the incident particle are transferred to atoms in the glass network or crystal lattice. The struck atoms (Si, O) will be displaced into interstitial positions. Primak *et al.* [48] argued that, around the site of primary knocked-on atom (about 10^4 atoms), extreme local conditions of temperature and pressure are achieved

through a “thermal spike” process. They estimated the local temperature to reach 5000-10000°C and a local pressure of 3000-7000atm. According to our two-phase model for vitreous silica, under such conditions, the phase *B* structure has the minimum free energy, so highly localized phase *B* structure will form out of phase *A*. The extremely small volume allows a rapid quench rate in the impact volume, and the high temperature phase *B* is frozen in. The entire sample could be converted to phase *B* structure provided it was exposed to sufficient neutron or ion flux such that every microscopic volume of the sample was melted. Phase *B* is called “metamict” phase, and it is distinguished from phase *A* by reducing the most probable Si-O-Si angle about 10°.

Maruyama and Hobbs have directly observed this transformation process in neutron-induced compaction in vitreous silica [49]. Using high-resolution transmission electron microscopy (TEM), they found that the initial damage in neutron-irradiated quartz was fine scale (~20-30Å) and homogenous, reflecting collision cascade disorder and that the transformation proceeded by linking of these homogeneously-distributed metamict zones.

When external hydrostatic pressure is applied to compress vitreous silica, SiO₄ tetrahedrons in the network are brought closer together. If the applied pressure is sufficiently high (>9GPa at room temperature), the bridging bond angle around β_A could jump into the β_B region as shown in Fig. 5-2(b), resulting in a phase transformation *A*→*B*. Arndt *et al.* [50] argued that this process is facilitated by an effect called the “resonating bond” that makes the energy barrier δ in Fig. 5-2 much lower than that of the valence-conduction band gap. This “reconstructive transformation” results in a substantially different structure in permanently densified vitreous silica. With this phase

transformation, Si-O-Si bridging bond angles become smaller and the whole solid contracts. Experimental evidence shows that there are broken bonds associated with this phase transformation [23,40,45]. At higher temperature, the energy barrier δ in Fig. 5-2(b) could be lower than that at room temperature. This might be the reason that McMillan *et al.* [23] observed *A* to *B* phase transformation at lower pressures.

When the hydrostatic pressure is less than 9 GPa at room temperature, the pressure is not high enough to break Si-O bond and the connectivity of SiO₂ network will not change. The structure will remain in phase *A* and in this “elastic region” in which the compaction is reversible. From infrared (IR) and Raman data, no substantial bridging bond angle changes were detected in this case [40,45].

Let's now discuss the origin of the two-phase description for vitreous silica. Vukceвич [51] has shown that even for very slight variations of the Si-O distances in a tetrahedron ($\sim 0.01 \text{ \AA}$), the Si-O-Si angle can have two values corresponding to two energy [E in Eq. (5-2)] minima of the system. This could be the physical origin of the double well structure for free energy in vitreous silica. The states of bridging oxygen are separated by a potential barrier which is due to the dependence of the potential energy on the Si-O-Si angle for each stable state and on the Coulomb repulsion of tetrahedrons for Si...Si distance changes caused by variations in the Si-O-Si angles (i.e., variation in the distance between tetrahedron centers). Diffraction experiments show that the Si-O bond length increases in vitreous silica after massive neutron irradiation or hydrostatic pressure compression [27,41].

At first sight, it might seem surprising that the application of pressure and an increase in density would lead to an increase in the Si-O bond length, but in fact, the

increased bond length is a direct consequence of the decrease in the Si-O-Si bond angle, since these two quantities are closely correlated [52]. In Gibbs free energy $G(\beta)$, there are also contributions from entropy and volume. The depth and the position of two minima of two potential wells in free energy (Fig. 5-3) change with temperature and pressure; this can explain the following phenomenon observed with infrared spectroscopy measurement in fused silica by Agarwal *et al.* [53]: when the fictive temperature increased from 950 to 1400 °C, from the, the most probable Si-O-Si bridging bond angle was computed to decrease by about 1.3°.

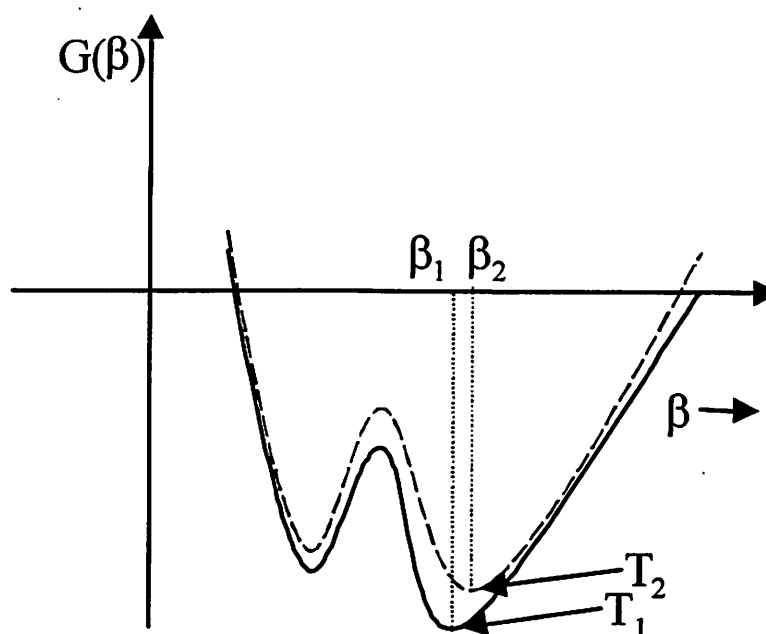


Figure 5-3. Most probable Si-O-Si angle as a function of fictive temperature T_f ($T_1 > T_2$)

In terms of the proposed angular potential, we can interpret the vitreous state of silica as an essentially random network of SiO_4 tetrahedrons in which the bridging bond angle Si-O-Si has a definite preference for the two characteristic values, β_A and β_B . At any given temperature and pressure, a certain "most probable" bridging bond angle exists in the structure that corresponds to thermodynamic equilibrium state.

The above two-phase model is further supported by Raman spectroscopy results. The Raman bands of low temperature chemical vapor deposited (CVD) SiO_2 films [53] are the same as those of high pressure-compacted samples and heavily neutron-irradiated samples. As in all as-deposited film samples, the major low-frequency band lies near 470cm^{-1} instead of the 430cm^{-1} of normal vitreous silica, indicating that in thin films, the Si-O-Si bridging bond angle is about 135° [54]. When the thin film sample is annealed, the spectrum returns to that of normal vitreous silica, indicating that the Si-O-Si angle increases to 145° .

When the film is deposited at low temperature ($T \sim 300^\circ\text{C}$), the deposited atomic species have very small thermal energies and so are constrained to remain in the position in which they have reacted on the surface to form SiO_2 . There is consequently no thermally induced relaxation of the film. It is possible that the film is frozen in the high temperature structural form, which has the characteristics of the phase *B* structure including the vibrational spectrum.

Experiments show that there are a lot of Si-OH groups in the low temperature CVD SiO_2 thin films and the density of the film is lower than that of normal vitreous silica [13-19]. Associated with high OH content, the viscosity of SiO_2 films is relatively low and this could facilitate the vitreous silica system's approach to the thermodynamic

equilibrium state during the annealing process. From our two-phase model for vitreous silica, we know that the “low” temperature phase is phase *A* and because the Si-OH bond is not as strong as Si-O-Si bonds, the phase transition ($B \rightarrow A$) happens at temperature even lower than 1000°C accompanied by Si-OH bond-breaking. After annealing, the detected OH content in the film is much less than that of the as-received sample [54].

5.4 Compaction induced by knock-on radiation

Heavy ion and neutron radiation introduce a structural phase transition in vitreous silica, and the new phase *B* has a higher density than that of *A* phase of pure vitreous silica. The energy deposited in vitreous silica converts the phase *A* structure to the phase *B* structure in localized clusters. In contrast, ionizing radiation produces network changes, which are not new phases but are distributed over a large distance throughout the elastic network.

During the particle bombardment process, we suppose that ρ_f is the observed density, ρ_0 is the density of starting silica (density of phase *A*), ρ_B is the density of vitreous silica in phase *B*, and x is the molar fraction portion of the matrix in phase *B*. We have the following relation

$$\rho_f = (1-x)\rho_0 + x\rho_B = \rho_0 + x(\rho_B - \rho_0). \quad (5-3)$$

Since there is no overlap of the damaged clusters in the initial stage of the damage, it is intuitive to assume that x increases with dose linearly. From Eq. (5-3), the density of the vitreous silica increases with deposited energy dose linearly. If we deposit more energy into vitreous silica, more atoms will be displaced and more phase *B* structure will form.

Eventually, the whole structure will be in phase *B*; and this is what we called metamict phase.

5.5 Conclusions

The density of fused silica increases linearly with the absorbed dose when exposed to atomic displacement radiation such as neutrons. The diffraction data suggest that the internal structure of fused silica undergoes a dramatic change during radiation. In order to explain the observed physical property changes, we studied the previous theoretical and experimental results, and propose a two-phase model.

In this chapter the physical condition generated by knock-on radiation is examined. We concluded that the “knock-on” radiation generally triggers a phase transition in the fused silica network. The new phase *B* has smaller Si-O-Si bridging bond angles and higher density than the structure of phase *A*. The metamict phase observed in neutron damage experiments is easily understood. Our two-phase model can also be used to explain the structure change in pressure compressed fused silica.

5.6 References:

- [1] W.Primak, R.Kampwirth, "Radiation Compaction of Vitreous Silica", Journal of Applied Physics, 39, 5651 (1968)
- [2] W.Primak, R.Kampwirth, "Impurity Effect in the Ionization Dilation of Vitreous Silica", J. Appl. Phys., 39, 6010 (1968)
- [3] F. L. Galeener, "Nonlinear gamma -ray activation of defect spins in vitreous silica". Journal of Non-Crystalline Solids, vol.149, 27 (1992)
- [4] J. A. Ruller, E. J. Friebele, "The effect of gamma-irradiation on the density of various types of silica". Journal of Non-Crystalline Solids, vol.136, 163 (1991)
- [5] J. E. Shelby, "Effect of radiation on the physical properties of borosilicate glasses". Journal of Applied Physics, vol.51, 2561 (1980)
- [6] J. E. Shelby, "Effect of morphology on the properties of alkaline earth silicate glasses". Journal of Applied Physics, vol.50, 3702 (1979)
- [7] P. L. Higby, E. J. Friebele, C. M. Shaw, M. Rajaram, E. K. Graham, D. L. Kinser, E. G. Wolff, J. Am. Ceram. Soc. 71, 796 (1988)
- [8] E. J. Friebele, P. L. Higby, in *Laser Induced Damage in Optical Materials*, 1987 NIST Spec. Pub. 756, edited by H. H. Bennett, A. H. Guenther, D. Milam, B. E. Newnam, M. J. Soileau (NIST, Boulder, CO. 1988), p. 89
- [9] M. Rajaram, T. Tsai, E. J. Friebele, "Radiation-induced surface deformation in low-thermal-expansion glasses and glass-ceramics". Advanced Ceramic Materials, vol.3, 598 (1988)
- [10] C. I. Merzbacher, E. J. Friebele, J. A. Ruller, P. Matic, "Long-wavelength infrared transmitting glasses: new ternary sulfide compositions". Proceedings of the SPIE - The International Society for Optical Engineering, vol.2018, 222 (1991)
- [11] T. A. Dellin, D. A. Tichenor, E. H. Barsis, J. Appl. Phys. 48, 1131 (1977)
- [12] C. B. Norris, E. P. EerNisse, "Ionization dilation effects in fused silica from 2 to 18-keV electron irradiation". Journal of Applied Physics, vol.45, 3876 (1974)

- [13] C. Smith, N. F. Borrelli, D. C. Allan, "Compaction of fused silica under low fluence/long term 193 nm irradiation". Proceedings of the SPIE - The International Society for Optical Engineering, vol.3051, 116 (1997)
- [14] D. C. Allan, C. Smith, N. F. Borrelli, T. P. Seward III, "193-nm excimer-laser-induced densification of fused silica". Optics Letters, vol.21, 1960 (1996)
- [15] P. Schermerhorn, "Excimer laser damage testing of optical materials". Proceedings of the SPIE - The International Society for Optical Engineering, vol.1835, 70 (1993)
- [16] M.Rothschild, D.J.Ehrlich, D.C.Shaver, "Effects of excimer laser irradiation on the transmission, index of refraction, and density of ultraviolet grade fused silica", Appl. Phys. Lett. 55 (13), 1276 (1989)
- [17] D.J.Krajnovich, I.K.Pour, A.C.Tam, W.P.Leung, M.V.Kulkarni, "Sudden onset of strong absorption followed by forced recovery in KrF laser-irradiated fused silica", Optics Letters, 15 Vol. 18 453-455 (1993)
- [18] R. Schenker, P. Schermerhorn, W. G. Oldham, "Deep-ultraviolet damage to fused silica". Journal of Vacuum Science & Technology B (Microelectronics and Nanometer Structures), vol.12, 3275 (1994)
- [19] R. E. Schenker, F. Piao, W. G. Oldham, "Material limitations to 193-nm lithographic system lifetimes". Proceedings of the SPIE - The International Society for Optical Engineering, vol.2726, 698 (1996)
- [20] Ch. Meade, R. J. Hemley, H. K. Mao, Phys. Rev. Lett. 69,1387 (1992)
- [21] S. Susman, K. J. Volin, D. L. Price, M. Grimsditch, J. P. Rino, R. K. Kalia, P. Vashishta, G. Gwanmesia, Y. Wang, R. C. Liebermann, "Intermediate-range order in permanently densified vitreous SiO₂: A neutron-diffraction and molecular-dynamics study". Physical Review B (Condensed Matter), vol.43 1194 (1991)
- [22] R.A.B.Devine, "Macroscopic and microscopic effects of radiation in amorphous SiO₂". Nuclear Instruments & Methods in Physics Research, Section B (Beam Interactions with Materials and Atoms), vol. B91, 378-390 (1994)
- [23] P.McMillan, B.Piriou, R.Couty, "A Raman study of pressure-densified vitreous silica". Journal of Chemical Physics, vol.81, 4234 (1984)
- [24] W.Primak, M.Bohmann, Prog. Ceram. Sci. 2, 103 (1962)
- [25] W.Primak, The Compacted States of Vitreous Silica (Gordon and Breach, New York, 1975)

- [26] W.Primak, Phys. Rev. 110, 1240 (1960)
- [27] A.C.Wright, B.Bachra, T.M.Brunier, R.N.Sinclair, L.F.Gladden, R.L.Portsmouth, "A neutron diffraction and MAS-NMR study of the structure of fast neutron irradiated vitreous silica". Journal of Non-Crystalline Solids, 69, 150 (1992)
- [28] R.H.Stolen, J.T.Krause, C.R.Kurkjian, "Raman scattering and far infra-red absorption in neutron compacted silica". Discuss. Faraday Soc., 50 (103)1970
- [29] W.Primak, Phys. Rev., 110, 1240-1254 (1958)
- [30] W.Primak, Phys. Chem. Solids, 13, 279-286 (1960)
- [31] M.C.Wittels, Phys. Rev., 89, 656-657 (1953)
- [32] M.C.Wittels, F.A.Sherrill, Phys. Rev., 93, 1117-1118 (1954)
- [33] E.W.J.Mitchell, E.G.S.Paige, Phil. Mag. 1, 1085-1115 (1956)
- [34] G.S.Zhdanov, V.G.Zubov, O.L.P.Kolontsova, I.V.Telegina, Soviet Physics---Crystallography, 8, 154-158 (1963)
- [35] G.Mayer, M.Lecomte, J. Phys. Radium 21,, 846-852 (1960)
- [36] I.Simon, J. Am. Ceram. Soc. 41, 116 (1958)
- [37] E.Lell, N.J.Kreidl, J.R.Hensler, in Radiation Effects in Quartz, Silica and Glasses, Pergamon Press(1966)
- [38] in "The physics and technology of amorphous SiO₂". Edited by R.A.B.Devine
- [39] F.L.Galeener, F.A.Barrio, E.Martinez, R.J.Elliott, Phys. Rev. Lett. 53, 2429 (1984)
- [40] G.E.Walrafen, P.N.Krishnan, "Raman spectrum of pressure compacted fused silica". Journal of Chemical Physics, vol.74, 5328 (1981)
- [41] S.Susman, K.J.Volin, R.C.Liebermann, G.D.Gwanmesia, Y.Wang, "Structural changes in irreversibly densified fused silica: implications for the chemical resistance of high level nuclear waste glasses". Physics and Chemistry of Glasses, vol.31, 144 (1990)
- [42] P.W.Bridgman, I.Simon, J. Appl. Phys. 24, 405 (1953); H.M.Cohen, R.Roy, Phys. Chem. Glasses, 6, 149 (1965)
- [43] J.D.MacKenzie, J. Am. Ceram. Soc. 46, 470 (1963)
- [44] R.Bruckner, J. Non-cryst. Solids, 5, 123 (1970)

- [45] R.J.Hemley, H.K.Mao, P.M.Bell, B.O.Mysen, Phys. Rev. Lett. 57, 747 (1981)
- [46] M.Grimsditch, Phys. Rev. Lett. 52, 2379 (1986)
- [47] F.L.Galeener, in The Physics and Technology of Amorphous SiO₂, ed. R.A.B.Devine, Plenum Press (1987)
- [48] W.Primak, Phys. Rev. 133, A531 (1964)
- [49] T.Maruyama and L.W.Hobbs, Am. Ceram. Soc. Bull. 67, 574 (1988)
- [50] J.Arndt, R.A.B.Devine, A.G.Revesz, "Anomalous behaviour of the refractive index during the annealing of densified, amorphous SiO₂". Journal of Non-Crystalline Solids, vol.131, 1206 (1991)
- [51] M.R.Vukceвич, "A new interpretation of the anomalous properties of vitreous silica". Journal of Non-Crystalline Solids, vol.11, 25 (1972)
- [52] G.V.Gibbs, M.M.Hamil, S.J.Louisnathan, L.S.Bartell, H.Yow, Am. Mineral. 57, 1578 (1972)
- [53] A.Agarwal, K.M.Davis, M.Tomożawa, "A simple IR spectroscopic method for determining fictive temperature of silica glasses". Journal of Non-Crystalline Solids, vol.185, 191 (1995)
- [54] M.Huffman, P.McMillan, "Infrared and Raman studies of chemically vapor deposited amorphous silica". Journal of Non-Crystalline Solids, vol.76, 369 (1985)

Chapter 6

Theory of Ionization-Induced Compaction in Fused Silica

6.1 Introduction

The UV-induced compaction in all of the fused silica samples we tested follows

$$\frac{\Delta\rho}{\rho} = A' D_a^c \quad (6-1)$$

with $c \sim 0.66$. Similar stretched power dependence of density change on absorbed radiation dose were observed in fused silica after exposure to γ -ray [1-5], e-beam [1,2,6-11] and ultraviolet (UV) radiation [12-18]. Although the types of radiation and the types of fused silica tested are different, the dose exponent c is generally found in the range of 0.55 to 0.80. The origin of this behavior [1,19,20] has been explained in terms of irradiation induced “hardening” [21]. In all experiments we just mentioned, an ionization process is believed to be dominant in inducing compaction because of the small probability for knock-on processes. Even though different fused silica samples have different impurity levels and different processing histories, they are all amorphous structures and are in a non-equilibrium state at room temperature, i.e.; all are in a super-cooled liquid state. We propose that the “universal” dose exponent of 0.66 is an intrinsic property of fused silica when it is densified by ionizing radiation and it is directly related to the structure of the fused silica.

6.2 Ionizing-induced compaction in fused silica

The random network model for fused silica consists of a three-dimensional random network of rigid tetrahedral SiO_4 molecular units. Neighboring units in the

structure are linked at vertices by sharing a common or bridging oxygen atom. Although the SiO_4 units themselves are regular in shape, the mutual orientation of adjacent units can vary widely throughout the silica glass in a random manner, subject only to the restriction that the network be continuously connected [22]. X-ray diffraction structural investigations show that the Si-O-Si angle distribution is rather broad (from 120° to 180°) with the maximum at 144° [23, 24].

For ionization (UV, low energy electron beam and gamma) induced compaction in vitreous silica, the dose exponent c is about 0.66 ($2/3$) and early experiments show that knock-on damage is much more effective in causing compaction in vitreous silica than ionization damage [25]. Also from the last chapter, we know that the phase transformation ($A \rightarrow B$) happens through the change of topology of the network. This can only be achieved by the collective movement of many atoms. But in deep ultraviolet (193nm and 248nm) induced compaction experiments, there was no threshold energy detected and the conditions for the “thermal spike” mechanism do not exist. In our 193-nm UV induced compaction experiments [16], we could detect a 200ppB density change in fused silica samples when the absorbed UV dose was 10^5 rad. If it takes 8 eV (band gap of fused silica) to break one Si-O bond, there will be one broken bond in every 10^4 Si-O bonds. At this low concentration, the broken bonds will not likely give SiO_4 tetrahedrons enough freedom to move to change the network connectivity. All of this suggests a different mechanism for ionization damage from that of knock-on damage in vitreous silica. To understand this sub-linear power dependent compaction behavior, we look at the structure of vitreous silica first.

6.3 Boltzmann distribution function of bridging bond angles

In the molten SiO_2 structure, the spatial packing becomes less and less tight with increasing temperature owing to the changing orientation of each SiO_4 tetrahedron with respect to the surrounding tetrahedrons. This has been observed by direct IR and X-ray measurements on the bridging bond angle distribution of silica glasses that have different fictive temperature T_f [26]. In a phase A structure, the bridging bond angle has a broad distribution as X-ray diffraction revealed, and this distribution becomes broader at higher fictive temperature T_f as shown in Fig. 6-1.

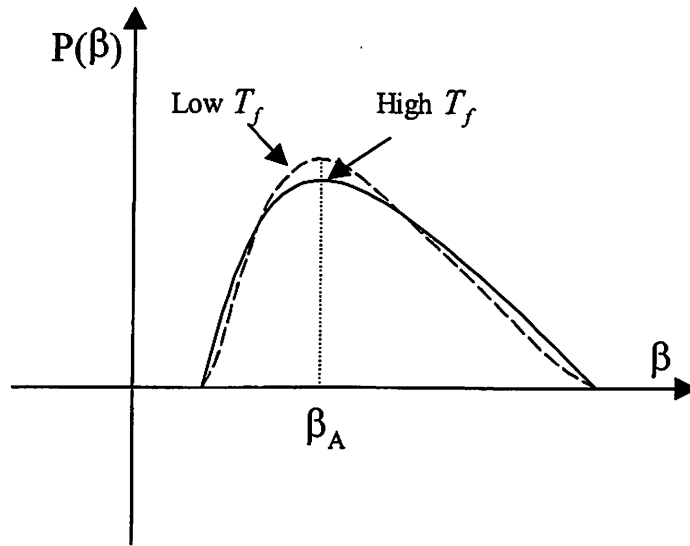


Figure 6-1. Bridging bond angle distribution as a function of fictive temperature T_f . The high T_f state has a broader angle distribution compared to that of the low T_f state.

Quantitatively, the Si-O-Si angle may be simply described by a distribution function $\rho(\beta)$, where $\rho(\beta)d\beta$ defines the number of Si-O-Si bridging bond angles in the range from β to $\beta + d\beta$, and the total number of Si-O-Si bonds is given by:

$$N = \int \rho(\beta) d\beta . \quad (6-2)$$

In order to find the distribution of the Si-O-Si bond angles in fused silica, we use a thermodynamic approach at high temperature to estimate the frozen-in bond angle distribution. We consider the bridging bonds β that are not equal to the most probable angle β_A as point defects in silica [27]. The Gibbs free energy G of the whole system, the system's configurational entropy S , the number of bridging bonds n_i which have a specific value of β , as well as the Gibbs free energy ϕ_i , the internal energy ε_i , the entropy s_i , and the volume v_i associated with each bridging bond labeled by i , are defined by the relations

$$G(\beta_A, T) = \sum_{i=0}^m n_i \phi_i - TS \quad (6-3)$$

$$S = \kappa_B \ln \frac{N!}{n_1! n_2! \dots n_m! n_0!} \quad (6-4)$$

$$\text{where } n_0 = N - \sum_{i=1}^m n_i \quad (6-5)$$

is the number of bridging bonds with angle of β_A , and

$$\phi_i = \varepsilon_i - Ts_i + pv_i . \quad (6-6)$$

We will assume that the fused silica is first in a thermal equilibrium state at the fictive temperature T_f from which it is quenched. At T_f , the Gibbs free energy of the whole system takes the minimum value and we obtain

$$n_i(\beta) = n_0 \exp[(\phi_0 - \phi_i) / \kappa_B T_f] , \quad (6-7)$$

where κ_B is the Boltzmann constant and the free energy ϕ_i is a function of bridging bond angle β . After the silica glass is quenched, the equilibrium structure (Si-O-Si

bridging bond angles) at the fictive temperature is frozen in. Thus we use the above Boltzmann distribution at fictive temperature T_f [Eq. (6-7)] to describe the distribution function of the Si-O-Si bridging bond angle β in fused silica;

$$\rho(\beta) = f(T_f) \exp[-\varphi(\beta) / \kappa_B T_f]. \quad (6-8)$$

where $\varphi(\beta)$ is the continuous functional form of φ_i and $f(T_f)$ is the normalizing factor.

Because it is generally believed that the SiO_4 tetrahedron is a very rigid structure and remains the same before and after radiation damage [28,29], the bridging bond angle β is the coordinate to describe the structural change of fused silica with radiation damage. The free energy $\varphi(\beta)$ can be expanded around the most probable angle β_A in a polynomial form as

$$\varphi(\beta) = \varphi(\beta_A) + \frac{a_1}{2}(\beta - \beta_A)^2 - a_2(\beta - \beta_A)^3 + a_3(\beta - \beta_A)^4 + \dots \quad (6-9)$$

where a_1 , a_2 and a_3 are constants.

The Si-O-Si bridging bond angle distribution in vitreous silica is non-symmetric according to the diffraction measurement of R.L.Mozzi *et al.* (Fig. 6-2) [23]. The number of bridging bonds on the $\beta < \beta_A$ side is less than that of bridging bonds on the $\beta > \beta_A$ side. Hence both a_1 and a_2 in Eq. (6-9) are positive. This asymmetry can be explained by the strong repulsive force between the two SiO_4 tetrahedrons with smaller bridging bond angles.

In Fig. 6-2, the circled points are the experimental data digitized from X-ray diffraction measurement of Si-O-Si bridging bond angle distribution in vitreous silica [23]. We use Eq. (6-8) and (6-9) to fit these experimental data. Since we do not have any

information about the T_f , we choose T_f in the range from 1000 °C to 1500 °C [26, 30]. For this range of T_f , a_1 lies in the range from 1.36eV to 1.86eV from this curve fitting process. As an example, in Fig. 6-2, we plotted the fitting curve when T_f is 1200°C. In this fit, $a_1 = 1.64\text{eV}$, $a_2 = 1.69\text{eV}$ and $a_3 = 2.67\text{eV}$ (angles are in the unit of radians).

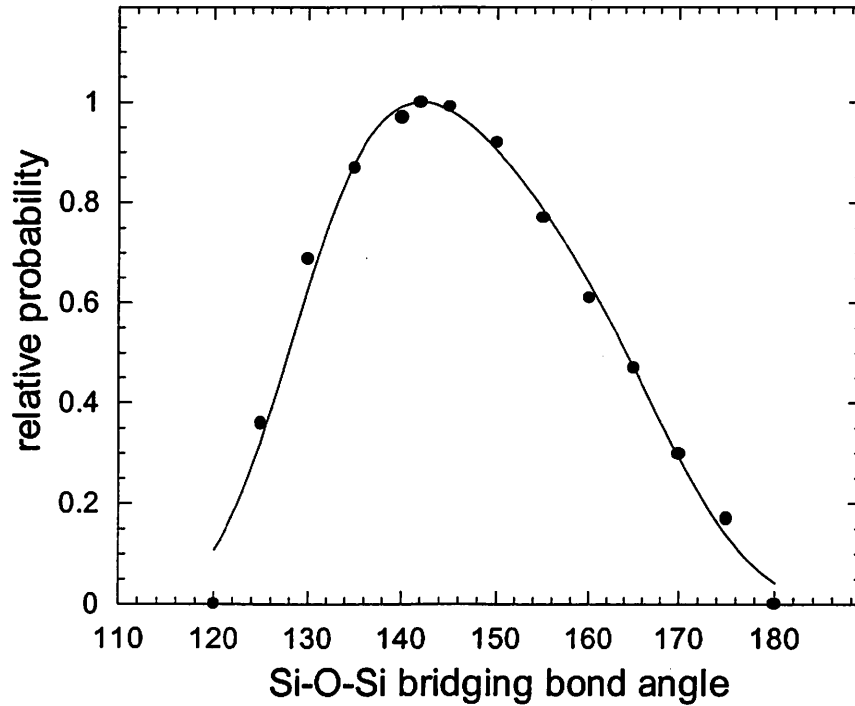


Figure 6-2. Using Boltzmann distribution to fit the X-ray diffraction data for Si-O-Si bridging bond angle distribution in vitreous silica.

When $(\beta - \beta_A)$ is small, let's say $\ll 1$, the potential $\phi(\beta)$ can be approximated by a oscillator potential as

$$\phi(\beta) = \phi(\beta_A) + \frac{a_1}{2}(\beta - \beta_A)^2, \text{ when } (\beta - \beta_A) \ll 1. \quad (6-10)$$

Here a_1 is the “spring constant” of the bending of Si-O-Si bridging bond, which can be compared with the measured IR spectroscopic data for fused silica. Such measurements have been analyzed by Jan Bock *et al.* [31]. The most probable value of the force constant for Si-O-Si bond bending is 5.0×10^3 dynes/cm. By using the Si-O distance obtained from the X-ray diffraction data obtained by Warren *et al.*, $d_{\text{Si-O}} = 1.61 \text{ \AA}$, we get $a = 1.64 \text{ eV}$ which is consistent with the value extracted from curve fitting of the X-ray diffraction curve.

6.4 The relaxation of bridging bond angles

According to the fictive temperature model, the fused silica structure is frozen into a state characteristic of the high temperature T_f ; thus the structure is in a non-thermal-equilibrium state at room temperature. Its excess energy is stored in the Si-O-Si bridging bonds. This excess energy acts as a driving force for the relaxation process in fused silica induced by breaking atomic bonds. During densification, ionization produces electron-hole pairs, providing paths for bond rearrangements, reducing the constraints on structural relaxation. The relaxation process releases some of the excess energy stored in the structure accompanied by a decrease of the average bridging bond (Si-O-Si) angle. The decrease of the average bridging bond angle in fused silica shows its macroscopic effect as compaction.

The structural rearrangement may be visualized as relaxation in a three-dimensional strained-spring network. The springs are connected to each other. Even though there is excess energy stored in the network, the whole structure just stays in its original state if all connections are intact. However if one spring connection is broken,

the system acquires additional freedom with the result that the whole network relaxes to a lower energy state. Because of the connectivity and the absence of regular (crystalline) structure, the relaxation involves long-range effects; essentially the entire structure participates. The network structure of glass is similar to that of the strained spring network: an ionization event initiates relaxation, allowing the bridging bond angle distribution to move toward the most probable angle β_A by releasing excess free energy stored in the network. The relaxation in the average deviation of Si-O-Si bond angle $\beta - \beta_A$ results in a decreasing response of the structure to the radiation, and can be thought as a kind of “hardening” effect [21]. The sub-linear dependence of the compaction rate on absorbed UV dose is a consequence.

In the annealing studies carried out for deep UV-compacted fused silica (see Chapter 4), an activation energy of 0.13eV is found for the compaction recovery process. This low energy is equivalent to $\kappa_B T$ at 1300°C, which is comparable to the fictive temperature in most vitreous glass [30]. Breaking bonds in the network causes the overall bridging bond angle distribution to shrink; the excess free energy is reduced. At the same time, broken bonds are associated with dangling electrons and defects. If we anneal the damage at high temperature, the shrunk Si-O-Si bonds would expand and have some dangling electrons rebond. The energy barrier for this recovery process should be at the same level as $\kappa_B T_f$. Our relaxation model for densification induced by ionization is supported by the small activation energy.

6.5 Compaction model for ionizing radiation

The following mathematical treatment is helpful to understand the sub-linear power dependence of the compaction in fused silica on the absorbed ionizing radiation dose. We use the above bridging bond relaxation model and assumed a simple relaxation mechanism.

Since the ionization-induced Si-O-Si bridging bond angle relaxation is achieved by the rotation of SiO_4 tetrahedrons and their movement is restricted by their connection to the other SiO_4 tetrahedrons; there is no reason to believe that some specific bridging bonds always shrink faster or slower than the others. We assume that every ionization event produces, statistically speaking, the same net amount of relaxation (represented by a parameter ω here) for each bridging bond angle ($\beta \neq \beta_A$) in the relaxed region. For example, if there are 10 bridging bonds with the value of $(\beta - \beta_A) = 10\omega$ in the relaxed region, one ionization event will cause a 10ω total angle shrinkage for these bridging bonds. For mathematical simplicity, we can also view this process as one in which one bridging bond shrinks to β_A while the other 9 bridging bonds remain unchanged. Thus, the relaxation process for the bridging bonds with a specific value β can be described by the equation

$$d[n(\beta)] = -\frac{n(\beta)\omega d(D_a)}{|\beta - \beta_A|\mu} \quad (6-11)$$

where $n(\beta)$ is the number of bridging bonds which have an angle β inside the relaxed fused silica structure, D_a is the absorbed radiation dose and μ is the energy needed to create one effective ionization event.

The solution to Eq. (6-11) is given by

$$n(\beta, D_a) = \rho(\beta) \exp\left[-\frac{\omega D_a}{|\beta - \beta_A| \mu}\right]. \quad (6-12)$$

We define a reference state to be the saturated state in which all angles are β_A . Then we can compute the relation between absorbed radiation dose and the relaxation of bond angle in fused silica by counting the weighted sum Φ of all bridging bond angles deviating from the reference state:

$$\Phi(D_a) = \int_0^\pi (\beta - \beta_A) \rho(\beta) \exp\left[-\frac{\omega D_a}{|\beta - \beta_A| \mu}\right] d\beta. \quad (6-13)$$

Setting $\zeta = (\beta - \beta_A)$, we obtain

$$\Phi(D_a) = f(T_f) \cdot \int_{-\beta_A}^{\pi-\beta_A} \zeta \exp(-a_1' \zeta^2 + a_2' \zeta^3 - a_3' \zeta^4 - \nu_0 D_a |\zeta|^{-1}) d\zeta \quad (6-14)$$

with $a_1' = a_1 / 2\kappa_B T_f$, $a_2' = a_2 / \kappa_B T_f$, $a_3' = a_3 / \kappa_B T_f$ and $\nu_0 = \omega / \mu$.

Because the observed ionization-induced densification level in fused silica is very small ($\frac{\Delta\rho}{\rho} \sim 10^{-6}-10^{-3}$) for very large absorbed radiation doses (see Table 3-2), we conclude from Eq. (6-11) that $\nu_0 D_a \ll 1$. Thus in Eq. (6-14), only the bridging bond angles with $\zeta \ll 1$ are important to the dependence of $\Phi(D_a)$ on D_a (since $\nu_0 D_a \ll a_1', a_2', a_3'$). The integral in Eq. (6-14) can be split into three parts

as $\int_{-\beta_A}^{\pi-\beta_A} = \int_{-\gamma}^{\gamma} + \int_{-\beta_A}^{-\gamma} + \int_{\gamma}^{\pi-\beta_A}$, where γ is a small quantity ($\gamma \ll \beta_A$). The dependence of $\Phi(D_a)$

on D_a can be found by solving the following integral;

$$\Phi(D_a) \sim f(T_f) \cdot \int_{-\gamma}^{\gamma} \zeta \exp(-a_1' \zeta^2 + a_2' \zeta^3 - a_3' \zeta^4 - \nu_0 D_a |\zeta|^{-1}) d\zeta \quad (6-15)$$

When we consider the net contribution of the non-symmetric distribution of the bridging bond angle β around β_A , we can then expand the exponential functions in Eq. (6-15) around $\zeta=0$, and get,

$$\Phi(D_a) \sim f(T_f) \cdot \int_0^{\gamma} 2a_2' \zeta^4 \exp(-a_1' \zeta^2 - \nu_0 D_a \zeta^{-1}) d\zeta. \quad (6-16)$$

With $y = \zeta^5$, Eq. (6-16) can be written as

$$\Phi(D_a) \sim f(T_f) \cdot \int_0^{\gamma} 2a_2' \exp(-a_1' y^{2/5} - \nu_0 D_a y^{-1/5}) dy \quad (6-17)$$

The exponential function in Eq. (6-17) is a fast decaying function, the main contribution to the above integral is from the saddle-point of $F(y) = a_1' y^{2/5} + \nu_0 D_a y^{-1/5}$. Thus the value of $F(y)$ at its saddle-point determines the asymptotic relation between $\Phi(D_a)$ and D_a ,

$$\Phi(D_a) \sim B' \exp(-\eta D_a^c) \quad (6-18)$$

with

$$c = 2/3 \quad (6-19)$$

where B' is a slowly varying function of D_a and η is a constant.

From Eq. (6-18), we see that the net effect of structural relaxation is a decrease of the total bridging bond angle in the fused silica. Since the Si-O distance remains unchanged, a decrease of Si-O-Si angle is equivalent to decreasing the Si to Si distance. The average distance between Si atoms will change in the following way relative to the initial state at which the dose parameter is zero,

$$\Delta d_{Si-Si} \propto \frac{\Phi(0) - \Phi(D_a)}{N} \quad (6-20)$$

here d_{Si-Si} is the average Si to Si distance and N is the total number of Si-O-Si bridging bonds in fused silica.

When Δd_{Si-Si} is small, the volume change is proportional to it. We get the relative volume change

$$\frac{\Delta V}{V} \propto \frac{\Delta d_{Si-Si}}{d_{Si-Si}} \propto [1 - \exp(-\eta D_a^c)]. \quad (6-21)$$

We can further expand the exponential function and get

$$\frac{\Delta V}{V} = -\frac{\Delta \rho}{\rho} \propto D_a^{2/3}. \quad (6-22)$$

6.6 Discussion

According to our model, different ionizing compaction rates are expected if fused silica samples have different fictive temperatures. Owing to the different manufacturing processes, the bridging bond angle distributions vary from sample to sample. As a first order approximation, we use a single parameter, the fictive temperature T_f , to describe the bridging bond angle distribution. In fused silica, high T_f structures have more excess free energy stored in the distorted Si-O-Si bonds ($\beta \neq \beta_A$) compared to the low T_f structures. In the ionizing radiation-induced compaction, excess free energy is the driving force for the bridging bond shrinking. And we expect that fused silica samples with higher fictive temperature show higher compaction rates.

From Fig. 3-6, we see that the damage rates for samples A, B, D and F follow the order $D(B) < D(D) < D(F) < D(A)$. Accordingly, we assign the fictive temperatures for these samples in the order of $T_f(A) > T_f(F) > T_f(D) > T_f(B)$. Even though we do not have a detailed understanding of the processes involved in the thermal recovery of UV-induced compaction, we observed a lower UV-induced compaction rate for all tested fused silica samples in higher ambient temperature environment. This suggests that the final relaxed state in the silica network is determined by the environmental temperature. Thermal energy causes reconfiguration of the atoms in the silica structure. Based on our compaction theory there are fewer constraints to restrict the movements of the SiO_4 tetrahedrons in the compacted regions. Therefore the thermal annealing will convert the compacted regions to a state close to the thermodynamic equilibrium state at the annealing temperature. When the annealing temperature equals the fictive temperature T_f , the thermal recovery of the compaction will be complete. This implies that the thermal recovery of the UV-induced compaction depends on the ratio of T/T_f , where T is the annealing temperature. In Fig. 4-7, we can see that at 500°C , the compaction recovery saturation levels \mathcal{R}_s for these four samples are in the same order of their compaction rates. This observation agrees with our theoretical prediction. The compaction rate for pre-UV-irradiated sample B recovered completely after 2 hours 600°C annealing [Fig. 4-9(a)] further suggesting that the fictive temperature for sample B be very close to 600°C . Meanwhile, the compaction rate for the pre-UV-irradiated sample F [Fig. 4-9(b)], after 2 hours 600°C annealing, did not fully recover. In turn this suggested that the fictive temperature for sample F is higher than 600°C .

From earlier literature [30] we know that we can manipulate the fictive temperature of silica samples through annealing. Our compaction theory implies that annealing a sample at any temperature above its fictive temperature should increase its UV-induced compaction rate. After annealing one hour at 950°C, sample B did show a higher UV damage rate compared to that of the virgin sample B, and the same was true for sample D [Fig. 4-13(a)]. More interestingly, these two samples after this 950°C one hour annealing cycle showed almost identical UV damage curves and these curves were still lower than the damage curves for the virgin samples A and F. This suggests that the fictive temperatures for samples A and F are higher than 950°C. From Fig. 4-13(b) we can see that after a 950°C, one-hour annealing cycle, sample A and F showed no changes in their compaction curves from that of virgin samples.

Generally, for deep ultraviolet (DUV) optics, researchers have tried different schemes to lower the UV damage susceptibility, such as pre-compression of the sample or synthesizing silica with high OH content. From our point of view, all of these schemes narrow the Si-O-Si bridging bond angle distribution and are equivalent to lowering the fictive temperature of silica. Because the viscosity of fused silica depends on its OH content [32,33], high OH content silica has low viscosity at a given temperature. It is relatively easier for high OH content silica to approach the thermal equilibrium state at lower temperature; the silica with high OH content usually has a low effective fictive temperature. An X-ray diffraction experiment determined that with the same thermal history, high OH content (1200ppm) glass has a fictive temperature of 1200°C in contrast to that of the low OH content (100ppm) glass with a fictive temperature of 1400°C [26]. Therefore, the ionization induced compaction rate for “wet” fused silica should be lower

compared to “dry” fused silica if rest of the producing processes is the same. This has been observed in deep UV-induced compaction in fused silica.

In our model, the most probable bridging bond angle β_A will remain essentially unchanged in the UV-induced compaction process. This is consistent with the observation that the Raman spectrum shows no changes in the density of D2 “defects” between deep ultraviolet irradiated and unirradiated fused silica [34]. The D2 “defects” are assigned to the strained three-fold ring structure in fused silica [35]. So far, there is no direct measurement of the change of β_A for pure ionization-induced compaction in vitreous silica. Such a measurement is extremely difficult because of the very small compaction values achieved in normal ionizing radiation experiments. But even if there is some change in β_A with radiation, we expect this effect to be second order in comparison to the narrowing of the distribution of bridging bond angles.

6.7 Conclsions

Deep ultraviolet (DUV) irradiation causes compaction in fused silica. The stretched power dependence of the density on dose can be understood as an intrinsic characteristic of the amorphous structure of fused silica. The excess free energy stored in the Si-O-Si bridging bonds in fused silica acts as the driving force for the densification process. The difference in the compaction rates among the samples can be explained by their different fictive temperatures. This theory helps us in understanding the very complicated results from thermal annealing experiments.

6.8 References:

- [1] W.Primak, R.Kampwirth, "Radiation Compaction of Vitreous Silica", J. Appl. Phys. 39, 5651 (1968)
- [2] W.Primak, R.Kampwirth, "Impurity Effect in the Ionization Dilation of Vitreous Silica", J. Appl. Phys., 39, 6010 (1968)
- [3] F. L. Galeener, "Nonlinear gamma -ray activation of defect spins in vitreous silica". Journal of Non-Crystalline Solids, vol.149, 27 (1992)
- [4] J. A. Ruller, E. J. Friebele, "The effect of gamma-irradiation on the density of various types of silica". Journal of Non-Crystalline Solids, vol.136, 163 (1991)
- [5] J. E. Shelby, "Effect of radiation on the physical properties of borosilicate glasses". Journal of Applied Physics, vol.51, 2561 (1980)
- [6] P. L. Higby, E. J. Friebele, C. M. Shaw, M. Rajaram, E. K. Graham, D. L. Kinser, E. G. Wolff, "Radiation effects on the physical properties of low-expansion-coefficient glasses and ceramics". Journal of the American Ceramic Society, vol.71, 796 (1988)
- [7] E. J. Friebele, P. L. Higby, in *Laser Induced Damage in Optical Materials*, 1987 NIST Spec. Pub. 756, edited by H. H. Bennett, A. H. Guenther, D. Milam, B. E. Newnam, M. J. Soileau (NIST, Boulder, CO. 1988), p. 89
- [8] M. Rajaram, T. Tsai, E. J. Friebele, "Radiation-induced surface deformation in low-thermal-expansion glasses and glass-ceramics". Advanced Ceramic Materials, vol.3, 598 (1988)
- [9] C. I. Merzbacher, E. J. Friebele, J. A. Ruller, P. Matic, "Long-wavelength infrared transmitting glasses: new ternary sulfide compositions". Proceedings of the SPIE - The International Society for Optical Engineering, vol.2018, 222 (1991)
- [10] T. A. Dellin, D. A. Tichenor, E. H. Barsis, J. Appl. Phys. 48, 1131 (1977)
- [11] C. B. Norris, E. P. EerNisse, "Ionization dilation effects in fused silica from 2 to 18-keV electron irradiation". Journal of Applied Physics, vol.45, 3876 (1974)
- [12] P. Schermerhorn, "Excimer laser damage testing of optical materials". Proceedings of the SPIE - The International Society for Optical Engineering, vol.1835, 70 (1993)
- [13] M.Rothschild, D.J.Ehrlich, D.C.Shaver, "Effects of excimer laser irradiation on the transmission, index of refraction, and density of ultraviolet grade fused silica", Appl. Phys. Lett. 55 (13), 1276 (1989)

- [14] D.J.Krajnovich, I.K.Pour, A.C.Tam, W.P.Leung, M.V.Kulkarni, "Sudden onset of strong absorption followed by forced recovery in KrF laser-irradiated fused silica", *Optics Letters*, 15 Vol. 18 453-455 (1993)
- [15] R. Schenker, P. Schermerhorn, W. G. Oldham, "Deep-ultraviolet damage to fused silica". *Journal of Vacuum Science & Technology B (Microelectronics and Nanometer Structures)*, vol.12, 3275 (1994)
- [16] R. E. Schenker, F. Piao, W. G. Oldham, "Material limitations to 193-nm lithographic system lifetimes". *Proceedings of the SPIE - The International Society for Optical Engineering*, vol.2726, 698 (1996)
- [17] C. Smith, N. F. Borrelli, D. C. Allan, "Compaction of fused silica under low fluence/long term 193 nm irradiation". *Proceedings of the SPIE - The International Society for Optical Engineering*, vol.3051, 116 (1997)
- [18] D. C. Allan, C. Smith, N. F. Borrelli, T. P. Seward III, "193-nm excimer-laser-induced densification of fused silica". *Optics Letters*, vol.21, 1960 (1996)
- [19] D. L. Griscom, M. E. Gingerich, E. J. Friebele, "Radiation-induced defects in glasses: origin of power-law dependence of concentration on dose". *Physical Review Letters*, vol.71, 1019 (1993)
- [20] D. L. Griscom, M. E. Gingerich, E. J. Friebele, "Model for the dose, dose-rate and temperature dependence of radiation-induced loss in optical fibers". *IEEE Transactions on Nuclear Science*, vol.41, 523 (1994)
- [21] W. Primak, "Expansion, crazing and exfoliation of lithium niobate on ion bombardment and comparison results for sapphire". *Journal of Applied Physics*, vol.43, 2745 (1972)
- [22] W. H. Zachariasen, *J. Am. Chem. Soc.* 54, 3841 (1932)
- [23] R.L.Mozzi, B.E.Warren, "The structure of vitreous silica". *Journal of Applied Crystallography*, vol.2, 164 (1969)
- [24] S.L.Chan, L.F.Gladden, S.R.Elliott, in: *The Physics and Technology of Amorphous SiO₂*, ed. R.A.B.Devine (Plenum, New York, 1988)
- [25] H.M.Presby, W.L.Brown, *Appl. Phys. Lett.* 24, 511 (1974)
- [26] Th.Gerber, B.Himmel, *J. Non-cryst. Solids*, 92, 407 (1987)
- [27] S.V.Nemilov, *Thermodynamic and Kinetic Aspects of the Vitreous State*, CRC Press, 1994

- [28] S. Susman, K. J. Volin, D. L. Price, M. Grimsditch, J. P. Rino, R. K. Kalia, P. Vashishta, G. Gwanmesia, Y. Wang, R. C. Liebermann, "Intermediate-range order in permanently densified vitreous SiO₂: A neutron-diffraction and molecular-dynamics study". *Physical Review B (Condensed Matter)*, vol.43 1194 (1991)
- [29] I. Simon, *J. Am. Ceram. Soc.* 40, 150 (1957)
- [30] A. Agarwal, K.M. Davis, M. Tomozawa, "A simple IR spectroscopic method for determining fictive temperature of silica glasses". *Journal of Non-Crystalline Solids*, vol.185, 191 (1995)
- [31] J. Bock, Gouq-Jen Su, "Interpretation of the infrared spectra of fused silica". *Journal of the American Ceramic Society*, vol.53, 69 (1970)
- [32] G. Hetherington, K.H. Jack, J.C. Kennedy, *Phys. Chem. Glasses*, 5(5), 130 (1964)
- [33] P.P. Bihuniak, A. Calabrese, E.N. Erwin, "Effect of trace impurity levels on the viscosity of vitreous silica". *Journal of the American Ceramic Society*, vol.66, C134 (1983)
- [34] C. Pfeleiderer, N. Leclerc, K.O. Greulich, *J. Non-Cryst. Solids*, 159, 145 (1993)
- [35] F.L. Galeener, F.A. Barrio, E. Martinez, R.J. Elliott, *Phys. Rev. Lett.* 53, 2429 (1984)

Chapter 7

Conclusions

Both stress-induced birefringence monitoring and at-wavelength (193nm) phase-shift point diffraction interferometry (PS/PDI) were used to investigate deep-UV-induced compaction in fused silica. While PS/PDI enables us to directly measure the compaction-induced optical-path-length difference (OPD) in fused silica, stress-induced birefringence method offers us a simple, highly-sensitive way to monitor compaction.

In this thesis, deep-UV (193nm) induced densification in fused silica is reviewed and some new compaction data are presented. UV-induced compaction in fused silica obeys a universal relation where, using the total energy absorbed from two-photon absorption as the dose parameter, density changes are equal to a material dependent constant times the dose parameter to a power of about 0.66 (2/3). This behavior is consistent with past compaction studies using electron beam and gamma radiation, suggesting like densification mechanisms. Despite this seemingly fundamental damage behavior, substantial differences in damage rates were found among the many fused silica samples evaluated in Chapter 3. This was an encouraging result because it suggests that more durable fused silica can be developed for UV-applications.

We investigated the thermal annealing behavior of UV-induced compaction in fused silica. We found that compaction recovery is observable at temperatures as low as 120°C. Isochronal annealing experiments showed that the apparent activation energy of this compaction recovery process is as low as 0.13eV. This value is small compared to that of viscous flow (4-7eV between 900 and 1400°C), suggesting that the observed recovery is not simply stress relaxation by viscous flow, particularly not due to the

structural re-arrangement accompanied by the disruption of Si-O bonds. Thermal annealing of the uniformly compacted samples showed the recovery of the compaction rate supports our compaction recovery interpretation. We further confirmed this conclusion by interferometric measurement (193nm PS/PDI) of the OPD in damaged versus undamaged regions in fused silica samples before and after thermal annealing.

In isothermal annealing of UV-induced compaction, saturation of the compaction recovery was observed and this is consistent with the earlier observation of the saturation of the thermal recovery of pressure-compressed fused silica. A strong correlation between the compaction rate and thermal history among our testing fused silica samples was found.

The sub-linear power dependence of the ionization-induced compaction in fused silica has been discussed for many decades. In this work, we propose an analytical compaction model to explain this universally observed sub-linear power dependence. We attribute the origin of the compaction to the Si-O-Si bridging bond angle shrinkage following ionization events. The sub-linear power dependent compaction is a direct consequence. Based on this model, the UV-induced compaction rate in fused silica depends on the effective fictive temperature of the sample; higher fictive temperature corresponds to higher UV compaction rate. We used high-temperature pre-annealing to change the fictive temperature of some samples; these samples later showed the UV-compaction behavior consistent with our fictive temperature model.

The density of fused silica increases linearly with the absorbed dose when exposed to atomic displacement radiation such as neutrons. The diffraction data suggest that the internal structure of fused silica undergo a dramatic change during radiation.

After studying the previous theoretical and experimental results, and examining the physical condition generated by knock-on radiation, we propose a two-phase model of fused silica structure and differentiate the knock-on damage from the ionization damage accordingly. We conclude that the knock-on radiation generally triggers a phase transition in the fused silica network, and the phase transition temperature is well above the glass transition temperature T_g . The new phase *B* structure has smaller Si-O-Si bridging bond angles and higher density than the structure of phase *A*. We use this model to understand the experimental results associated with the volume change induced by hydrostatic pressure, fast neutron, ion, electron and photon etc. Based on our theory, the compaction induced by knock-on radiation and hydrostatic pressure in vitreous silica is different from the compaction induced by ionizing radiation.

Appendix

In this appendix I briefly describe two additional experiments performed in the course of this study. Neither experiment provided significant new information, but they are described for completeness.

A-I. Gamma rays induced compaction in fused silica

Gamma rays cause knock-on and ionization in fused silica at the same time. ^{60}Co gamma rays have about 1.2 MeV energy. Most of the absorbed energy is lost to ionization, and since it takes about 20 eV to produce one electron-hole pair in fused silica [1], 1 Mrad absorbed gamma rays produces approximately 10^{18} ionization events/gram. Some of the gamma rays can cause displacement damage via the "Compton electrons" knock-on mechanism [2]. Because of very poor momentum-matching conditions knock-on events are infrequent, and only about 10^{12} events/gram occur per Mrad with gamma radiation [3-5].

To estimate the relative importance of ionization versus displacement in gamma radiation of fused silica, we can estimate the compaction from either process independently based on compaction rates for UV damage (pure ionization) and neutron radiation (displacement dominant). Because the dependence on dose is different in the two mechanisms, we will do this at two typical dose: 1 and 10 Mrad. We will convert the UV dose to equivalent dose in rads by using the two-photon absorption coefficient at 193nm, and assuming electron-hole pair is produced per two-photon event. We will use a typical compaction rate for sample type F.

TABLE A-I Gamma radiation-induced compaction in fused silica (Type F)

Equivalent UV (193nm) Dose	1 Mrad	10 Mrad
Estimated Gamma-Induced Compaction (Ionization)*	1.72ppm	7.8ppm
Estimated Gamma-Induced Compaction (Displacement)**	<0.01ppm	<0.1ppm

*Assuming most of absorbed energy goes into ionization.

**Knowing that about every 100 gamma ray photons cause 1 displacement event [3]. 10^{10} rad knock-on radiation causes 3% densification in fused silica [6].

From the above comparison we concluded the ionization process is dominant in gamma radiation-induced compaction in fused silica. In Chapter 4, we reported that the UV pre-compacted fused silica samples show lower compaction rates compared to the virgin samples as predicted by the sub-linear power law. Since ionization is the dominant process in gamma rays induced compaction in fused silica, we expect to see the same effect in the pre-gamma-irradiated fused silica. This implies that the UV compaction rate of the pre-gamma-irradiated sample should be lower compared to that of the virgin sample if we suppose the gamma radiation has the same effects as UV radiation. Fig. A-1(a), A-1(b) and A-1(c) show the experimental results for sample D, E and F. The fused silica samples were first irradiated in gamma ray source at Lawrence Livermore National Laboratory, the source has dose rate at 10krad/min. After the gamma-ray exposures, we used birefringence scans to check the uniformity of compaction, and found the gamma-irradiated samples have the similar uniformity as the virgin samples. In the three type of samples we tested, after low dose gamma irradiation (3.6 Mrad), all of D, E and F samples show lower UV compaction rates compared with their virgin sample values (Fig. A-1(a), A-1(b), A-1(c)). However, in sample E the UV compaction rate increases from

the virgin sample values after high dose gamma exposure (Fig. A-1(b)). From these experiments, we see that even the gamma rays interact with fused silica through ionization primarily, the small possibilities of the knock-on process makes the physical picture very complicated. Earlier observations on other fused silica types also showed that gamma rays introduce volume expansion in some samples and contraction in others [7].

In the gamma-irradiated samples, a significant complication came from color center formation. The transmission at 193nm wavelength was reduced to a very large extent (Fig. A-2).

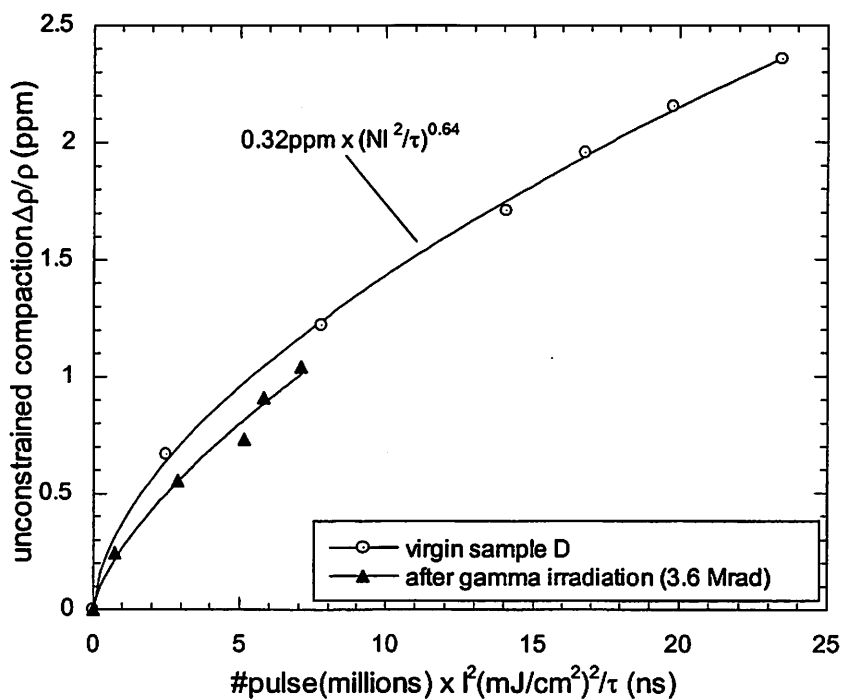


Figure A-1(a). UV-induced compaction curve for sample D before and after gamma irradiation.

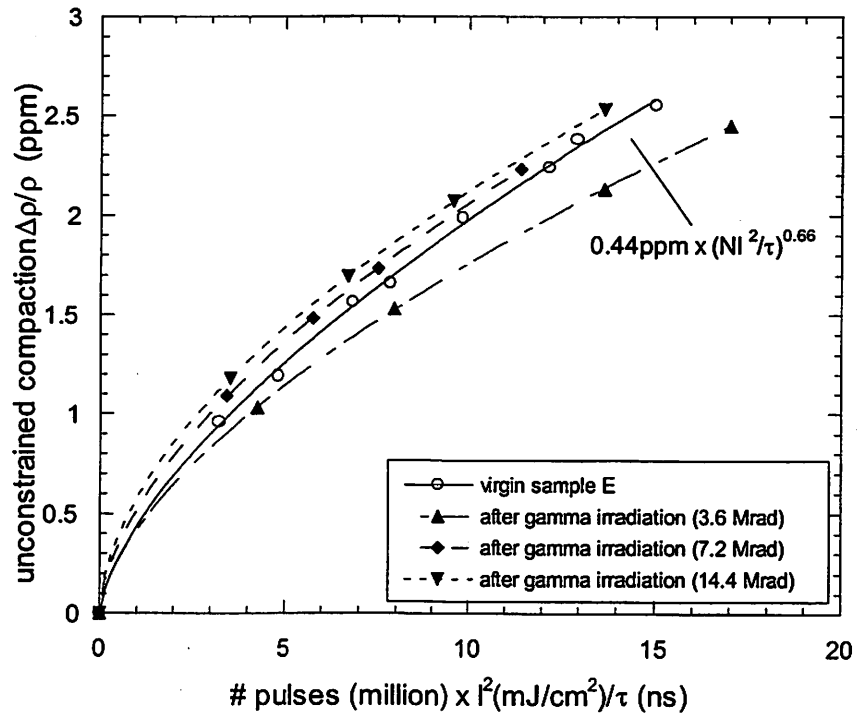


Figure A-1(b). UV-induced compaction curve for sample E before and after gamma irradiation.

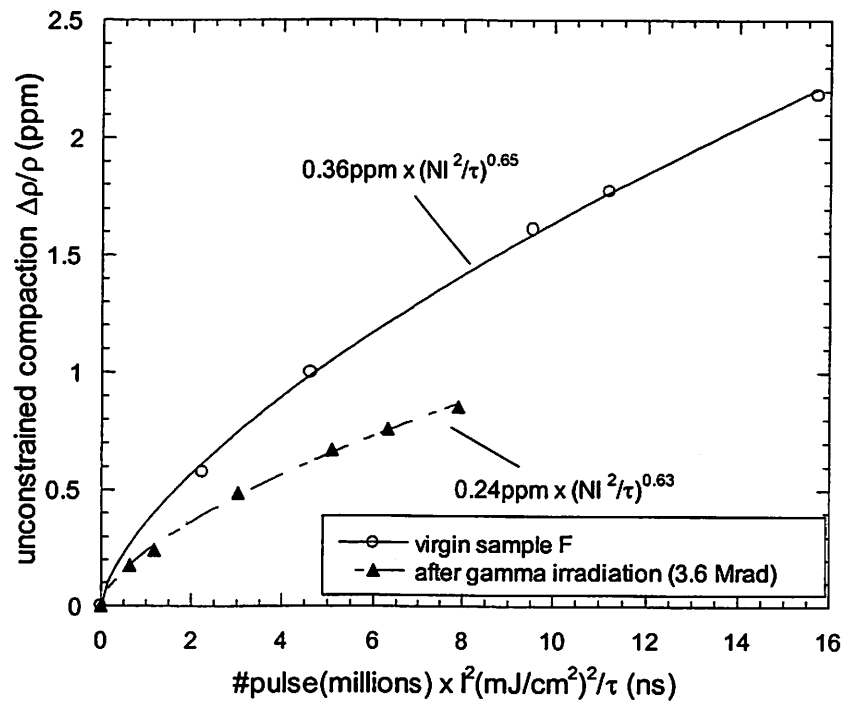


Figure A-1(c). UV-induced compaction curve for sample F before and after gamma irradiation.

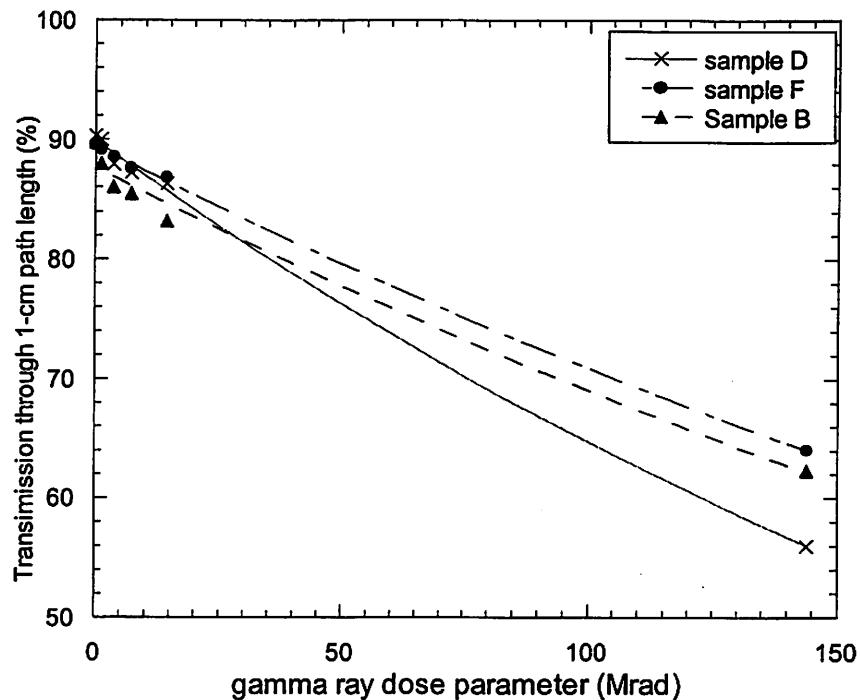


Figure A-2. Transmission decay at 193nm after gamma radiation for 1cm thick Samples.

A-II. X-ray diffraction study of compacted fused silica

The X-ray diffraction spectra of a portion of the sample within and outside the UV-irradiated region (Fig. A-3) were measured using a Copper K_{α} X-ray source (1.5Å wavelength). The X-ray beam diameter is approximately 5mm. Fig. A-4 shows the spectra from the irradiated and unirradiated areas. The signal from intrinsic scattering is not subtracted, but the property that both spectra have equal magnitudes at high diffraction angle indicated that scattering was equal for both measurements.

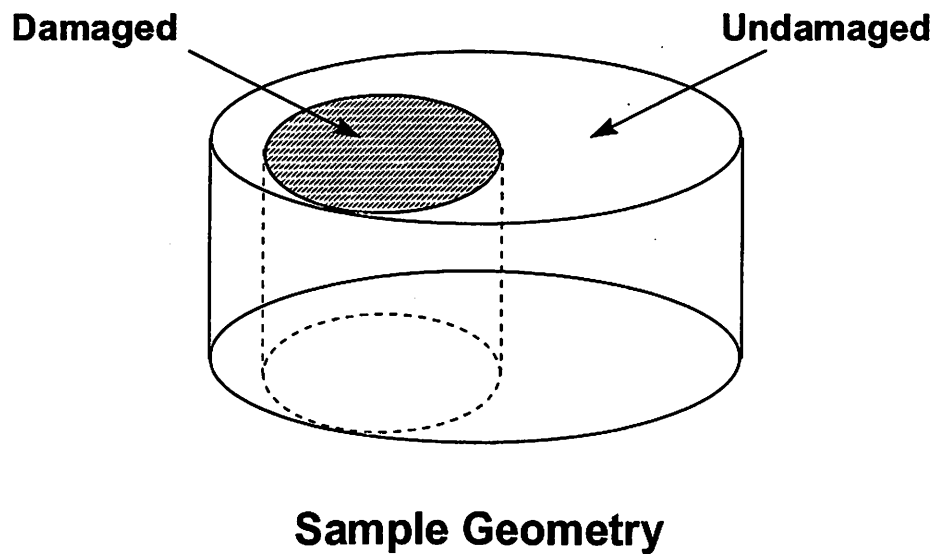


Figure A-3. The geometry of the tested sample---Suprasil 2. The damaged area was irradiated with 70 million $40\text{mJ}/\text{cm}^2$, 193nm pulses.

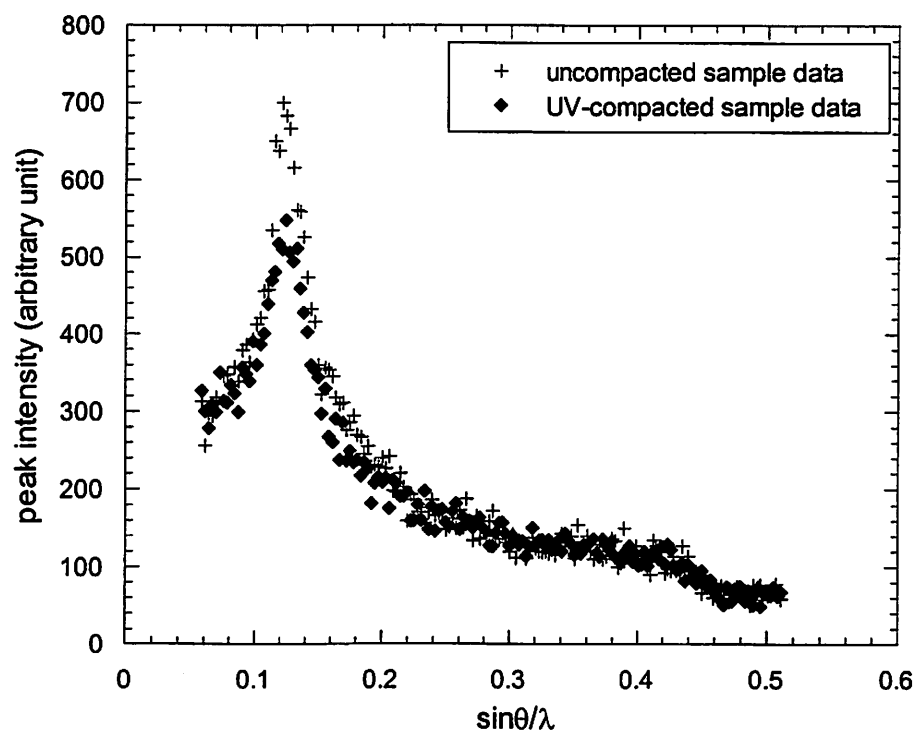


Figure A-4. X-ray diffraction spectra of Suprasil 2. (For both damaged area and undamaged area).

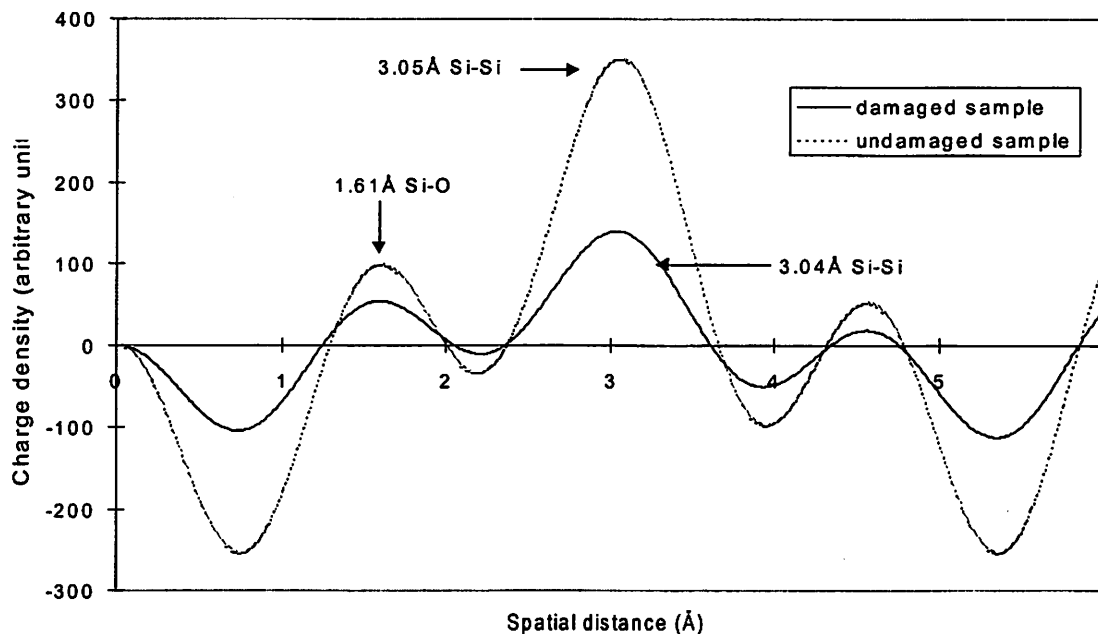


Figure A-5. Spatial atomic distribution in UV damaged and undamaged Suprasil 2.

We can not see obvious differences between the spectra from the undamaged and damage area in the tested fused silica. Based on the Fourier transformation technique developed by B. E. Warren [8], we transferred the measured $\theta-2\theta$ spectrum to the spatial distribution of atoms, from Fig. A-5, and again no differences can be detected. This can be explained by the fact that ionizing radiation is very inefficient in producing densification in fused silica compared with knock-on radiation such as that of neutron irradiation. Lower compaction levels make the direct observation of the atomic structure change in fused silica almost impossible.

A-III. References

- [1] G.J.Dienes, G.H.Vineyard, "Radiation Effects in Solids", Wiley, New York.
- [2] D.L.Griscom, SPIE Vol. 541, 38 (1985)
- [3] O.S.Oen, D.K.Holmes, J. Appl. Phys. 30, 1289 (1959)
- [4] D.L.Griscom, P.C.Taylor, P.J.Bray, J. Chem. Phys. 51, 977 (1969)
- [5] D.L.Griscom, G.H.Sigel, R.J.Ginther, J. Appl. Phys. 47, 960 (1976)
- [6] R.A.B.Devine, Nuclear Instr. and Meth. B91, 378 (1994)
- [7] J.E.Shelby, "Radiation effects in hydrogen-impregnated vitreous silica", J. Appl. Phys. Vol. 50, 3702 (1979)
- [8] B.E.Warren, J. Appl. Phys. Vol. 8, 645 (1937)